McGill

Designs and Characterization of Switchable Microwave Electromagnetic Bandgap and Split-Ring Resonator Structures

By

Jay-Hsing (Jack) Wu

Department of Electrical & Computer Engineering

McGill University, Montreal, Canada

April 2007

A thesis submitted to McGill University in partial fulfillment of the requirements of the degree of Doctor of Philosophy

Your file Votre référence
ISBN: 978-0-494-32335-9
Our file Notre référence
ISBN: 978-0-494-32335-9

ABSTRACT

The design and characterization of both electromagnetic bandgap (EBG) and inter-coupled split-ring resonator (SRR) structures utilized in microwave frequencies were proposed and studied. A new double-stopband EBG structure with a passband region of 14 to 18 *GHz* was initially constructed by determining the critical structural ratios. To reduce the size of EBG structure, a novel tapered array pattern was introduced. The structural period, the number of slot, and the length of slot were examined and a strong correlation was found between the lowpass cutoff frequency and the center slot length. Non-linearly tapered configuration was applied to enhance the filter performance and its size was only 57% of the conventional EBG structure. Inter-coupled SRR was also examined and utilized as a bandpass filter when it is implemented on the microstrip line for the first time. It was found that the proposed structure can provide a fractional bandwidth of over 68% with an insertion loss of 0.81 *dB* in the passband region with a device size of 15.5 *mm*.

Chemical bath deposited Cadmium Sulfide (CdS) thin film was applied to the microwave structures to construct switchable filters. The illumination-sensitive CdS thin film's sheet resistance has been demonstrated to be able to switch from 300 to 10^9 *Ω/square*. With the proposed "conductive-islands" implementation, switching of EBG structure's transmission coefficient (S_{21}) was achieved from 31.3 *dB* to 5.6 *dB* at 13

GHz. The inter-coupled SRR structure also showed a S_{21} switching response from 19 *dB* to 1.5 *dB* at 5 *GHz*. Therefore, optically controlled microwave filters were successfully constructed and realized.

Critical contributions in the field of microwave periodic structures are the characterization and the construction of double-stopband structure, linearly and non-linearly tapered array structures, and inter-coupled SRR structures. Vital characteristics and advantages discovered include wide stopband, reduced size, and large fractional bandwidth. Chemical bath deposited CdS thin films were studied to achieve an ultra low sheet resistance and high photosensitivity. Important applications associated with these structures are microwave lowpass/bandpass filters and optically controlled filters.

RÉSUMÉ

La conception et la caractérisation de l'espace de bande électromagnétique (EBG) et du résonateur de structures inter-couplées *«split-ring»* (SRR), utilisées dans des fréquences micro-ondes, ont été proposées et étudiées. Une nouvelle structure de bande à double-arrêt EBG avec une région de bande de passage de 14 à 18 *Gigahertz* a été construite en déterminant les rapports structuraux critiques. À fin de réduire la taille de la structure d'EBG, un nouveau modèle d'arrangement de fente conique a été introduit. La période de la structure, le numéro de fente, et la longueur de la fente ont été examinés, et une corrélation forte a été trouvée entre la fréquence de coupure *«lowpass»* et la longueur centrale de fente. De la configuration conique non-linéale a été appliquée à fin d'augmenter la performance du filtre et sa taille était seulement 57% de la structure conventionnelle d'EBG. SRR inter-couplé a été également examiné et utilisé comme un filtre de passage de bande, quand il a été mis en application sur la ligne de bande micro pour la première fois. On a constaté que la structure proposée peut fournir une largeur de bande partielle de plus de 68% avec une perte d'insertion de 0.81 *dB* dans la région de bande de passage avec une taille de dispositif de 15.5 *millimètre*.

Une couche mince -- déposée par bain chimique -- de sulfure de cadmium (CdS) a été appliquée aux structures de micro-onde, pour construire les filtres permutables.

La résistance de la feuille à couche mince d'illumination-sensible CdS a été démontrée de pouvoir commuter de 300 à 10^9 *Ω/square*. Avec l'exécution proposée des «îles-conductrices», du changement du coefficient de la transmission de la structure d'EBG (S_{21}) a été obtenu de 31.3 *dB* à 5.6 *dB* à 13 *Gigahertz*. La structure inter-couplée de SRR a également montré une S_{21} réponse de commutation de 19 *dB* à 1.5 *dB* à 5 *Gigahertz*. Par conséquent, des filtres de commande optique à micro-ondes ont été construits et réalisés avec succès.

Des contributions critiques dans le domaine des structures périodiques de micro-onde sont la caractérisation et la construction de structure «*double-stopband*», les structures coniques de rangée linéaires et non-linéaires, et les structures inter-couplées SRR. Des caractéristiques essentielles et des avantages découverts incluent le «*stopband*» large, la taille réduite, et la grande largeur de «*bandwidth*» partielle. Les couches minces déposées par bain chimique de CdS ont été étudiées pour réaliser une résistance de feuille ultra basse. Des applications importantes associées à ces structures son des filtres «*lowpass/bandpass*» à micro-ondes et des filtres à commande optique.

ACKNOWLEDGEMENTS

First and the most important of all, I would like to dedicate my sincere appreciation to Prof. Shih, my supervisor, for his excellent guidance, knowledgeable advices, and thoughtful considerations during this research work. I truly admire and thank him for his exceptional supervision. Also, I would like to thank my colleagues Yi Chen, Yu-Mo Chien, Steve Yang, Hung-Pao Yang, Jeanne Shih, Hadley Myers, Sean Chen, Patrio Chiu, and Sanna Hui for their assistance and spontaneous discussions. Moreover, I would like to take this opportunity to thank Fonds de recherché sur la nature et les technologies (FCAR) from Quebec, Canada for their funding support.

Great appreciation also goes to Steve and Cindy Qiu at CIS Scientific for their helpful discussions, kind patience, support, and all the help they have given me while I was doing my measurements.

Last but not the least; I would like to thank my friends and family for their unconditional support and encouragements. Their care and love mean so much to me and are deeply appreciated. Special thanks to my dear friend, Mario Hepburn, for helping me translate the abstract into French.

CONTENTS

1. INTRODUCTION

The transfer of information has become an integral part of our lives. We rely on communication systems and networks to transmit and receive an enormous amount of information everyday. Just to name a few that are more closely bounded to us such as television/radio networks, telephone networks, and computer inter-networking (internet). The advancement in the telecommunication technology not only allows the ease of conveying information from one place to another, but also encourages people to share inspirational ideas and tackle the major obstacles that this world faces together. It was estimated in 2006 that the telecommunication industry generated revenue of US$1.2 trillion, which is equivalent to around 2 % of the gross world product (~ US$59 trillion) [1-1]. Therefore, it is vastly important to develop the components of the telecommunication equipment so that the ability to control the transmitted and received information can be performed efficiently.

For a large amount of information to travel faster and further, microwave and millimeter-wave components are often applied. Microstrip transmission line is a suitable high frequency structure that can be utilized to carry these signals across a long distance with minimal insertion loss. It is a very suitable transmission structure for microwave signals, which, can propagate through air very efficiently. Moreover, to provide robustness and flexibility in designs and functions, these microstrip

transmission lines are often built with periodic patterns that are located either in the ground plane or on the microstrip line. These patterns not only assist the transmission of the signals, but also they provide useful functionalities such as frequency-selection and filtering. Therefore, the design and characterization of structures that are compatible with microstrip line become a very important part in these high-speed components. In this thesis work, two types of structures were considered and proposed to integrate with the microstrip transmission line: the electromagnetic bandgap (EBG) structure and the split-ring resonator (SRR) structure. Both structures are suitable for planar circuit technology and are relatively simple to fabricate. New characteristics and design methods were explored and studied utilizing the structures with microstrip lines. Mainly, three types of novel periodic structures are proposed to be utilized in the microwave region: double-stopband EBG structure, linearly and non-linearly tapered array EBG structures, and inter-coupled SRR structures. In addition, switchable microwave lowpass and bandpass filters are developed and experimentally verified with the proposed low-resistance CdS thin film.

The term Photonic Band-Gap (PBG) was initially acknowledged in late 1980s where it is used to describe the blockage of traveling electromagnetic (EM) waves in optical regime. Such blockage in the transmission is caused by a periodically changing pattern of the dielectric layers with different index of refractions [1-2, 1-3, 1-4, 1-5].

In the microwave applications, the structures that exhibit this phenomenon are referred to as Electromagnetic Band-Gap (EBG) structures. The most advantageous aspects of the microwave EBG structures are their extremely simple implementation and effective stopband ability. Planar EBG structures can be implemented easily in the ground plane of a microstrip transmission line with periodic perforations. These perforations, with appropriate spacing, provide interference for the traveling EM waves at a certain range of frequency [1-6, 1-7, 1-8]. Fig. 1-1 illustrates a typical EBG structure with four periodic rectangular perforations implemented directly underneath the microstrip line to induce a stopband effect.

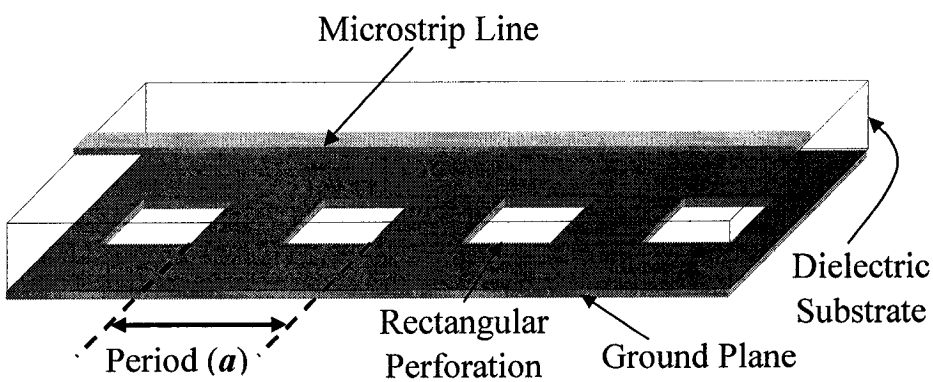

Fig. 1-1: A typical one-dimensional EBG with rectangular perforations implemented in the ground plane of a microstrip transmission line.

It has been reported that that the ratios of perforation dimensions to the period (***a***) are closely linked to the stopband frequency [1-9]. In the beginning of Chapter 3, this relationship is further investigated and subsequently a double-stopband EBG structure with a controllable passband region has been developed simply by adjusting the structural ratios [1-10]. The proposed double-stopband EBG structure provides an

opportunity to have a profound understanding of the relationship between the structural dimension and the passband region, which has not been explored before in the literature.

Ordinary periodic planar EBG structures have S_{11} ripples in the passband region and therefore the transmission quality in this region is degraded [1-11, 1-12]. S_{11} ripples usually occur near the stopband-edge and degrade the passband performance; therefore, insertion loss is increased. However, this drawback of the planar EBG structures can be solved with an innovative Tapered Array (TA) pattern [1-13]. It is noted that the fiber Bragg gratings, which utilize the grating apodization have the similar concept applied in the optical regime [1-14, 1-15]. The TA patterns proposed in this thesis work provide not only defined passband and stopband regions, but also the position of cutoff frequency can be controlled very easily. The physical length of TA patterned EBG structure does not increase with a decrease of cutoff frequency like the typical EBG structures. Furthermore, the stopband region of the TA patterns is much wider than regular periodic patterns. The characterization of linearly and non-linearly TA patterned structures are also presented in Chapter 3.

Split-ring resonator (SRR) structure was first proposed by Pendry *et al.* [1-16] to achieve a large imaginary component in effective permeability due to its unique resonance nature. Smith *et al.* [1-17, 1-18] further investigated the split-ring resonator

structure together with metallic wires placed in proximity. Such combined structure exhibits passband characteristics with backward wave propagation and it is known as the left-handed medium. This realizes the structure proposed by Veselago in 1968 [1-19], which have a negative permeability and a negative permittivity simultaneously. Soon after, split-ring resonator and complementary split-ring resonator structures have been exploited in many different applications including microwave filters [1-20, 1-21, 1-22, 1-23, 1-24, 1-25]. However, most of these structures have the resonators implemented in the ground plane or beside the parallel coupled microstrip lines to enhance the filtering performance. Planar edge-coupled split-ring resonator was proposed as bandpass filter but the fractional bandwidth still remains small [1-26]. In Chapter 4, a newly proposed structure called inter-coupled split-ring resonator structure implemented directly on the microstrip line is characterized and explored for the first time. The structure is found to have an exceptionally large fractional bandwidth when it is utilized as a bandpass filter. Fig. 1-2 shows an inter-coupled split-ring resonator structure.

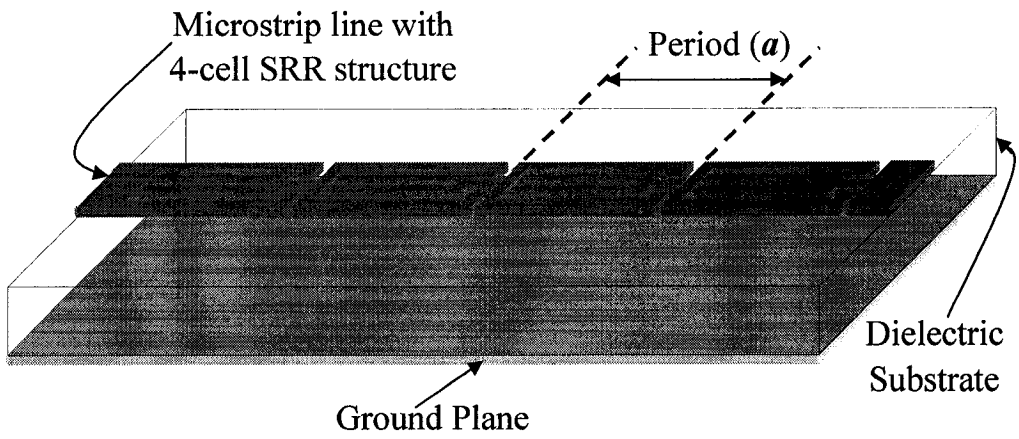

Fig. 1-2: An inter-coupled split-ring resonator (SRR) structure with four unit cells implemented on the microstrip line.

Chapter 5 presents the deposition method of illumination-sensitive Cadmium Sulfide (CdS) thin film by Chemical Bath Deposition (CBD). It has been reported that CdS thin film deposition by the CBD method yields the best results in terms of photoconductivity and photosensitivity [1-27, 1-28]. The CBD method is also a low-cost and a simple way to deposit CdS over a large area. This chapter explores and proposes a set of optimal conditions for depositing CdS thin films with extremely low sheet resistance (~ 300 *Ω/square*) under illumination condition. Thus, it is possible to apply such thin film to microwave structures and achieve optical switching of the transmission signals [1-29, 1-30].

Chapter 6 combines the works on EBG and SRR structures with the low sheet resistance CdS thin film to realize the proposed optically switchable microwave filters. The highly sensitive CdS thin films were deposited on the ground plane of the EBG structures to cover up the perforations. Meanwhile, a novel perforation pattern is

introduced in this thesis to enhance the switching performance of the EBG structures. The additional "conductive islands" in the center of the perforations improved the insertion loss significantly when the structure was under illuminated condition. For inter-coupled SRR structures, the CdS thin film is deposited on top of the microstrip line so that the passband effect can be switched with illumination. Due to the high isolation between the controlling device and the periodic structures, there are many potential applications for the switchable structures such as tunable filters and optoelectronic components. All the simulations were done with Agilent Advanced Design System's Momentum simulator, which has the capability of performing full-wave analysis. The simulation results were verified by experimentally fabricated and measured samples.

Finally, the last chapter gives a summary of the thesis and some possible future improvements that can be carried out to design an EBG/SRR structure and its applications.

2. MICROWAVE EBG AND SRR STRUCTURES

The attractive features of microwave EBG and SRR structures are the abilities to generate passband and stopband regions at specific frequency ranges depending on their structural dimensions. This chapter attempts to summarize the characteristics of different types of EBG and SRR structures that were reported in the literatures. In addition, the possibilities of switching the passband and stopband effects are discussed at the end.

2.1. EBG STRUCTURES

Prior to implementation in the ground plane, the periodic perforations of an EBG structure used to be placed in the dielectric substrate as shown in Fig. 2-1 [2-1].

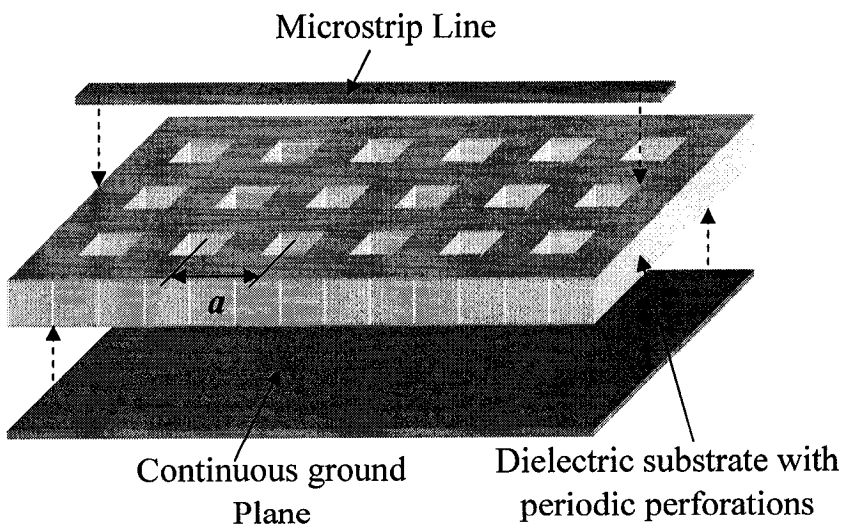

Fig. 2-1: An EBG structure with perforations implemented in the layer of dielectric substrate.

Various shapes of lattices such as triangular, rectangular, and honeycomb were studied for this type of EBG structure and they have been utilized in applications such as

harmonic tuning to increase the power-added efficiency for power amplifiers [2-2, 2-3]. It was also reported that the interference effect due to different periodicities can be cascaded together to produce a wide stopband from 4 *GHz* to 15 *GHz* [2-4]. However, the dielectric-based EBG structures are difficult to fabricate and therefore they were replaced with planar EBG structures, which have the periodic perforations implemented in the ground plane. The fabrication of the planar EBG structures is easier since no drilling process in the substrate is required. In addition, the planar EBG structures possess the same stopband effects as the dielectric-based structures. Generally, the planar EBG structures can be separated into two categories: uniformly and non-uniformly sized perforations.

2.1.1. EBG DESIGNS WITH UNIFORM PERFORATIONS

Fig. 2-2 shows a typical planar EBG structure where uniformly sized perforations are implemented in the ground plane of a microstrip transmission line.

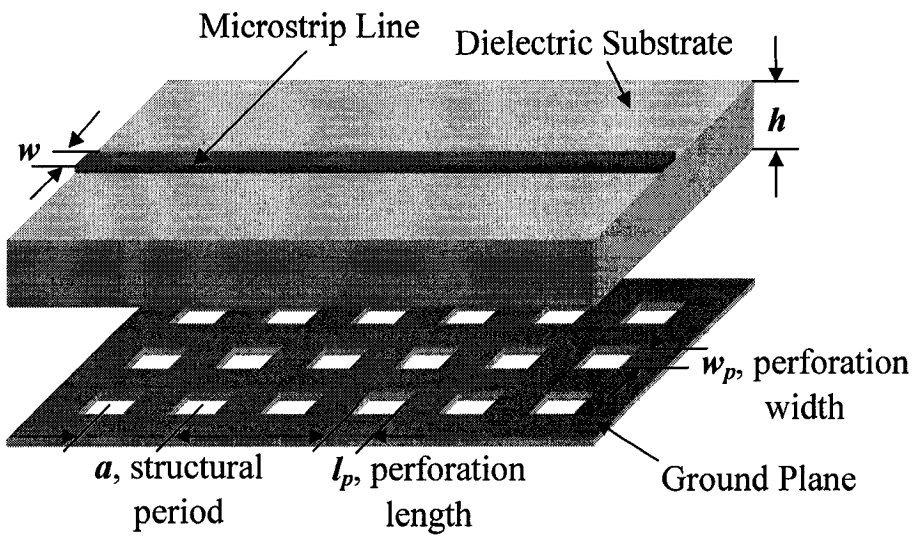

Fig. 2-2: A typical planar EBG structure with 3 by 6 uniformly sized perforations in the ground plane of a microstrip transmission line.

The maximum interference of traveling electromagnetic waves occurs when the Bragg's condition ($\beta a=\pi$, β is the propagation constant) is met and therefore the structural period (a) of the EBG structure can be obtained with a corresponding frequency of interference [1-6, 2-5]. Consequently, the structural period is a critical parameter in determining the stopband frequency of an EBG structure. It has been reported that as the ratios of w_p/a and l_p/a decrease, the stopband width and the stopband attenuation are decreased [1-5]. The stopband attenuation can be improved by increasing the number of perforation period; however, this will also increase the total length of the device.

Furthermore, a wide stopband EBG structure was demonstrated, which was achieved by having a parallel connection of the perforations that were designed to have different stopband frequencies, shown in Fig. 2-3. The perforations located in the

center row have a larger structural period and therefore the corresponding stopband position is at lower frequencies. The top and bottom rows of perforations have a smaller structural period; thus, they are responsible for the stopband located at higher frequencies. When appropriate calculations are applied, the two stopbands can merge together and create a wider overall stopband.

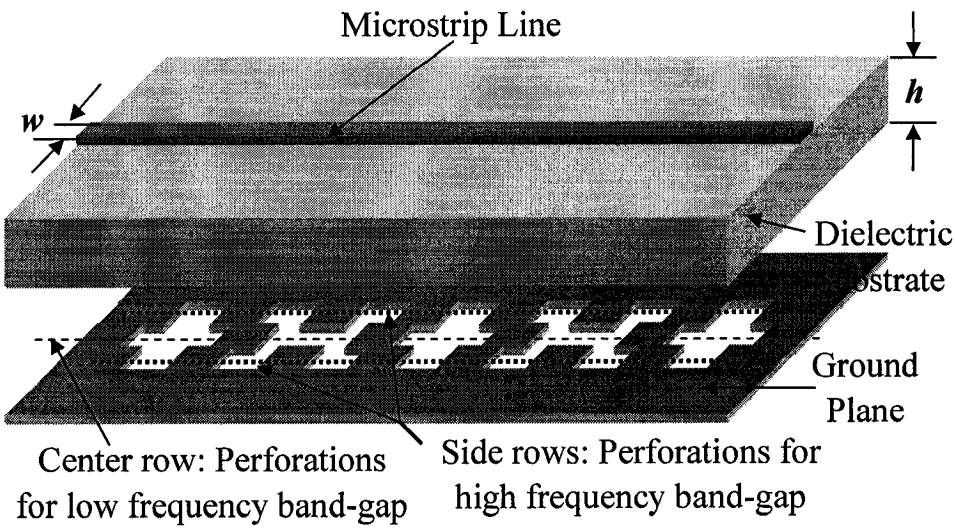

Fig. 2-3: An EBG structure with perforations connected in a parallel configuration.

Such configuration has the advantage of creating a wide stopband width without increasing the physical size of the whole structure like the serially cascaded case. The reported EBG structure that utilizes this configuration has a stopband region that extends from 3 *GHz* to 12 *GHz* [2-6]. The applications of this structure for suppressing harmonics in microstrip patch antenna and feed-forward amplifier have been demonstrated [2-7].

The last EBG design that is introduced in this section is called Uniplanar-Compact EBG (UC-EBG) structure. UC-EBG structures are able to

generate the stopband effects with smaller lattice patterns that are also implemented in the ground plane of a microstrip transmission line. Fig. 2-4 shows an UC-EBG structure where the lattice pattern is consisted of a metal pad and four connecting branches.

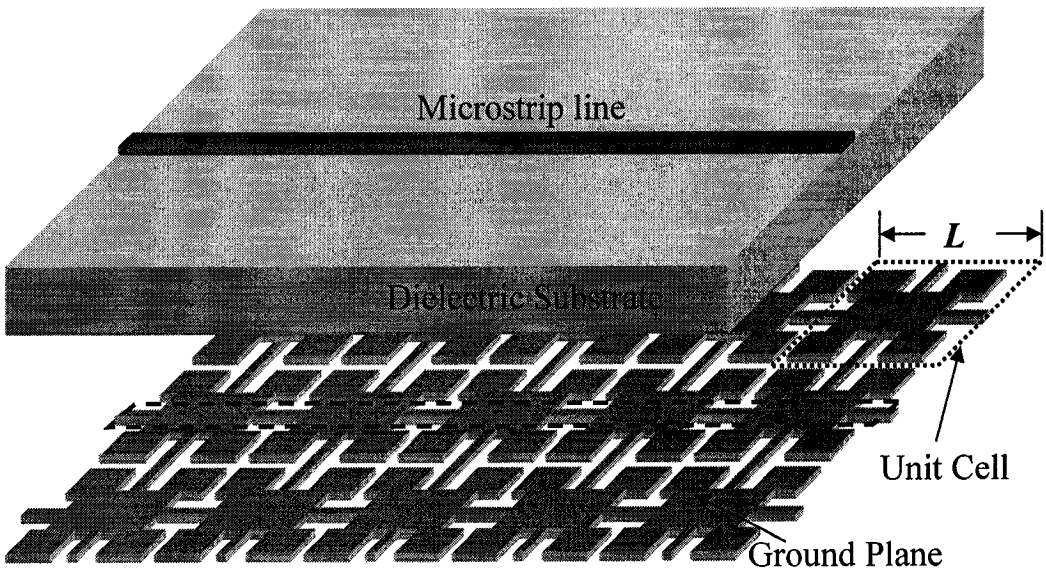

Fig. 2-4: A microstrip transmission line with UC-EBG lattice pattern implemented in the ground plane.

The narrow branches and gaps between metal pads introduce series inductances and shunt capacitances respectively. Thus, the propagation constant (β) is much larger than the conventional microstrip line structure due to these two additional components. According to Bragg's condition, the propagation of quasi-TEM mode along the microstrip line is prohibited when the following expression is satisfied:

$$\beta L = \pi \tag{2-1}$$

Therefore, if β is larger, then the period distance of a unit cell, L, can be reduced [2-8, 2-9]. Many applications of the UC-EBG have been explored. One of the most popular

applications is the harmonic tuning for power amplifiers. It has been shown that the second and third harmonics of a power amplifier can be suppressed by UC-EBG structure so that the power-added efficiency is increased by 10% and the output power is increased by 1.3 *dB* [2-10]. Also, UC-EBG can be used to enhance the performance of lowpass filters (LPF) and bandpass filters (BPF) [2-9, 2-11]. Conventional parallel-coupled BPF used in microwave integrated circuits usually have spurious passbands at high frequencies. Therefore, extra filters are required to eliminate these unwanted harmonics to increase the performance of the overall circuits. However, the insertion loss will increase in this case. This problem can be solve by utilizing UC-EBG structures since they provide intrinsic harmonic tuning at high frequencies; thus, the spurious passbands can be filtered without adding any loss to the transmission line. It has been reported that the UC-EBG structure with a dimension of 18.3 *mm* by 9.1 *mm* (number of period is 3 by 6) can create a stopband above 10 *GHz* with an attenuation better than 20 *dB* [2-9].

2.1.2. EBG DESIGNS WITH NON-UNIFORM PERFORATIONS

Non-uniform perforation patterns or tapered perforation patterns can be utilized to enhance the performance of the EBG structures. It has been reported that an EBG structure can be constructed to have multiple stopbands simultaneously [2-12]. Instead of having a uniform and periodic perforation pattern, the multiple-frequency-tuned

EBG has a non-uniform perforation pattern that is consisted of a multiple of Hamming-windowed raised sinusoidal functions added together. Each function has a different period length and therefore it is optimized to generate a stopband region at a specific frequency range. Thus, the EBG structure possesses an irregular pattern that is very different from the ordinary ones. It has been demonstrated that a triple-frequency tuned EBG structure with periods of 24 *mm*, 19 *mm* and 15 *mm* can create stopband regions located at 3 *GHz*, 4 *GHz*, and 5 *GHz* respectively. The total length of the EBG structure is 215 *mm* long. Even though this device has multiple stopband regions, but the insertion losses in the passband regions remain high and the fabrication of such irregular pattern is complicated.

Another type of non-uniform EBG structure is focused on improving the passband quality near the band edge. Conventional EBG structures with uniform perforations have the problem of S_{11} ripples occur near the stopband edge. Therefore, the passband insertion loss increases significantly. It has been reported that this problem can be solved by implementing non-uniform perforations. Fig. 2-5 illustrates EBG structures with non-uniform circular perforations.

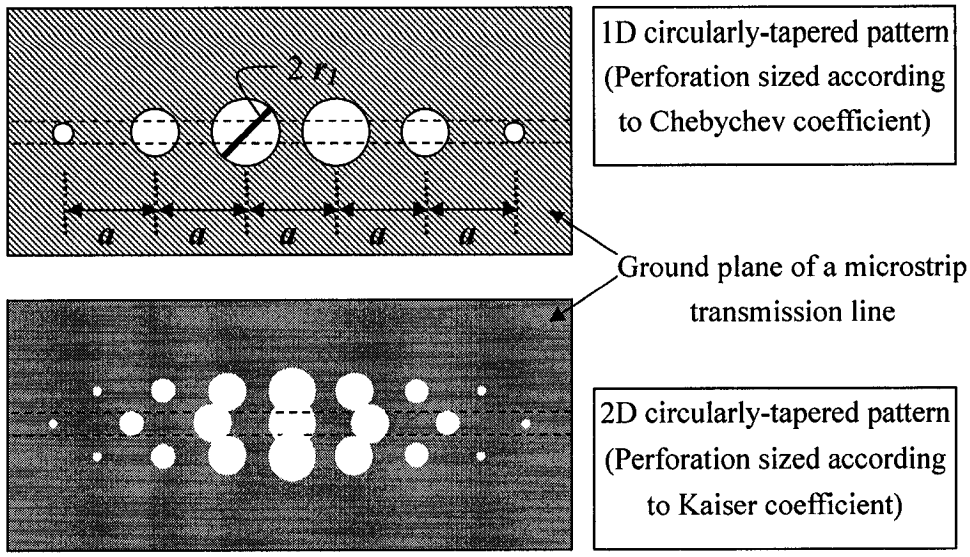

Fig. 2-5: EBG structures with non-uniform circular perforations in the ground plane of a microstrip transmission line [1-10, 2-13].

By proportionally sizing the dimension of each circular pattern according to coefficient of the Chebychev polynomials, an enhanced passband performance can be achieved [2-13]. It has been demonstrated that the S_{11} ripples were significantly reduced with a non-uniform EBG structure (10 periods, a = 5.7 *mm*, r_1 = 2.1 *mm*, ε_r = 10.2) having a stopband region from 9 *GHz* to 13 *GHz*. Similar two-dimensional tapered EBG structure has been constructed with three rows of circular perforations that are proportional to Kaiser's window function [1-10]. Such EBG structures can be utilized as lowpass filters but the overall size is still quite large. Therefore, the tapered structure's size needs to be reduced while maintaining the equivalent performance in order for the EBG effect to be practical in real applications.

2.2. SRR STRUCTURES

The split-ring resonator (SRR) structure is originated to realize the negative permeability of the proposed left-hand material (LHM), which possesses a negative index of refraction. The concept of LHM was first proposed by Veselago in 1968 [1-16]. He carried out the first theoretical investigation on LHM by simultaneously assuming both dielectric permittivity and magnetic permeability to be negative. Thus, the propagating waves inside of the LHM would have unique properties such as reversal of Snell's law, Cerenkov radiation, and Doppler's effect. However, this concept was not experimentally demonstrated until recently in mid-90s. Pendry and Smith have successfully verified the properties of LHM experimentally with thin-wire structures and split-ring resonators [1-13, 1-14, 1-15, 2-14]. These artificial structures, indeed, have negative properties and they stimulate researchers from worldwide to utilize LHM on practical applications. However, the three-dimensional LHM have bulky structures and high insertion loss so they cannot be applied to microwave applications effectively. This does not discourage researchers who are interested in microwave structures because SRR structure, alone, is perfectly suitable to be implemented with planar technology.

Since then, split-ring resonator and complementary split-ring resonator (CSRR) structures (Fig. 2-6) are explored and implemented in planar microwave components

widely [2-15].

(a) (b)

Fig. 2-6: (a) a split-ring resonator and (b) a complementary split-ring resonator structures (Black region represents the conductive metallization region).

Due to its unique magnetic resonance property, SRR and CSRR can be employed beside the microstrip transmission line [1-18, 2-16] or in the ground plane [2-17, 2-18] to generate or enhance the filter responses. Fig. 2-7 shows a construction of lowpass filter utilizing CSRR patterns in the ground plane of a microstrip transmission line.

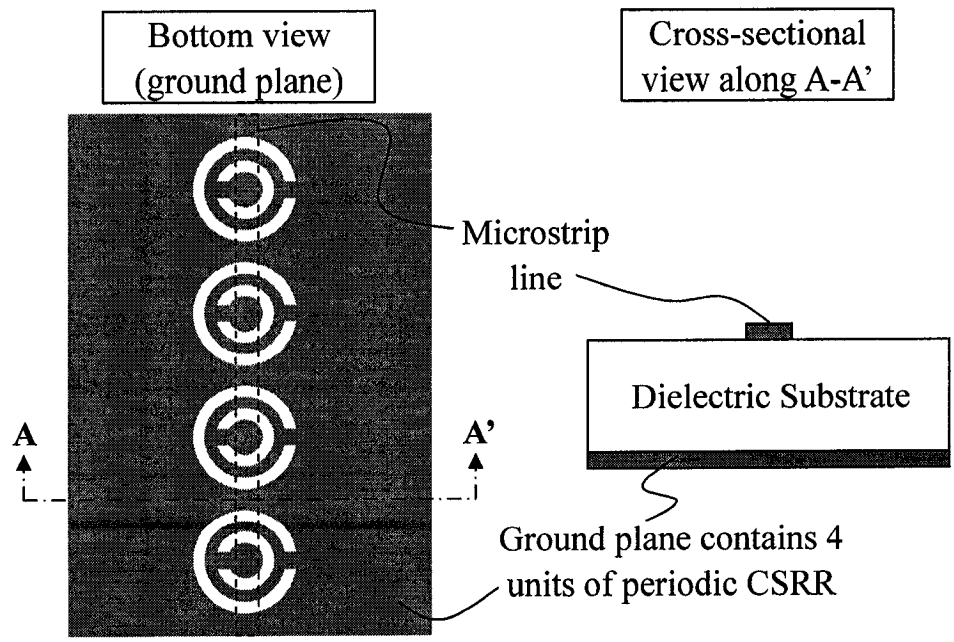

Fig. 2-7: Periodic CSRR structures implemented in the ground plane of a microstrip transmission line to construct a lowpass filter.

Microwave bandpass filters with high-frequency selectivity can also be achieved by

utilizing CSRR structures [1-22]. It has been reported that a passband region centered at 1 *GHz* was achieved with a total device length of 45.6 *mm*, which is significantly shorter than the conventional parallel-coupled line filter. However, this proposed structure needs a more complicated fabrication process.

2.3. SWITCHABLE STRUCTURES

Switching of EBG structure's stopband effect has been reported with the utilization of a piezoelectric actuator [2-19]. The actuator controls a piece of conductor's movement so the EBG structure's perforations can be covered up to eliminate the stopband effect. Fig. 2-8 illustrates how the switching is performed with the actuator.

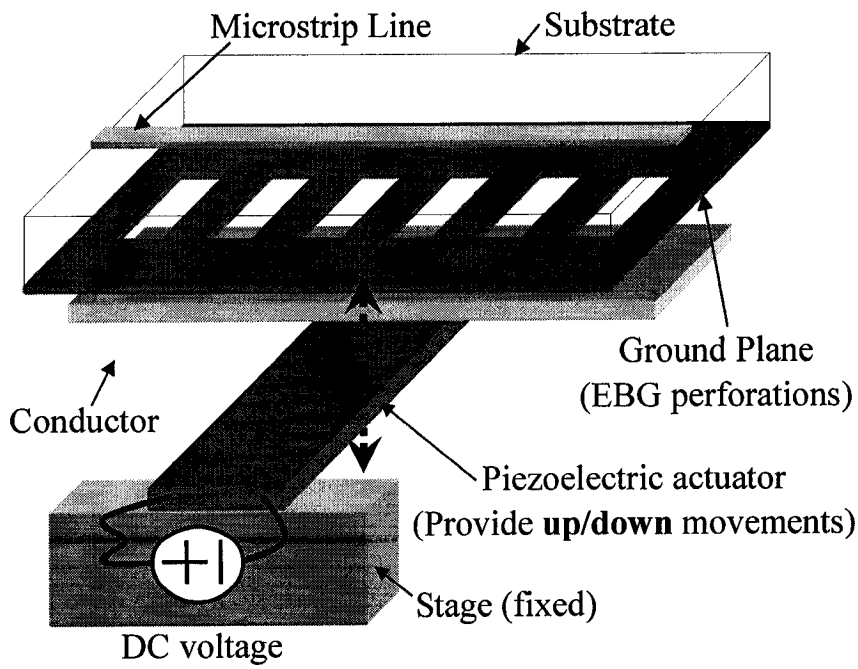

Fig. 2-8: The setup of an EBG structure with a piezoelectric actuator to facilitate switching [2-19].

When a voltage that ranges from 0 to 40 *V* is applied to the actuator, it induced an

up/down movement that ranges from 0 to 400 μm. Thus, the gap between the EBG perforations and the conductor is effectively controlled by the applying voltage. When the conductor piece touches the EBG structure, the ground plane becomes continuous and the stopband is eliminated. Therefore, the stopband phenomenon delivered by the EBG perforations can be switched on and off by the voltage. Such method achieved a switching of the transmission coefficient (S_{21}) from -35 dB to -1 dB at 16 GHz.

Furthermore, optically controlled EBG structures have been demonstrated by simulation [2-20]. This concept utilizes the photoconductive material as the substrate of the EBG structure. As the illumination incidents on the ground plane of the EBG structure where the perforations are located, electron-hole pairs are generated and the conductivity of the photoconductive substrate that is exposed to the illumination is increased. Thus, a continuous ground plane without the perforations is formed and the structure behaves like an ordinary microstrip transmission line. Without the illumination, the conductivity of the photoconductive substrate is low and the EBG structure produces a stopband effect. Fig. 2-9 shows the proposed EBG structure, which the stopband effect can be switched on and off by illumination. However, this proposed structure has only been simulated and therefore the actual characteristics of the photoconductive substrate are yet to be explored experimentally.

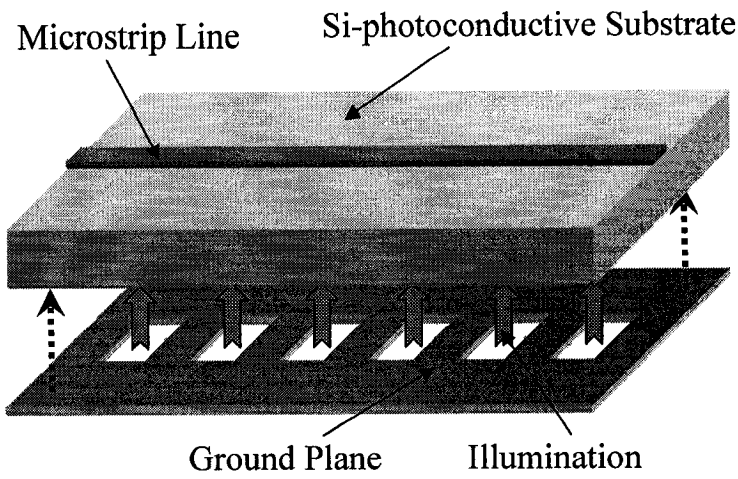

Fig. 2-9: An optically-controlled EBG structure with a photoconductive substrate [2-20].

3. DESIGN OF ELECTROMAGNETIC BANDGAP STRUCTURES

Since the electromagnetic bandgap (EBG) structures possess unique properties of stopband effects, they can be utilized as bandpass and lowpass microwave filters. Two types of EBG structures are studied and explored in this chapter: double-stopband EBG structure and tapered slot-array EBG structures. The main advantages of the proposed double-stopband EBG structure are its simple implementation and flexible control of passband frequency. The critical characteristics of the proposed tapered array EBG structures are their remarkably wide stopband region and reduced device size.

3.1. DOUBLE-STOPBAND EBG STRUCTURES

The vital characteristics of the EBG structure are the perforation dimension to the period ratios. When the appropriate ratios are implemented as the ground perforations in a microstrip line, a double-stopband effect can be achieved. Therefore, the size of the overall structure does not increase while the stopband effects can be controlled to give the desired performance. Effectively, the double-stopband phenomenon creates a passband region that can be utilized as a microwave bandpass filter. First, the preliminary design and the calculation method used to obtain the passband frequency are shown. Then, the EBG structures were simulated with Agilent Advanced Design

System, which provides a full-wave analysis on the structural layout designs. The simulated S-parameters were compared to the measured results from an actual sample to validate the initial design.

3.1.1. DESIGN TECHNIQUE

The stopband effect of the EBG structures is created by the interferences of the traveling electromagnetic waves. In order to achieve this effect, some form of periodic perturbation has to be presented. Therefore, a simple way to accomplish the interference effect is to introduce periodic perforations in the ground plane of a microstrip transmission line structure. Fig. 3-1 shows a typical EBG structure with rectangular perforations periodically placed in the ground plane of a microstrip transmission line. It is noted that the microstrip transmission line structure is on a substrate with a thickness h, and a microstrip line width, w. Together with the dielectric permittivity (ε_r) of the substrate, these three parameters are critical in determining the characteristic impedance (Z_0) of the overall structure. To maintain a low insertion loss and to ensure a good transmission, it is desirable to have Z_0 to be 50 Ω at the operating frequency.

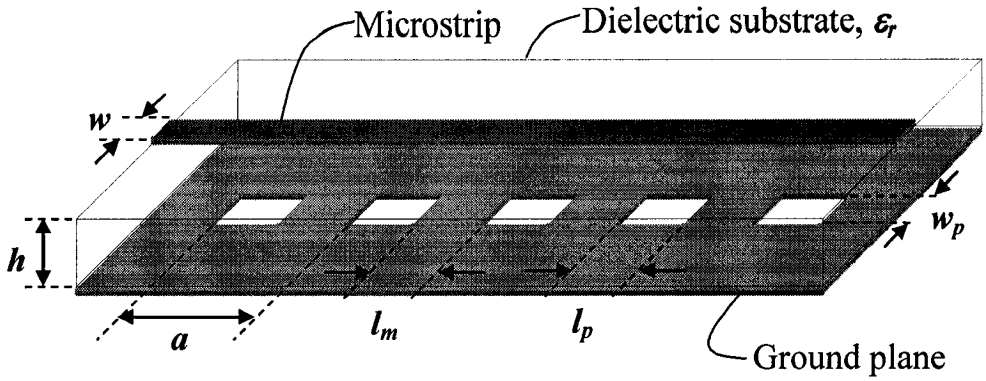

Fig. 3-1: A typical EBG structure with periodically spaced rectangular perforations.

Moreover, each perforation in the ground plane is separated by a period, ***a***. In order to achieve maximum interference for the traveling electromagnetic waves, Bragg's condition must be satisfied and therefore ***a*** is chosen to be half of the guided wavelength (λ_g).

$$n\lambda = 2a\sin\theta; \quad a = n\lambda_g/2 \quad (\boldsymbol{n} \text{ is an integer}) \tag{3-1}$$

Since in the case of microstrip transmission line, the incident angle of the traveling waves (θ) is 90 degrees, interference condition is fulfilled when the period (a) is equal to any multiple of the half guided-wavelength (λ_g). Therefore, it is possible to obtain the stopband frequency from the above relationships.

$$a = \frac{\lambda_g}{2} = \frac{c}{2f_0\sqrt{\varepsilon_{eff}(f_0)}} \quad (\text{Let } \boldsymbol{n} = 1) \tag{3-2}$$

a = Period of the perforations

λ_g = Guided wavelength

c = Velocity of propagating wave in free-space

f_0 = Principle interference frequency

$\varepsilon_{eff}(f)$ = Frequency-dependent effective permittivity*

From this relationship, it is also noted that for every chosen a, interferences will occur at any multiple of the principle frequency, f_0. Meanwhile, each rectangle has a perforation width (w_p) and a perforation length (l_p). The ratios of these dimensions to the period (w_p/a and l_p/a) are the critical factors in determining the stopband characteristics such as the stopband width, stopband frequency, and maximum attenuation of the planar EBG structures. However, to construct an EBG structure with a decent passband region (insertion loss less than 1 *dB*), a more comprehensive investigation on the w_p/a and l_p/a ratios is required.

Since the target is to create a passband region above 10 *GHz*, the preliminary design of the period (a) was chosen to be 6.5 *mm*, which corresponds to stopband regions centered roughly at 9 *GHz* and 18 *GHz* according to the equation shown above. Thus, it is possible to obtain a passband in between the two stopband regions. In the next section, detailed simulation results are presented.

3.1.2. SIMULATION RESULTS

TABLE 3-I shows the global and trial simulation conditions used for all of the EBG structures in this section. The global conditions are to ensure the microstrip line has a characteristic impedance of 50 Ω. A standard bandpass EBG model (a = 6.5 *mm*)

* Please refer to Appendix A for detailed calculations on frequency-dependent effective permittivity.

was first constructed and simulated. Then, the dimension of the EBG structure was reduced to characterize the effects of having a passband behavior at higher frequencies. The performance of each case was evaluated in terms of S-parameters, mainly the reflection coefficient (S_{11}) and the transmission coefficient (S_{21})[†]. Consequently, the S-parameters indicate the vital characteristics of an EBG structure such as the positions of passband width, cutoff frequency, passband insertion loss and stopband attenuation.

TABLE 3-I: GLOBAL AND TRIAL SIMULATIONS CONDITIONS

Global Simulation Conditions:		
Thickness of the substrate (h)	250 μm	
Width of the microstrip line (w)	250 μm	
Characteristic impedance (Z_o)	50 Ω	
Dielectric constant of the substrate (ε_r)	9.8	
Trial Simulation Conditions:		
Parameters	Standard EBG Model	With 50% Reduction
Period (a)	6.50 mm	3.25 mm
Perforation width (w_p)	1.63 mm	0.81 mm
Perforation length (l_p)	4.88 mm	2.44 mm
w_p/a Ratio	0.25	0.25
l_p/a Ratio	0.75	0.75
Number of Period (n)	5	5

In TABLE 3-I, the dimensions and parameters for the standard bandpass EBG model are provided. The w_p/a and l_p/a ratios are not 0.5 as seen in most of the EBG structures. The distinctive feature of the double-stopband EBG structure is that the w_p/a ratio and l_m (distance between two rectangular perforations) are equal to

[†] Please refer to Appendix B for detailed equations of S-parameters.

one-eighth of the guided wavelength ($\lambda_g/8$). Thus, the region in between the two stopbands is suitable for transmission because of the low insertion loss. With these dimensions, the resulting S-parameters of the standard model are shown in Fig. 3-2. A passband region is observed from 13.5 *GHz* to 18.3 *GHz* at the 3 *dB* cutoff frequencies. Therefore, the bandwidth is 4.8 *GHz* with an average insertion loss (S_{21}) of 1.4 *dB*. Also, the return loss (S_{11}) in the passband regions is 28.6 *dB*. Moreover, two distinctive stopband regions located at 10 *GHz* and 22 *GHz* with attenuations of around 30 *dB* result from this construction. Thus, a bandpass filter is effectively created with a very simple planar EBG structure by alternating its perforation dimensions.

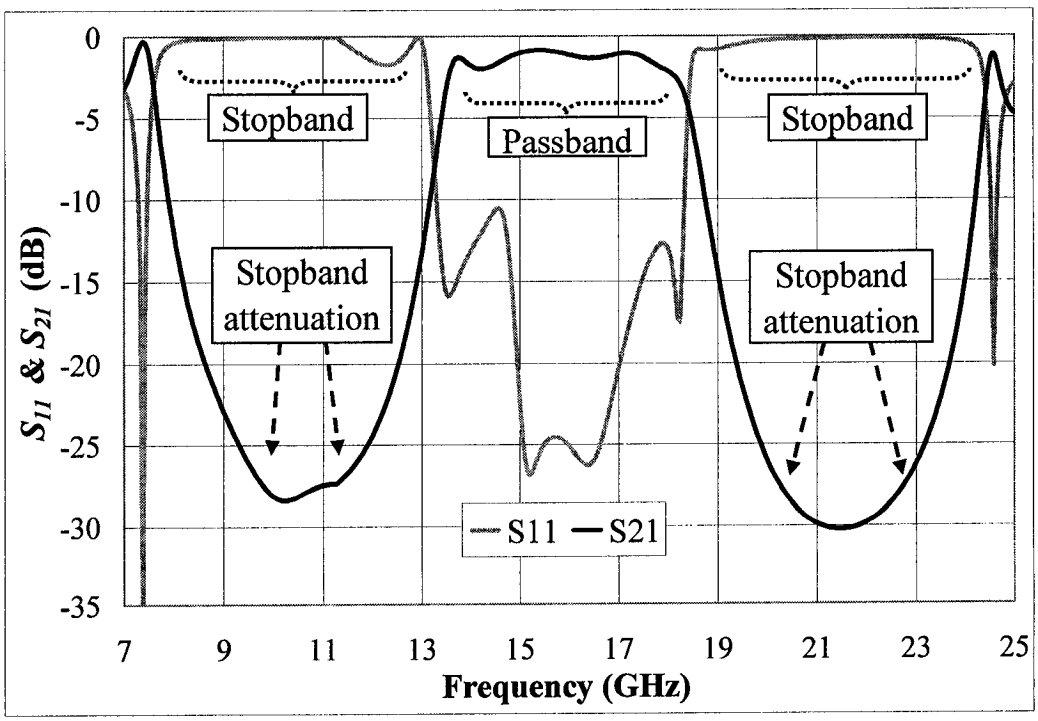

Fig. 3-2: S-parameters showing the passband characteristics of the standard EBG model.

For comparison, Fig. 3-3 illustrates the S-parameters of an ordinary EBG

structure with the w_p/a and l_p/a ratios of 0.5. Even though it has a larger stopband region at low frequencies, the passband region is very poor with high insertion and return losses. Therefore, the ratios of the perforation dimension to the period play a vital role in the transmission and reflection responses.

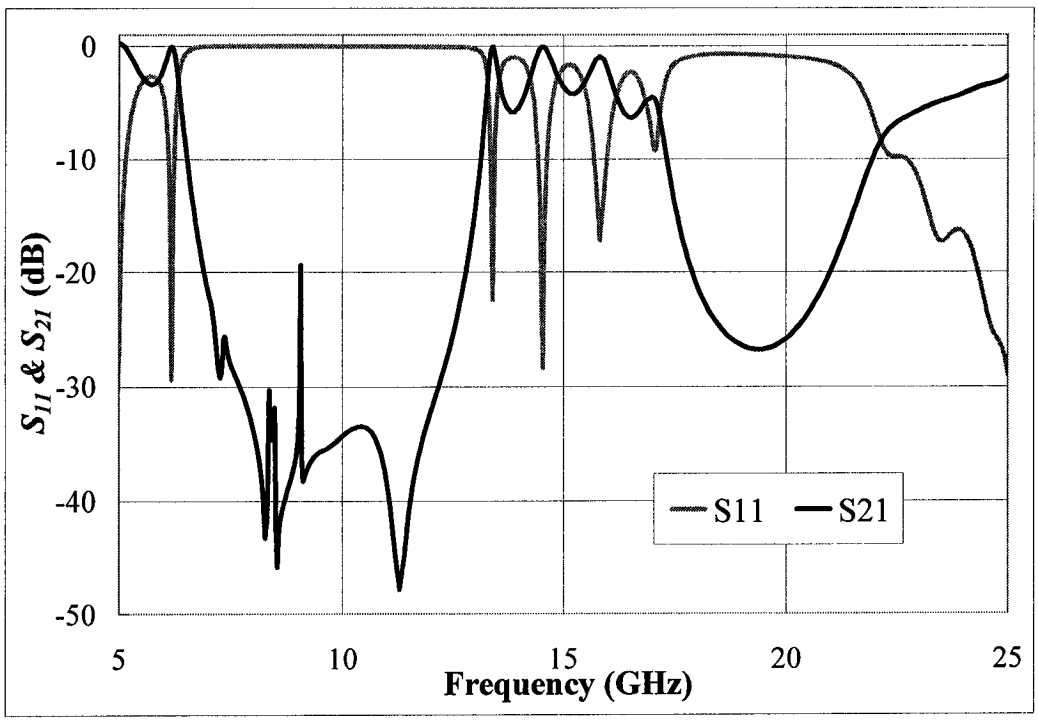

Fig. 3-3: S-parameters of an ordinary EBG structure with w_p/a and l_p/a ratios of 0.5 (a = 6.5 *mm*)

In order to explore the passband characteristics at higher frequencies, the dimensions of the standard EBG model was reduced by 50% while the w_p/a and l_p/a ratios were unchanged. The dimensions used to simulate the EBG structure with 50% reduction are also shown in TABLE 3-I. The resulting S-parameters of the smaller structure are shown in Fig. 3-4. Two structures having different number of periods (n = 5 and n = 7) were simulated. It is observed that the passband region is now shifted to above 20 *GHz*, which is located from 22.4 *GHz* to 34.3 *GHz* at the 3 *dB* cutoff

frequencies. Therefore, the bandwidth is 11.9 *GHz* with an average S_{21} of 1.2 *dB*. In addition, S_{11} in the passband region is beyond 30 *dB*. As the number of the period (***n***) increases, the upper and lower stopband attenuations are increased. Hence, the double-stopband EBG structure can be constructed and utilized at higher frequencies efficiently by just changing the overall dimensions. The simulation results are summarized in TABLE 3-II.

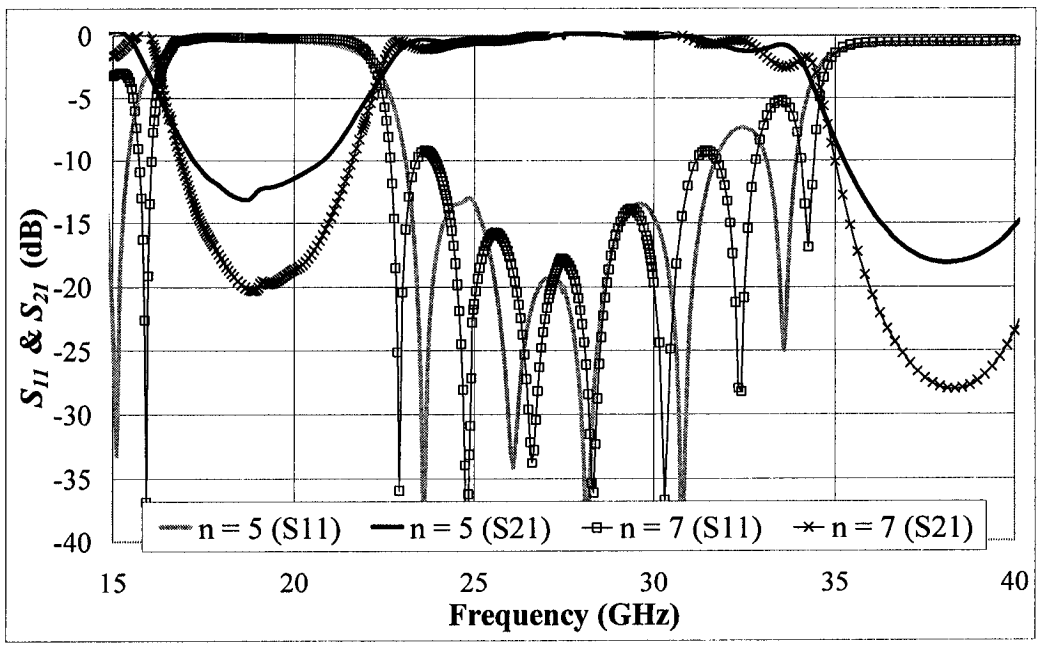

Fig. 3-4: S-parameters for the EBG model with 50% reduction in size.

TABLE 3-II: SUMMARY OF THE SIMULATION RESULTS

	Standard Model	50% Reduction Model
Lower 3 dB passband edge	13.5 *GHz*	22.4 *GHz*
Higher 3 dB passband edge	18.3 *GHz*	34.3 *GHz*
Bandwidth	4.8 *GHz*	11.9 *GHz*
Fractional Bandwidth	30.5%	42.9%
Average insertion loss	1.4 *dB*	1.2 *dB*
Maximum return loss	26.8 *dB*	35.0 *dB*

3.1.3. EXPERIMENTAL MEASUREMENTS AND COMPARISONS

The standard EBG structure with the dimensions shown in TABLE 3-I was fabricated on Alumina substrate (ε_r = 9.8) and the S-parameters were measured with the Anritsu 37347A vector network analyzer, which has the capability of measuring S-parameters up to 20 *GHz*. Please refer to Appendix C for detailed fabrication and measurement procedures. Fig. 3-5 illustrates the front (microstrip line) and the back (EBG perforations) sides of the standard EBG model fabricated for measurements.

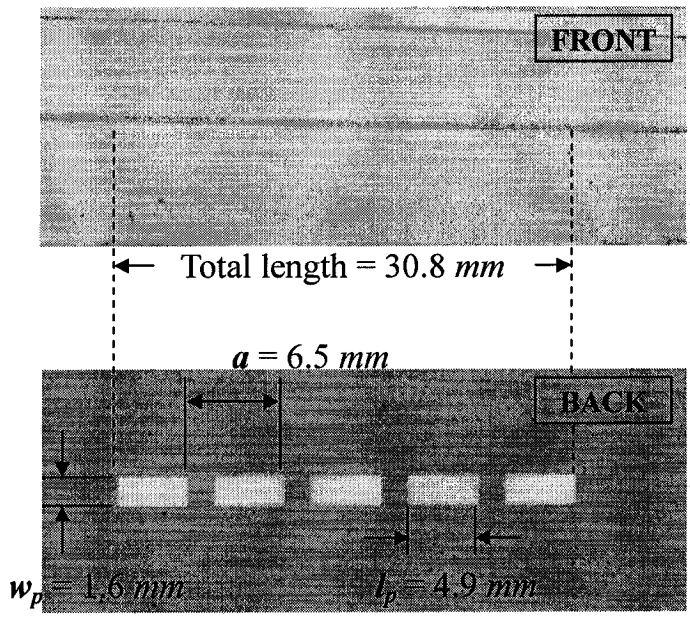

Fig. 3-5: A photo of the actual fabricated sample showing the front and the back side (standard model).

The experimental measured results are compared with the simulated ones, which are shown in Fig. 3-6. It is seen that the general shape of both passband and stopband regions are very similar. However, the measurement results of S_{21} showed a higher insertion loss in the passband region. This is due to the imperfection on the microstrip

transmission line during the fabrication processes. The insertion loss can be improved with a better microstrip transmission line mask. Other aspects of the bandpass EBG structure such as the attenuation of the upper and lower stopbands showed good behaviors in the measurement results. Therefore, the measurement results verified and confirmed the performance of the proposed double-stopband EBG structure. Also, the passband region that exists in this type of EBG structure can be constructed easily with appropriate w_p/a and l_p/a ratios.

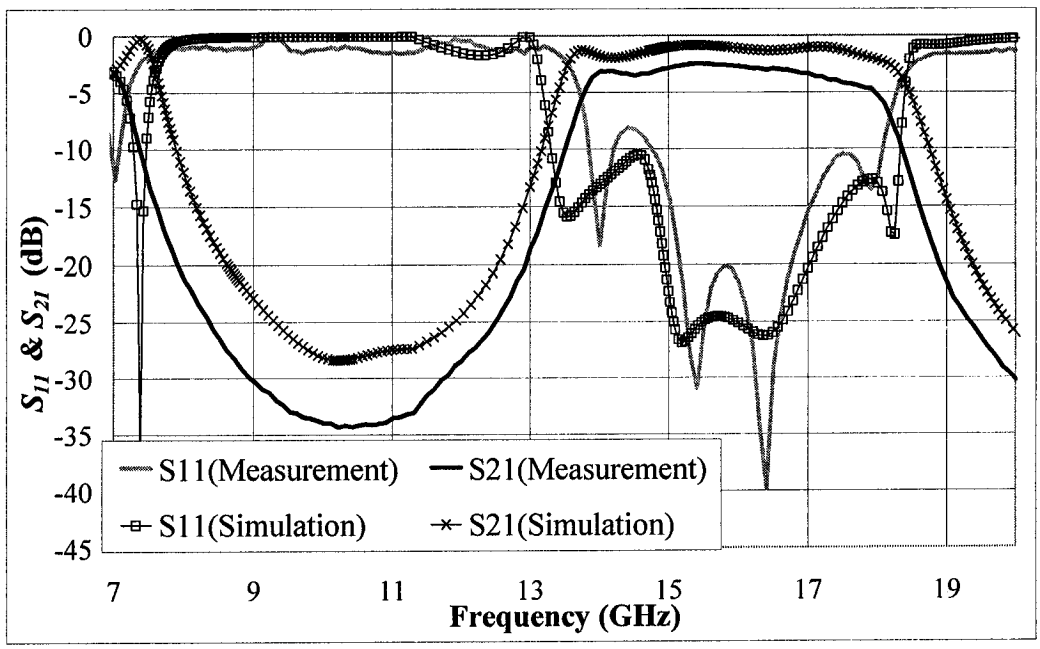

Fig. 3-6: Comparison of simulated and measured results for the standard EBG structure.

3.1.4. SUMMARY

A new characteristic of the planar EBG structure was found by varying the width and length of the rectangular perforation patterns. The structure period (a) primarily determines the position of the stopbands. Meanwhile, the ratio of w_p/a and l_m were set

to be one-eighth of the guided wavelength in order to obtain a passband region. The proposed EBG structure has a unique property of double-stopband and it can be utilized as a bandpass filter. It has been demonstrated both by simulation and experiment that the characteristic of the double-stopband effect can be achieved. Moreover, it has been shown by simulation that reducing the overall size of the ground perforations can control the location of the passband frequency. Therefore, a bandpass filter can be constructed easily and efficiently by utilizing the EBG structure.

3.2. TAPERED SLOT-ARRAY EBG STRUCTURES

In this section, an innovative tapered array (TA) pattern that is used to construct an EBG structure is proposed. Tapered array patterns not only provide distinctive passband and stopband regions, but also the position of cutoff frequency can be controlled very easily. In addition, the stopband region provided by the tapered array patterns is much wider and the structural dimension is more compacted than regular periodic patterns and any other proposed tapered structures in the literatures. Fig. 3-7 shows a typical planar EBG structure with linearly tapered array pattern inside of a ground plane of a microstrip transmission line.

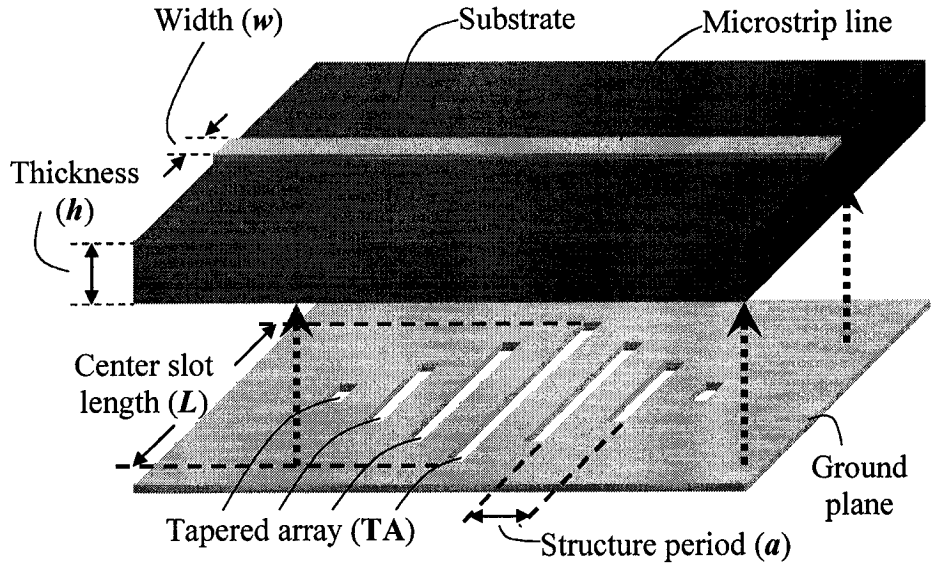

Fig. 3-7: An EBG structure constructed with 7-slot linearly tapered array pattern implemented in the ground plane.

The design and analysis of the linearly TA patterned EBG structures are firstly discussed. The simulation and measurement results showing the dependence of the transmission and reflection performances on the structure period (***a***), number of slots (***n***), and the center slot length (***L***) are presented. Then, the improved design, which is consisted of non-linearly tapered slot-array, is investigated and studied. In both linear and non-linear cases, actual EBG samples were fabricated to verify the initial designs.

3.2.1. LINEARLY TAPERED SLOT ARRAY

3.2.1.1. DESIGN TECHNIQUE

Tapered array pattern consists of a periodic array of slots, whose lengths are linearly tapered toward the ends. This critical characteristic allows the traveling electromagnetic waves to be exposed to periodic interferences progressively and

therefore it is possible to obtain much defined regions of passband and stopband in a frequency response. This indicates that the transmission and reflection performances of the structure are very good. The parameters for the preliminary design are shown in Fig. 3-8.

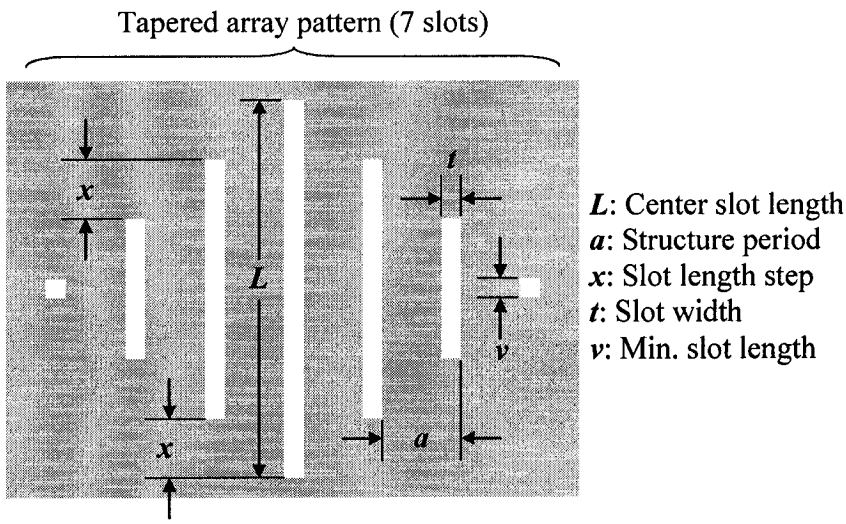

Fig. 3-8: A 7-slot tapered array pattern showing preliminary design dimensions.

In order to understand the TA patterned EBG structure better, the slots can be modeled with resistor-inductor-capacitor (RLC) resonator equivalent circuits. Fig. 3-9 shows a circuit representation of a 7-slot TA patterned EBG structure with microstrip transmission lines in between. The grey components represent the microstrip transmission line in the TA patterned EBG structure, which can be characterized by series inductors and shunt capacitor. The slots are modeled with RLC network where RL_4C_4 represents the center slot.

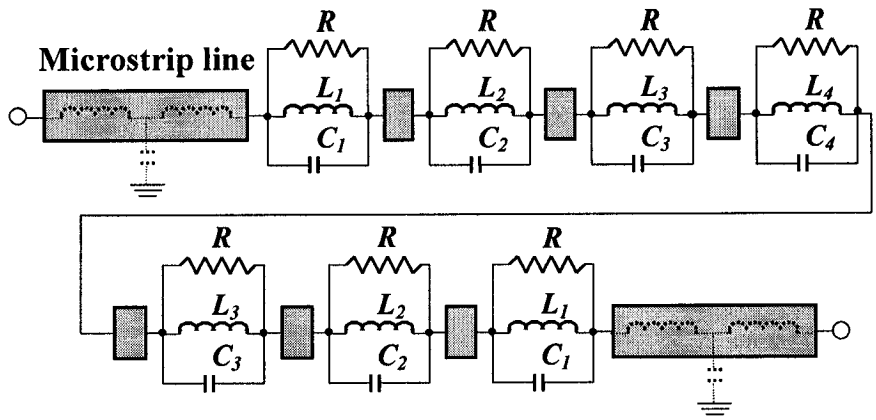

Fig. 3-9: Equivalent circuit representation for a 7-slot TA patterned EBG structure. (R = 1500 Ω, L_4 = 1.45 nH, C_4 = 0.145 pF, L_3 = 1.00 nH, C_3 = 0.10 pF, L_2 = 0.55 nH, C_2 = 0.055 pF, L_1 = 0.10 nH, and C_1 = 0.01 pF)

Fig. 3-10 shows the comparison of S-parameters between the equivalent circuit model and the actual measurement of the sample. It is observed that the S-parameters match fairly well. Therefore, the equivalent circuit model serves as a good preliminary design tool and representation for the actual TA patterned EBG structure.

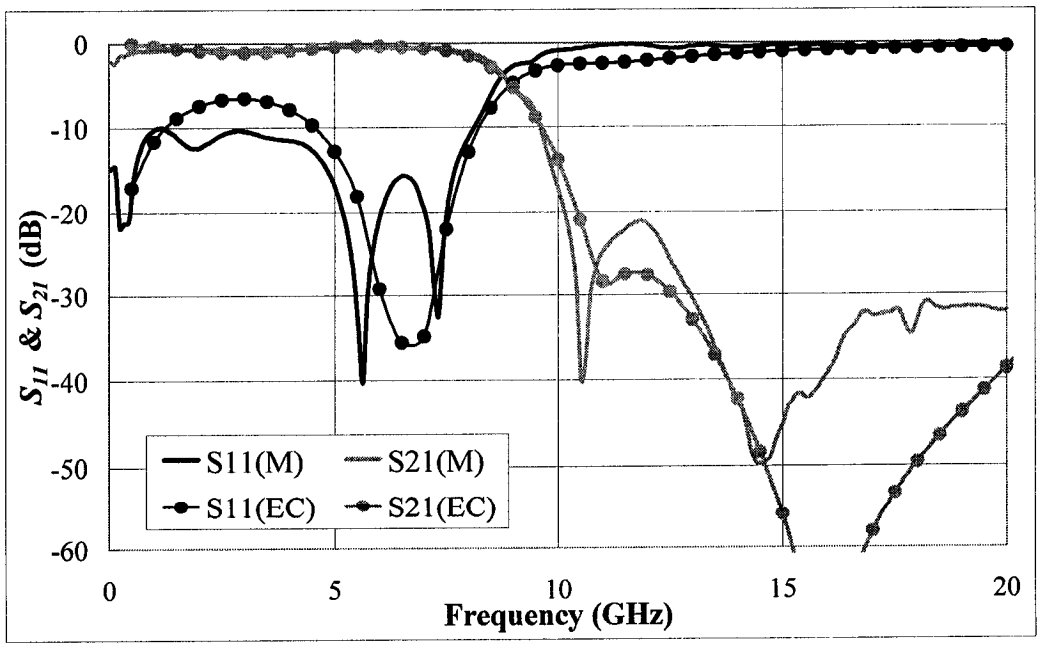

Fig. 3-10: Comparison of S_{21}/S_{11} between equivalent circuit model (EC) and measurement (M) results for a 7-slot tapered array pattern EBG structure with L = 7.7 mm.

To characterize the tapered array pattern and its stopband performance, three parameters were chosen to be analyzed: the structure period (a), the number of slots (n), and the center slot length (L) mainly because these three structural parameters describe the essence of the EBG structure. TABLE 3-III shows a simulation overview on how the data sets were obtained and analyzed.

TABLE 3-III: SIMULATION DATA SETS

Data Sets	Structure period (a)	Number of Slots (n)	Center slot length (L)
Trial #1	1 ~ 2.5 *mm*	7-Slots	7.7 *mm*
Trial #2	2 *mm*	5-, 7- 9-slots	10.1 *mm*
Trial #3	2 *mm*	7-Slots	1.7 ~ 12.5 *mm*

The performance of each case is measured in terms of S-parameters. Consequently, the S-parameters indicate the vital characteristics of an EBG structure such as passband width, cutoff frequency, passband insertion loss and stopband attenuation. Fig. 3-11 shows the critical characteristics mentioned above on a typical S-parameter diagram with S_{11} and S_{21} responses.

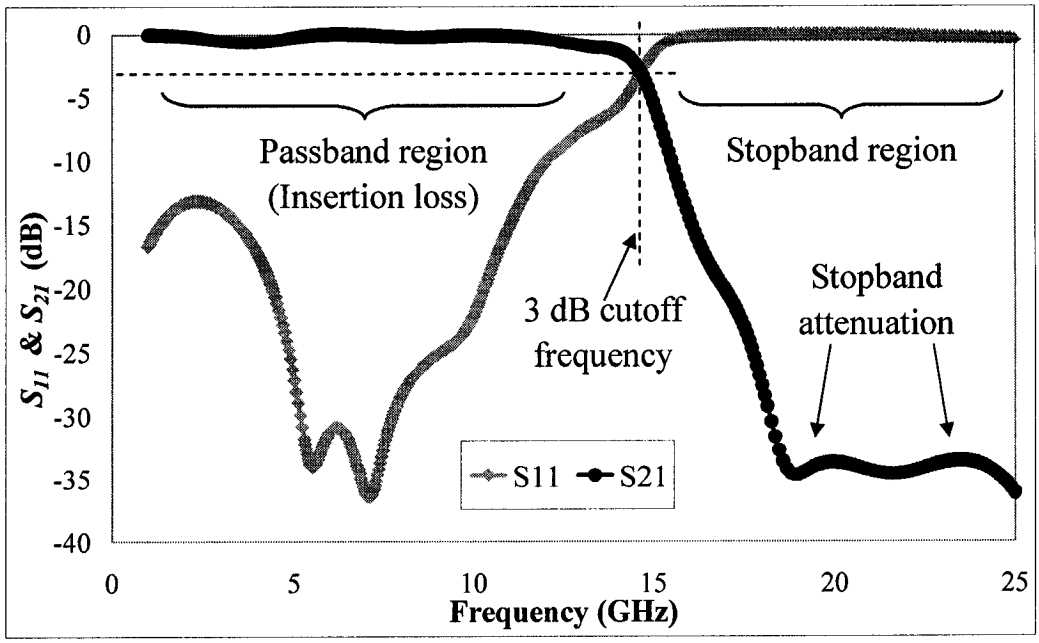

Fig. 3-11: A typical S-parameters diagram showing critical characteristics of an EBG structure.

3.2.1.2. SIMULATION RESULTS

All of the simulations were performed with Agilent Advanced Design System's Momentum simulator, which utilizes the method of moments to simulate the microwave structures. The global simulation parameters are shown in TABLE 3-IV, primarily the properties of dielectric substrate and the microstrip line width, which are the same for each trial. Finite ground plane structure is used for all the simulation models to provide more realistic S-parameter results.

TABLE 3-IV: GLOBAL SIMULATION PARAMETERS FOR ALL TRIALS

Substrate type	Alumina (Al_2O_3)
Dielectric constant (ε_r)	9.8
Substrate thickness (h)	250 μm
Microstrip line width (w)	250 μm

Trial #1 – Varying the structure period

The structure period (*a*) is defined as the distance between the centers of each slot. In this trial, *a* is varied from 1 *mm* to 2.5 *mm* with incremental steps of 0.5 *mm*. Meanwhile, other dimensions were unchanged, which are summarized in TABLE 3-V.

TABLE 3-V: PARAMETERS USED FOR SIMULATIONS IN TRIAL #1

Number of slots (*n*)	7
Center slot length (*L*)	7.7 *mm*
Structure period (*a*)	1, 1.5, 2, and 2.5 *mm*
Slot length step (*x*)	1.2 *mm*
Slot width (*t*)	0.5 *mm*
Minimum slot length (*v*)	0.5 *mm*

Fig. 3-12 shows the simulation results of S_{21} and S_{11} responses for each structure period, *a*.

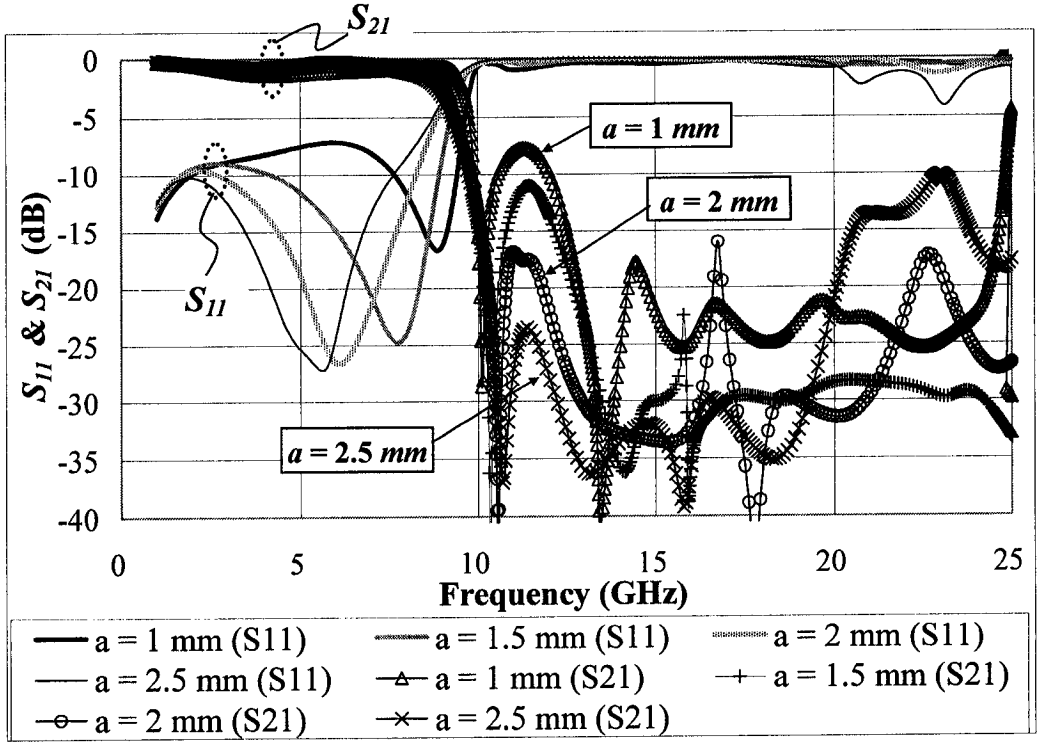

Fig. 3-12: Simulation results of S_{21} and S_{11} responses for trial #1.

From Fig. 3-12, it is observed that a passband region lies up to around 9 *GHz*,

while a defined stopband region is obtained from around 10 *GHz* and onwards. Also, in the stopband region, S_{21} at 11.5 *GHz* is highly dependent on a. This stopband attenuation increases as a is increased. Thus, it indicates that a wider structure period permits better stopband ability at this frequency region. Furthermore, in the passband region, it is observed that the insertion loss (S_{21}) decreases as a is increased. However, stopband performance degrades as the frequency is increased beyond 20 *GHz*.

In ordinary microwave EBG structures, the structure period (a) is an important indicator for the center of the stopband region because of the Bragg's law. In this case, Bragg's condition predicts that the center of the stopband for a equals to 1 *mm* and 2.5 *mm* are at 58 *GHz* and 23 *GHz* respectively. However, Bragg's condition does not predict the stopband width and the cutoff frequencies (i.e., frequency of stopband edges). Therefore, the effect of the structure period a is not obvious in the case of TA patterned EBG structures below 25 *GHz*.

TABLE 3-VI shows a detailed data set on the 3 *dB* cutoff frequency, the maximum passband insertion loss, and the minimum stopband attenuation for each simulated structure period. For the minimum stopband attenuation, the data were obtained for values below 20 *GHz*.

TABLE 3-VI: SUMMARIZED SIMULATION RESULTS FOR TRIAL #1

	1 *mm*	1.5 *mm*	2 *mm*	2.5 *mm*
3 dB cutoff freq. (*GHz*)	9.01	9.01	9.29	9.65
Max. passband insertion loss (*dB*)	1.39	1.21	0.95	0.76
Min. stopband attenuation (*dB*)	7.71	11.10	16.00	20.90

The structure period (***a***) affects the quality of passband and stopband region in terms of insertion loss and attenuation respectively. However, it is not very influential on the cutoff frequency. Therefore, other aspects of the tapered array pattern have to be examined to realize the control of the cutoff frequency.

Trial #2 – Varying the number of slots

The number of slots (***n***) is varied in this trial. Slots are rectangular perforations in the ground plane with various dimensions. In this trial, two cases relate to ***n*** are investigated. The first case has the conditions where the center slot length (***L***) and the minimum slot length (***v***) are kept constant. Thus, the slot length step (***x***) is different for each ***n***. The second case simply reduces the number of slots from the sides and therefore ***x*** remains the same for each ***n***. Fig. 3-13 illustrates the variation parameters for two cases accordingly. The dimensions utilized in this trial are summarized in TABLE 3-VII.

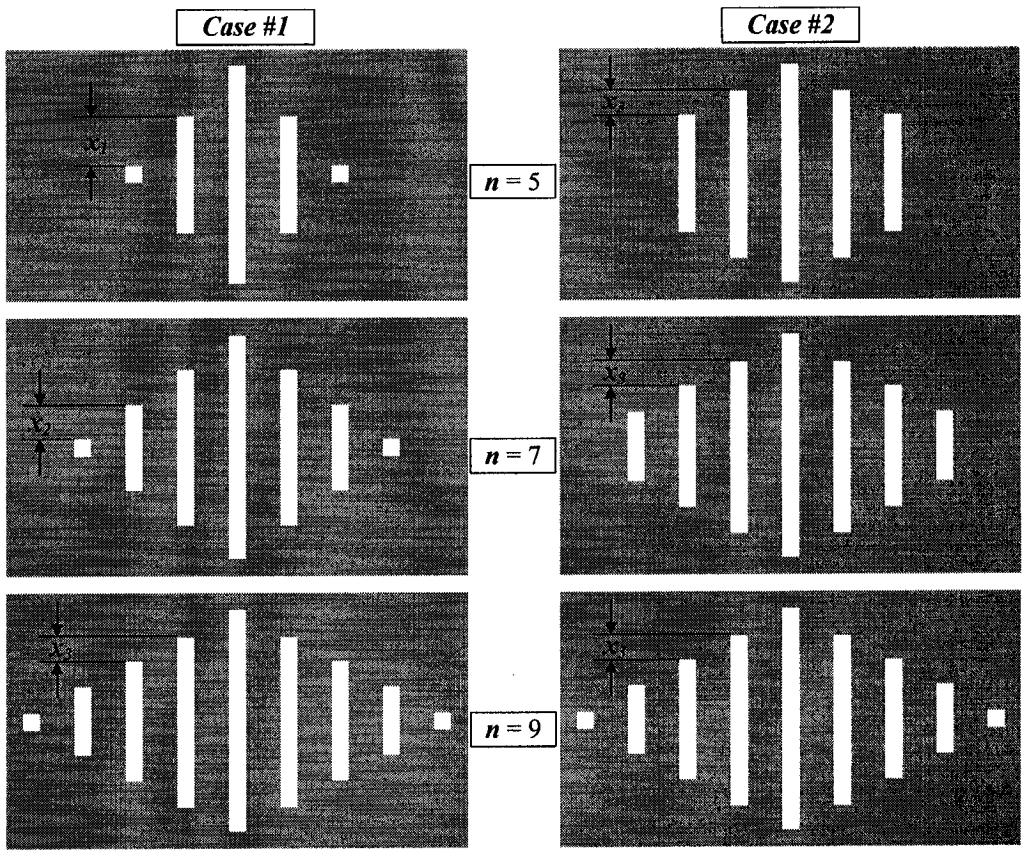

Fig. 3-13: Schematics of the varying slots in the ground plane.

TABLE 3-VII: PARAMETERS USED FOR SIMULATIONS IN TRIAL #2

	Case #1	Case #2
Number of slots (*n*)	5, 7, 9	5, 7, 9
Center slot length (*L*)	10.1 *mm*	10.1 *mm*
Structure period (*a*)	2 *mm*	2 *mm*
Slot length step (*x*)	2.4, 1.6, and 1.2 *mm*	1.2 *mm*
Slot width (*t*)	0.5 *mm*	0.5 *mm*
Minimum slot length (*v*)	0.5 *mm*	5.3, 2.9, and 0.5 *mm*

Fig. 3-14 shows the simulation results for Case #1, where the minimum slot length was kept constant while *n* varied.

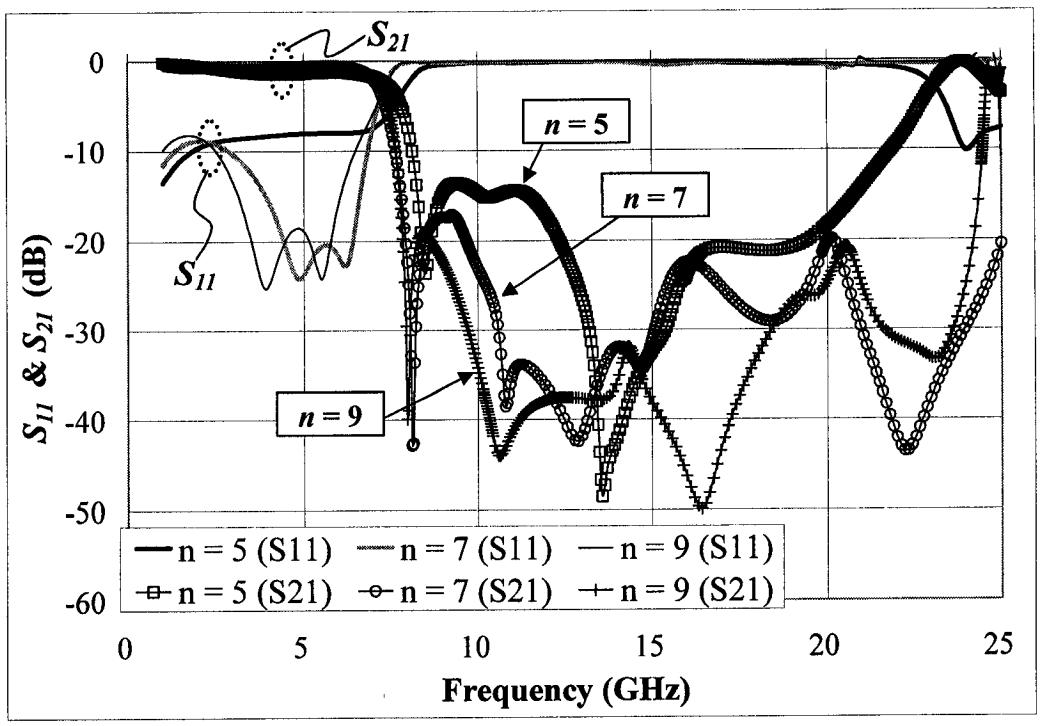

Fig. 3-14: Simulation results of Case #1, where v is fixed and n = 5, 7, and 9.

From Fig. 3-14, a passband region is observed up to 7 *GHz*, while a well-defined stopband region follows. Also, in the stopband region, the attenuation (S_{21}) generally increases as n is decreased. This indicates that a higher number of slots offer a better defined stopband region. Furthermore, in the passband region, it is seen that the insertion loss (S_{21}) up to 2.3 *GHz* decreases as n is decreased. Beyond 2.3 *GHz*, the insertion loss increases significantly for n = 5. TABLE 3-VIII shows a detailed data set on the 3 *dB* cutoff frequency, the maximum passband insertion loss, and the minimum stopband attenuation for each n. For the minimum stopband attenuation, the data were obtained for values below 20 *GHz*.

TABLE 3-VIII: SUMMARIZED SIMULATION RESULTS FOR TRIAL #2, CASE #1

	$n = 5$	$n = 7$	$n = 9$
3 dB cutoff frequency	7.50 *GHz*	7.14 *GHz*	7.25 *GHz*
Max. passband insertion loss	1.49 *dB*	0.93 *dB*	0.95 *dB*
Min. stopband attenuation	13.6 *dB*	17.3 *dB*	19.3 *dB*

Fig. 3-15 shows the simulation results for Case #2, where x was kept constant while n varied.

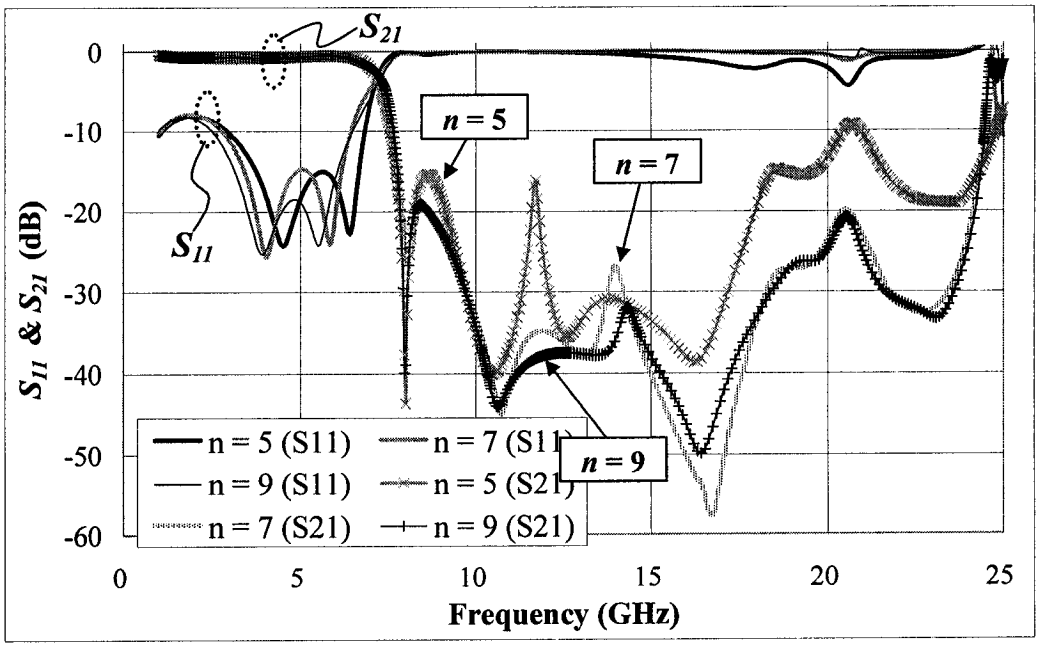

Fig. 3-15 Simulation results for Case #2, where x was fixed and n = 5, 7, and 9.

From Fig. 3-15, similar results are observed as in Fig. 3-14. However, the insertion loss in the passband region for n = 5 is much better than in Case #1. On the other hand, the stopband region of the S_{11} starts to degrade at around 16 *GHz*, compared to 20 *GHz* in Case #1. Therefore, it is noticed that the slots with shorter length (i.e., the outer slots) were mainly responsible for stopband effect at higher frequencies. For Case #1, since some slots with medium length were taken away as n is decreased, the stopband effect started to degrade at around 9 *GHz* to 12 *GHz*. Hence

from this trial, the correlation of the slot length with respect to stopband frequency is starting to emerge. TABLE 3-IX shows a detailed data set on the 3 *dB* cutoff frequency, the maximum passband insertion loss, and minimum stopband attenuation for each ***n***. For minimum stopband attenuation, the data were obtained for values below 20 *GHz*.

TABLE 3-IX: SUMMARIZED SIMULATION RESULTS FOR TRIAL #2, CASE #2

	***n* = 5**	***n* = 7**	***n* = 9**
3 dB cutoff frequency	7.14 *GHz*	7.05 *GHz*	7.25 *GHz*
Max. passband insertion loss	0.90 *dB*	0.90 *dB*	0.79 *dB*
Min. stopband attenuation	14.9 *dB*	19.0 *dB*	19.2 *dB*

Trial #3 – Varying the center slot length

The center slot length (***L***) is defined as the longest slot in the middle of the tapered array pattern. In this trial, ***L*** is varied from 1.7 ~ 12.5 *mm* to analyze the effect of this dimension with respect to the stopband characteristics. Fig. 3-16 shows a schematic of the variations. Meanwhile, other dimensions were unchanged, which are summarized in TABLE 3-X.

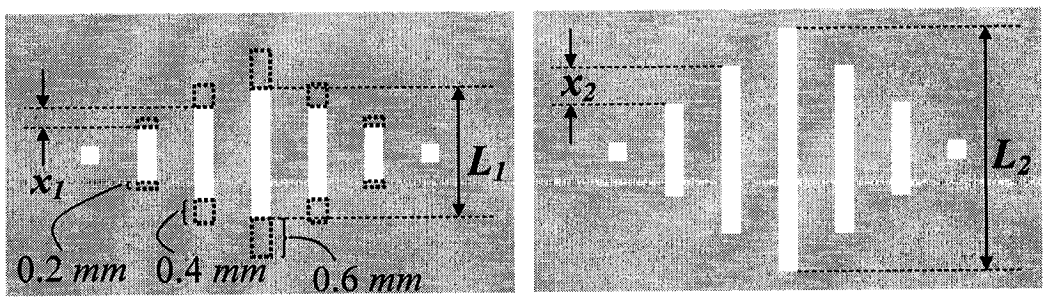

Fig. 3-16: Center slot length of the TA patterned EBG structure was varied linearly in this trial.

Since the lengths of the first and last slots are to be kept constant for the stopband

effect to be distributed evenly through out a wide range of frequency, the slot length step (x) has to be increased for every center slot length (L). There were a total of ten different L, which were simulated in this trial. In each variation, L was increased by 1.2 *mm*. The 3rd and 5th slots were increased by 0.8 *mm* while the 2nd and 6th slots were increased by 0.4 *mm*. Therefore x was increased by 0.2 *mm* in each variation of L.

TABLE 3-X: PARAMETERS USED FOR SIMULATIONS IN TRIAL #3

Number of slots (n)	7
Center slot length (L)	1.7 ~ 12.5 *mm*
Structure period (a)	2 *mm*
Slot length step (x)	0.2 ~ 2.0 *mm*
Slot width (t)	0.5 *mm*
Minimum slot length (v)	0.5 *mm*

Fig. 3-17 shows the simulation results of S_{21}. Each curve refers to a different L.

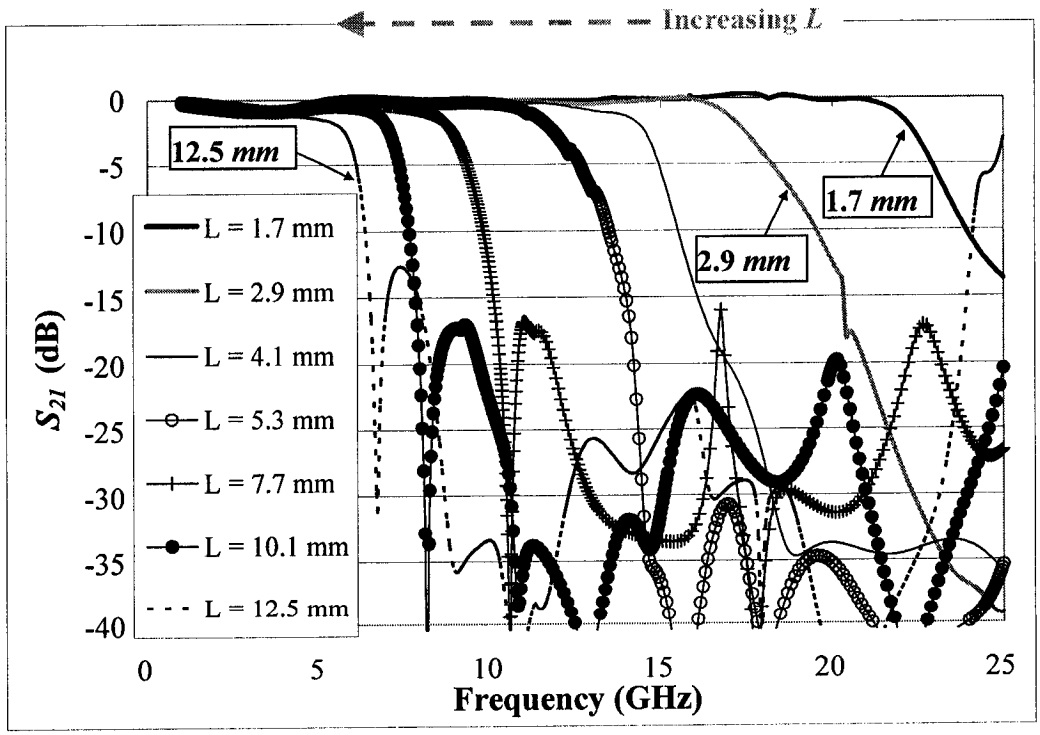

Fig. 3-17: Simulation results of S_{21} for variation of L.

First of all and most significantly, Fig. 3-17 shows that the cutoff frequency

decreases as L is increased. Also, the insertion loss in the passband region increases as L is increased. This demonstrates that the passband region is highly dependent on L. As the center slot length increases, the series inductance and capacitance represented by the slot are increased. Therefore, the cutoff frequency of the lowpass network represented by the tapered slot-array pattern is decreased as the slot length increases. Thus a stopband region is created and it has a cutoff frequency that is highly dependent on the center slot length. It is noted that the S_{21} response for L = 1.7 *mm* and 2.9 *mm* showed unphysical results of beyond 0 *dB* towards the higher end of the frequency span. This is due to the limitation of the simulation software on the calibration of the ports.

Furthermore, the attenuation in the stopband region is generally around 20 *dB*. The simulation results for S_{11} are shown in Fig. 3-18. TABLE 3-XI presents detailed values for 3 *dB* cutoff frequency, the maximum passband insertion loss, and the minimum stopband attenuation. For the minimum stopband attenuation, the data were obtained for values below 20 *GHz*.

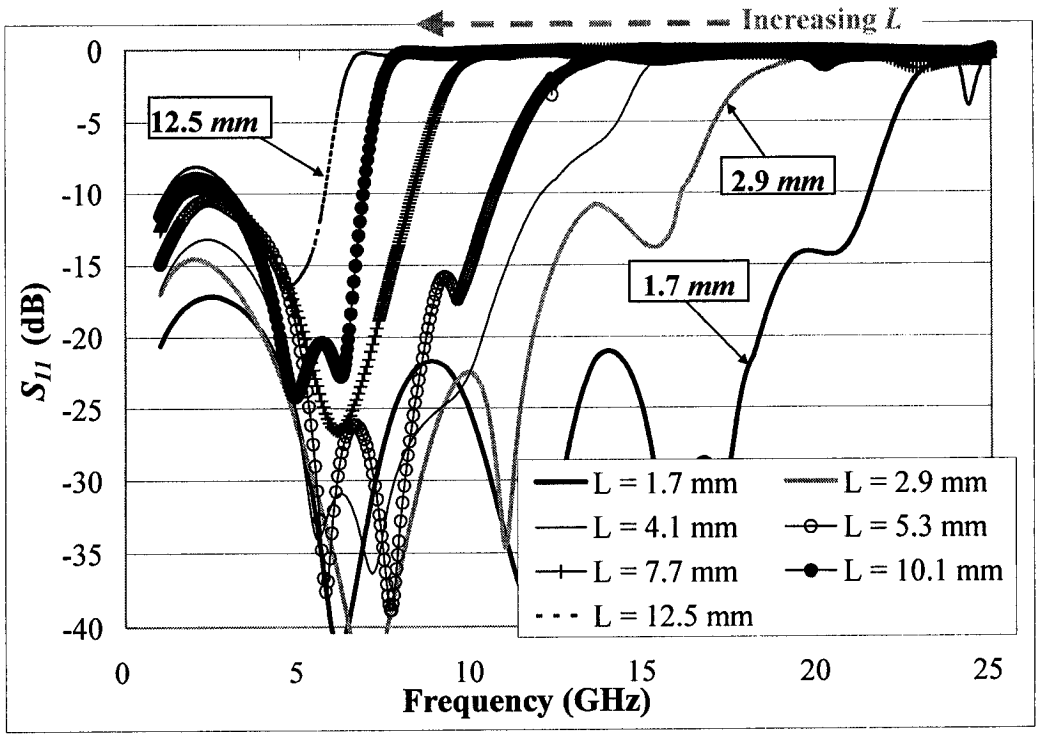

Fig. 3-18: Simulation results of S_{11} for variation of L.

TABLE 3-XI: SUMMARIZED SIMULATION RESULTS FOR TRIAL #3

Center slot length, L	3 *dB* cutoff frequency	Max. passband insertion loss	Min. stopband attenuation
1.7 mm	22.5 *GHz*	0.56 *dB*	--
2.9 mm	17.6 *GHz*	0.54 *dB*	--
4.1 mm	14.6 *GHz*	0.67 *dB*	33.8 *dB*
5.3 mm	12.0 *GHz*	0.87 *dB*	30.8 *dB*
6.5 mm	10.0 *GHz*	0.77 *dB*	25.6 *dB*
7.7 mm	9.0 *GHz*	0.95 *dB*	16.0 *dB*
8.9 mm	7.9 *GHz*	1.04 *dB*	19.1 *dB*
10.1 mm	7.1 *GHz*	0.93 *dB*	17.2 *dB*
11.3 mm	6.5 *GHz*	1.12 *dB*	12.7 *dB*
12.5 mm	5.9 *GHz*	1.16 *dB*	12.7 *dB*

Since L is a very effective parameter to determine the cutoff frequency, Fig. 3-19 plots the relationship between them (Cutoff frequency versus L).

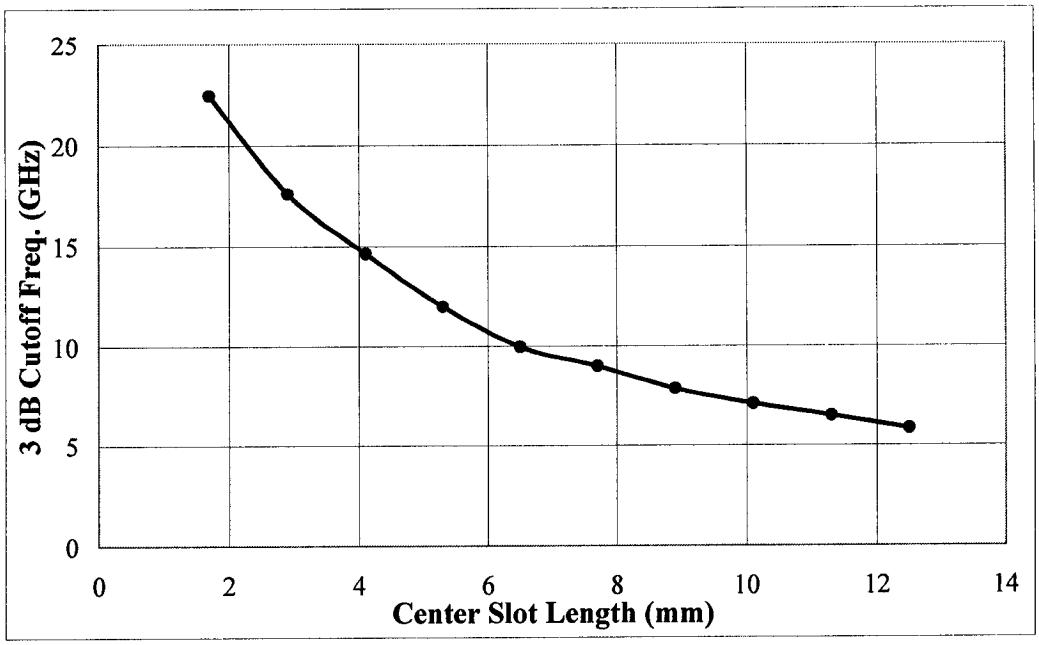

Fig. 3-19: The relationship between ***L*** and the cutoff frequency.

Based on the simulation results, it is concluded that the 3 *dB* cutoff frequency is highly dependent on the center slot length, ***L***. It is observed that as ***L*** increases, the 3 *dB* cutoff frequency is decreased. Therefore, the passband and stopband regions can be controlled very easily with the TA patterned EBG structures. Also, from TABLE 3-XI, in most cases the maximum insertion loss in the passband region is below 1 *dB*. Hence, the quality of the filter performance is maintained while the cutoff frequency can be controlled. Moreover, the overall length of the device does not increase as the cutoff frequency is decreased.

3.2.1.3. EXPERIMENTAL MEASUREMENTS AND COMPARISONS

To validate the simulation results, a few samples of the TA patterned EBG structures were fabricated and measured. The samples were fabricated on Alumina

substrates with the same structural properties shown in TABLE 3-IV. Please refer to Appendix C for detailed fabrication and measurement procedures.

Fig. 3-20 illustrates two samples having 7-slot linearly TA patterns implemented in the ground plane of a microstrip transmission line structure.

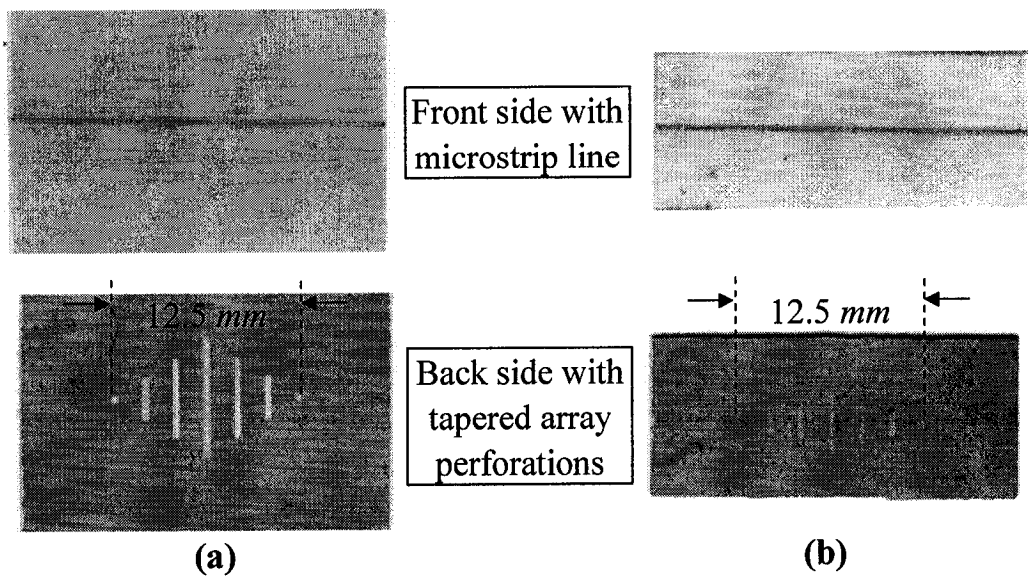

Fig. 3-20: Fabricated 7-slot linearly TA patterned EBG structures with (a) L = 7.7 *mm* and (b) L = 4.1 *mm*.

Two comparisons are shown to illustrate the effect of varying the center slot length, L. Fig. 3-21 shows the comparison between the simulation and the measurement results for the case of 7-slot TA patterned EBG with L = 7.7 *mm*.

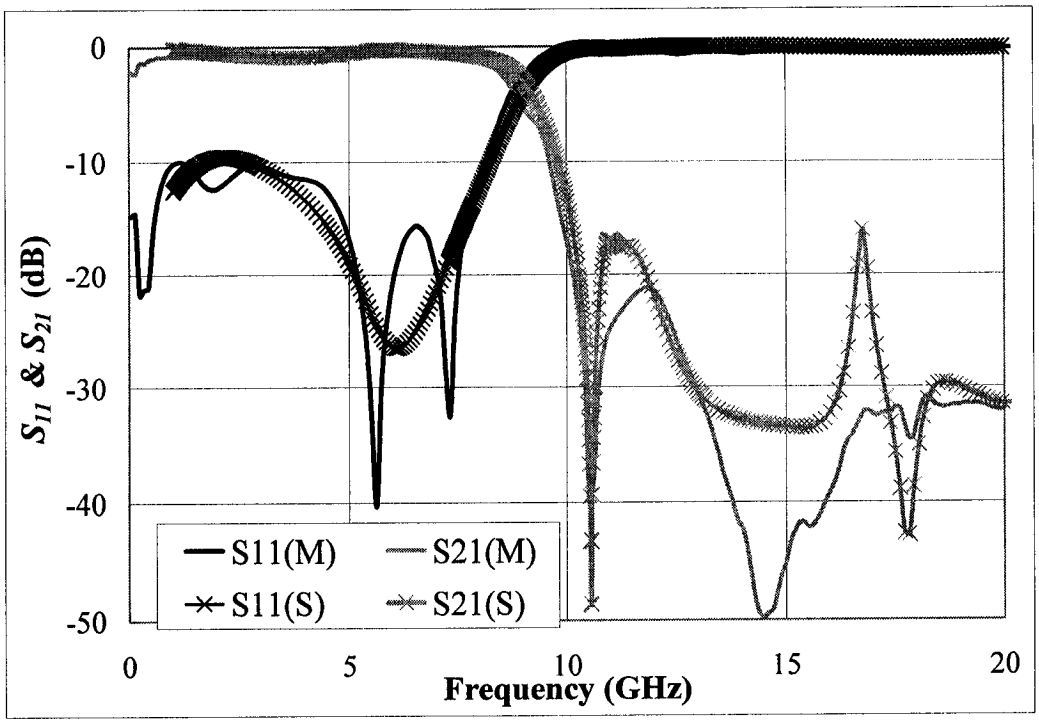

Fig. 3-21: Comparison of S_{21}/S_{11} between simulation (S) and measurement (M) results for the 7-slot TA patterned EBG structure with L = 7.7 *mm*.

It is observed from Fig. 3-21 that the measurement results match very well with the simulation ones. The 3 *dB* cutoff frequencies in two cases differ only by 0.4 *GHz*. Therefore, the passband and stopband width are very similar. Also from the graph, it can be seen that the insertion loss in the passband region and the attenuation in the stopband region generally have the same behavior, which is a solid indication that the simulation results are very accurate. Fig. 3-22 further illustrates the strong dependence of the cutoff frequency on the center slot length (L), which was reduced to 4.1 *mm*.

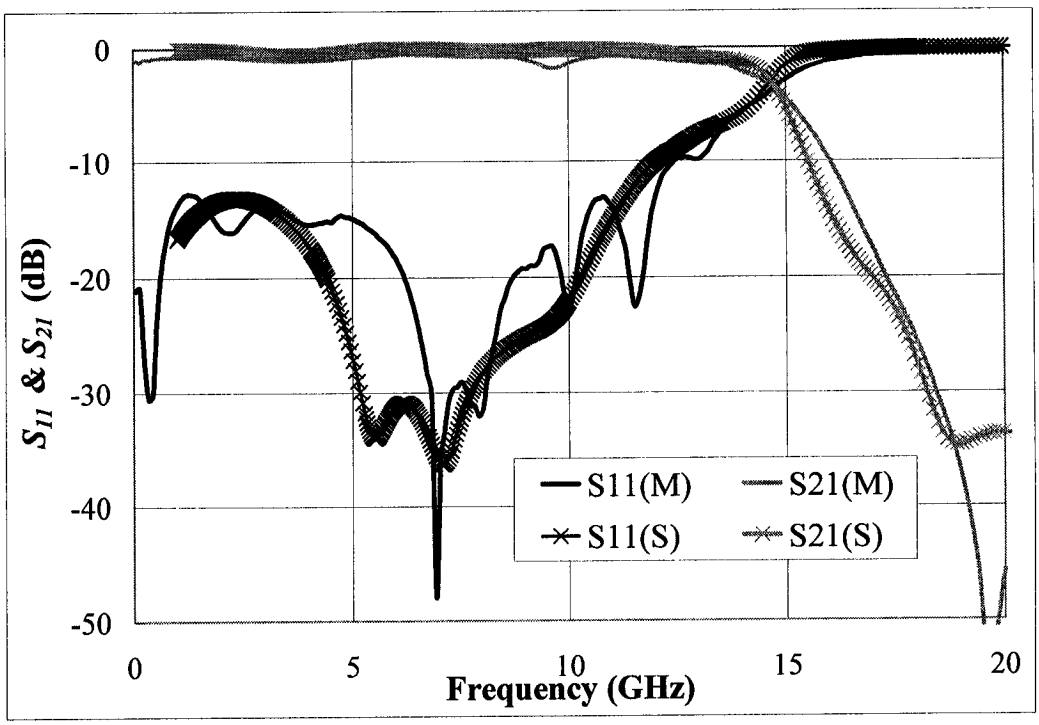

Fig. 3-22: Comparison of S_{21}/S_{11} between simulation (S) and measurement (M) results for the 7-slot TA patterned EBG structure with L = 4.1 *mm*.

In Fig. 3-22, the difference between simulation and measurement results in 3 *dB* cutoff frequencies is only 0.1 *dB*. Also, it is clearly shown that the cutoff frequency shifted roughly from 9 *GHz* to 15 *GHz* when compared with Fig. 3-21. Therefore, this confirms that the center slot length (L) and the cutoff frequency are highly correlated. From the measurement results, it is concluded that the simulation results are very reliable and they provide a good prediction on the designs of the new TA patterned EBG structures.

3.2.2. NON-LINEARLY TAPERED SLOT ARRAY

3.2.2.1. DESIGN TECHNIQUE AND SIMULATIONS

The most unique characteristic of TA patterned EBG structure is that it is

consisted of a periodic array of slots with different lengths. Fig. 3-23 illustrates the difference between linearly and non-linearly TA patterns.

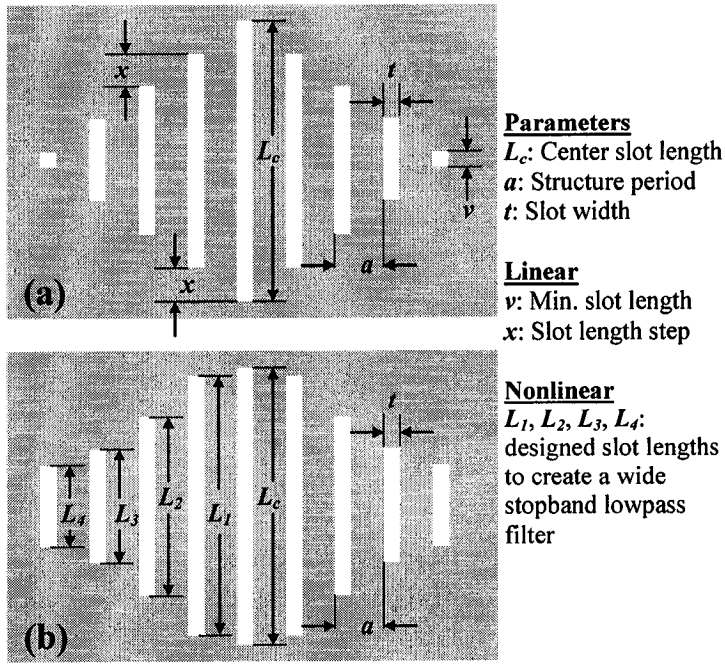

Fig. 3-23: (a) Linearly and (b) non-linearly 9-slot TA patterned EBG structure implemented in the ground plane of a microstrip transmission line.

The general performance of TA patterned EBG structure can be demonstrated through the linear configuration. However, to fully utilize the TA patterned EBG structure in any specific application, non-linear configuration can be used to maximize the stopband effect at a wide range of frequency. In this section, the design of a non-linearly TA pattern with stopband from 9.3 *GHz* to 20 *GHz* is studied and verified. In order to model the non-linearly tapered array pattern, RLC equivalent circuit is used to represent each slot. Simulations were performed with Agilent Advanced Design System. Fig. 3-24 shows the equivalent circuit and the layout of a single slot.

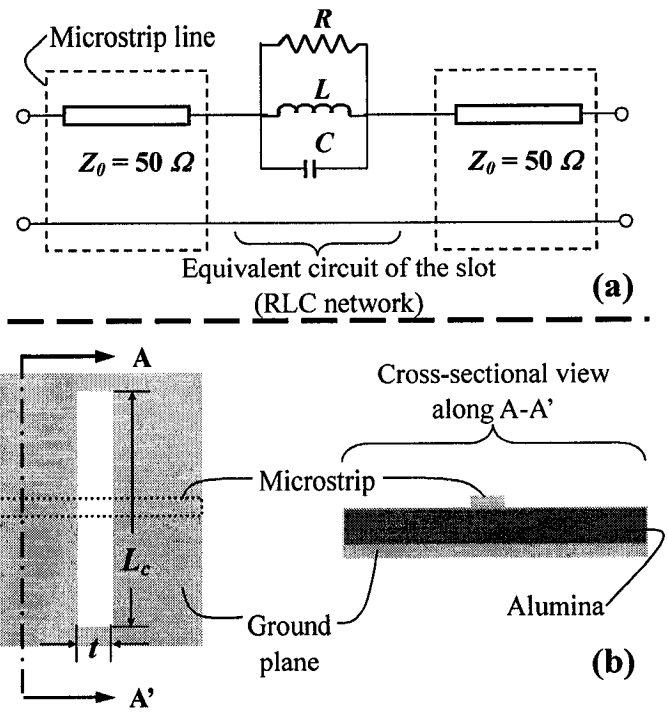

Fig. 3-24: (a) Equivalent circuit with R = 500 Ω, L = 1.3 nH, and C = 0.15 pF, and (b) layout of the center slot with L_c = 7.9 mm and t = 0.5 mm (microstrip line width = 0.25 mm and thickness of Alumina = 0.25 mm)

Fig. 3-25 shows the comparison of the S-parameters between the equivalent circuit model and simulation results from the layout.

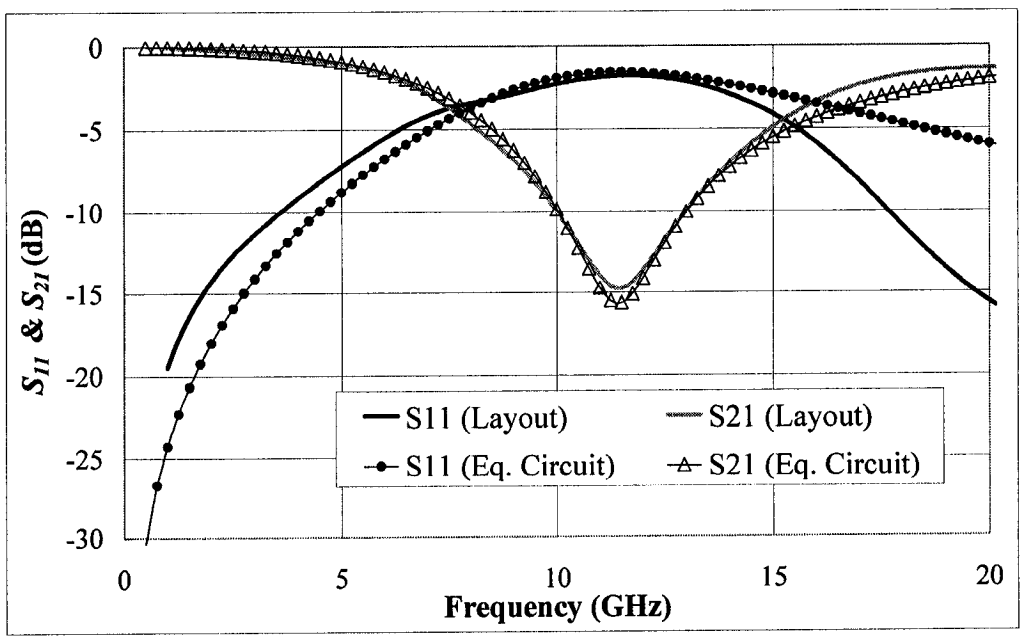

Fig. 3-25: A comparison of S-parameters between the equivalent circuit model and the layout design for the center slot length, L_c = 7.9 mm.

From Fig. 3-25, it is noticed that the RLC equivalent circuit models the slot perforation fairly well. Therefore, it is possible to find the rest of the slot lengths (L_1, L_2, L_3, and L_4) using this technique and construct a wide stopband lowpass filter. The dimensions of the non-linearly TA patterned EBG structure, which can be utilized as a wide stopband lowpass filter, are summarized in TABLE 3-XII.

TABLE 3-XII: DIMENSIONS OF NON-LINEARLY TAPERED ARRAY PATTERN

Number of slots (n)	9
Center slot length (L)	7.9 *mm*
Structure period (a)	1.5 *mm*
Slot lengths (L_1, L_2, L_3, and L_4)	7.4, 5.7, 4.5, and 3.7 *mm*
Slot width (t)	0.5 *mm*

The simulation results of S_{21} of each slot, as well as the complete 9-slot non-linearly TA patterned EBG structure, are shown in Fig. 3-26.

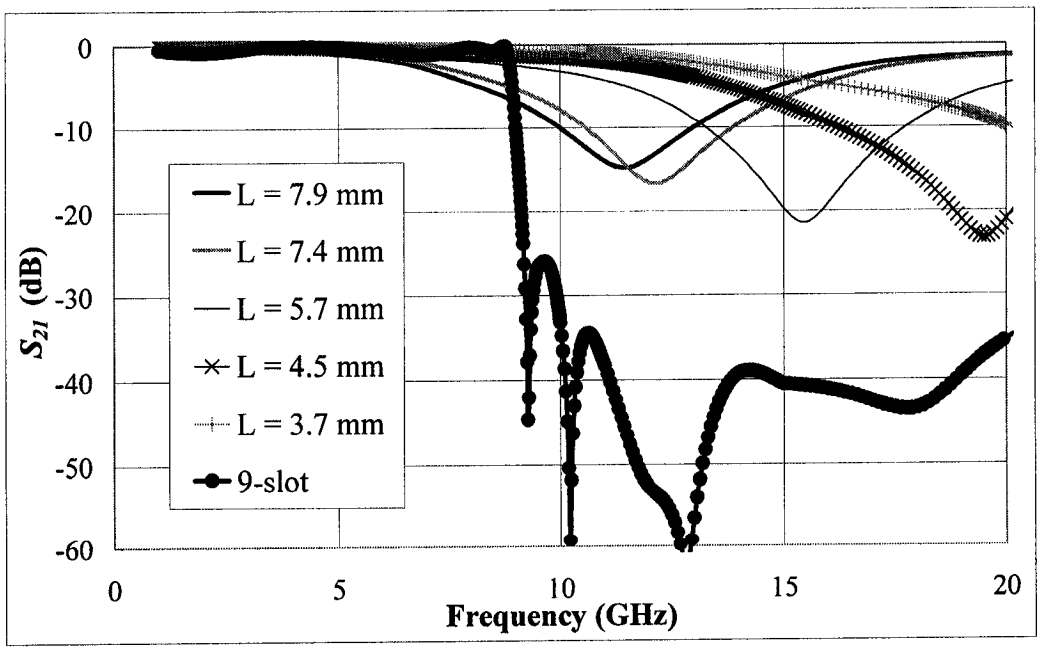

Fig. 3-26: S_{21} results for both single slot (L = 7.9, 7.4, 5.7, 4.5, and 3.7 *mm*) and 9-slot non-linearly TA patterned EBG structure.

It is seen from Fig. 3-26 that the overall 9-slot non-linearly TA patterned EBG

structure has a very flat passband up to 9 *GHz* and a stopband with high attenuation up to 20 *GHz*. Therefore, the simulation results show promising performance for the non-linearly TA patterned EBG structure to be utilized as a microwave lowpass filter with an exceptionally wide stopband. To illustrate the significance of the non-linearly tapered structure, Fig. 3-27 shows the simulation results of S_{21} of both linearly and non-linearly TA patterned EBG structure.

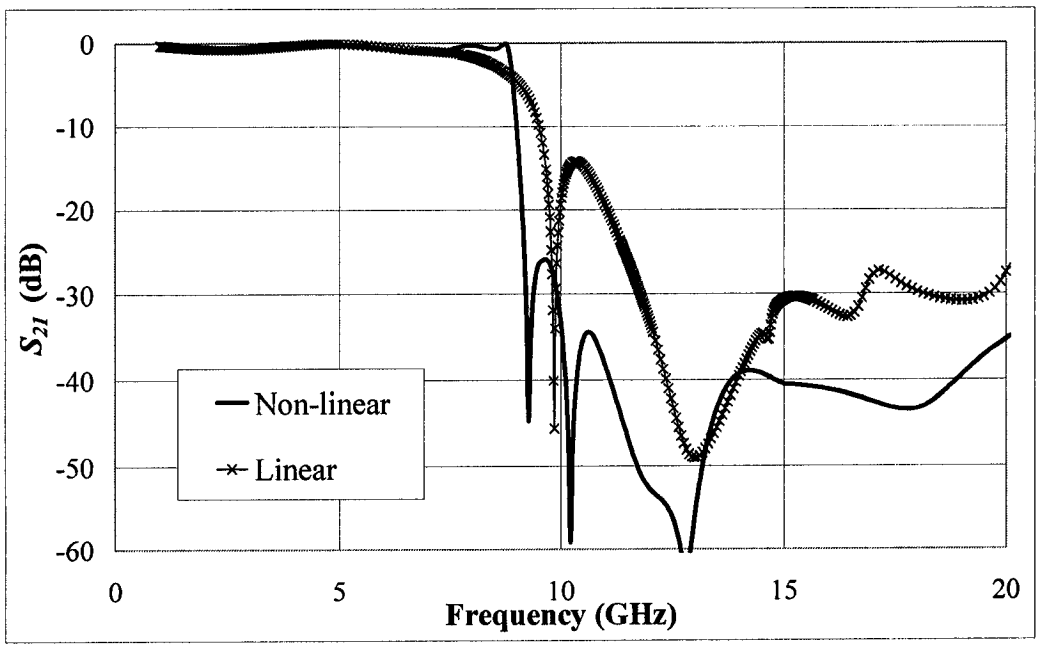

Fig. 3-27: S_{21} results for both linearly and non-linearly 9-slot TA patterned EBG structures.

It is observed from Fig. 3-27 that the non-linear structure has a superior stopband performance, especially near the stopband edge at 9.5 *GHz* and 10.5 *GHz* where the attenuation is 20 *dB* more than the linearly tapered structure. Also, the non-linearly tapered structure has a more defined passband edge, which allows a better transmission near the cutoff frequency.

Furthermore, the overall dimension of the EBG structure is significantly smaller when the non-linearly TA pattern is used instead of the ordinary rectangular pattern. To construct an EBG structure with a stopband region centered at around 12 *GHz* (cutoff frequency is around 9 *GHz*) by utilizing the conventional rectangular perforations, the structure period (***a***) can be calculated according to Eq. 3-2 and it is equal to 4.8 *mm*. Assuming that the substrate is Alumina with an dielectric constant (ε_r) of 9.8, which is also the same material used for non-linearly TA patterned EBG structure. Fig. 3-28 illustrates both the conventional rectangular EBG pattern and the non-linearly TA pattern for comparison.

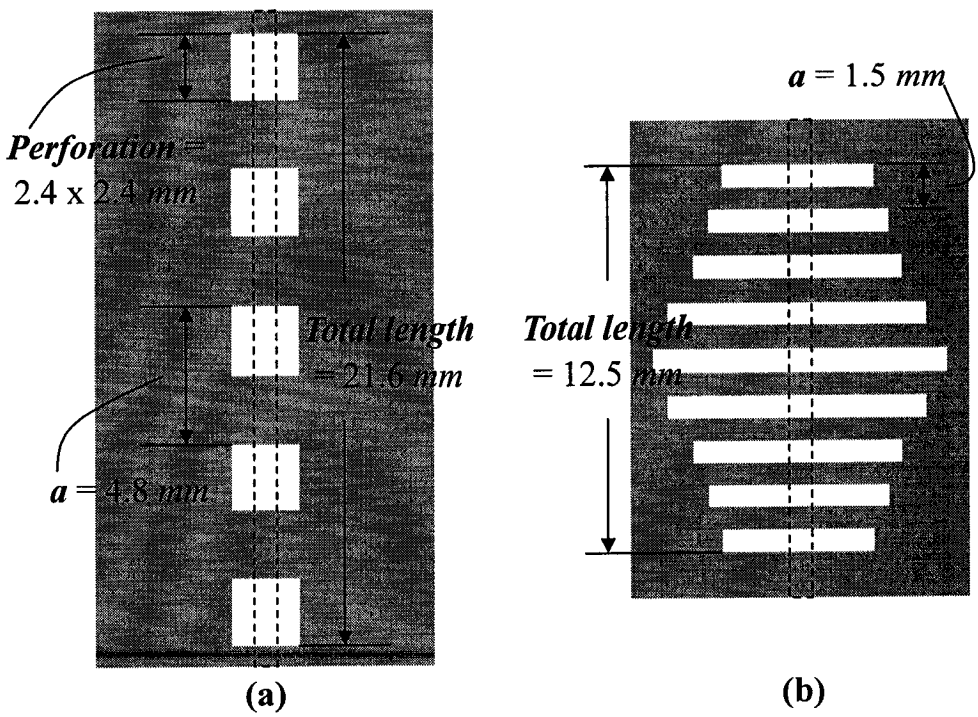

Fig. 3-28: Layout schematics of (a) the conventional EBG and (b) the non-linearly TA patterned EBG structures.

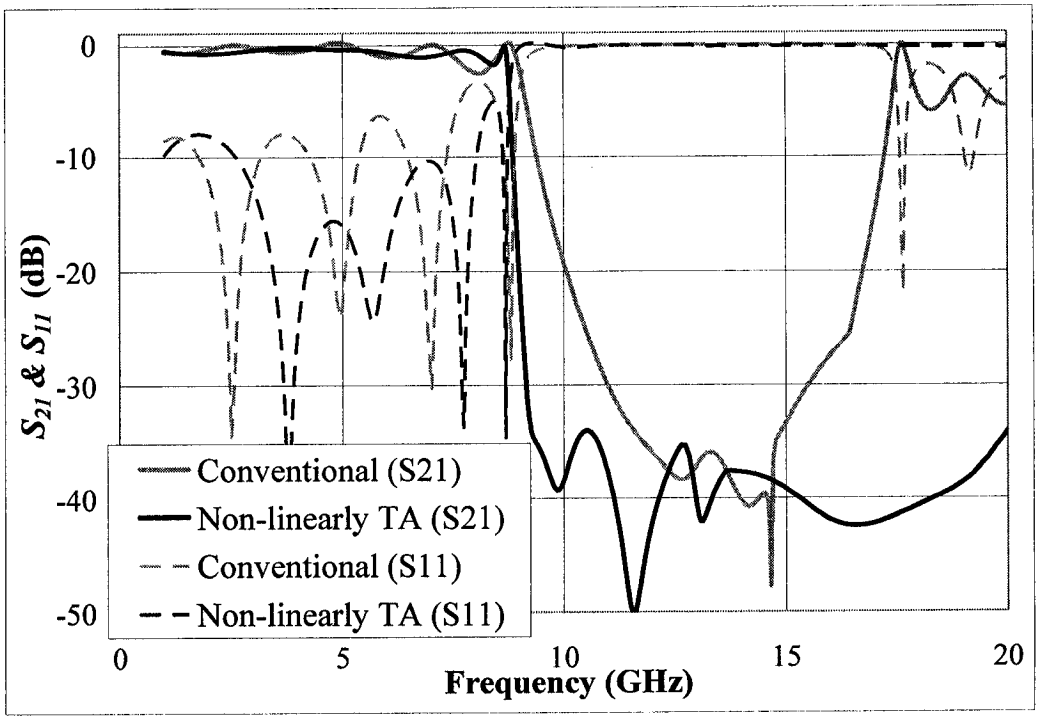

Fig. 3-29: Comparisons of S_{11} and S_{21} between the conventional EBG and the non-linearly TA patterned EBG structures.

It is observed from Fig. 3-29 that the performances of both structures are similar with a cutoff frequency at around 9 *GHz*. However, the conventional EBG structure shows a smaller stopband region and a poorer return loss (S_{11}) performance in the passband region. Meanwhile, the conventional structure has a higher insertion loss (S_{21}) in the passband region. Therefore, the non-linearly TA patterned EBG structure not only has a significantly reduced dimension (57% of the conventional structure in length) but also has superior passband and stopband regions. In the next section, the performance of the non-linearly TA patterned EBG structure is verified with experimental results.

3.2.2.2. *EXPERIMENTAL MEASUREMENTS AND COMPARISONS*

The Anritsu vector network analyzer (VNA) was used to carry out the S-parameters measurements of the non-linearly TA patterned EBG sample. The universal test fixture was utilized to hold the sample in place and the setup was connected to the VNA via microwave cables. Thus, the EBG structure was being measured as a two-port network where S_{21} and S_{11} were used to characterize its performance. Fig. 3-30 illustrates the front (microstrip line) and the back sides (non-linearly TA pattern) of the fabricated sample and its dimensions.

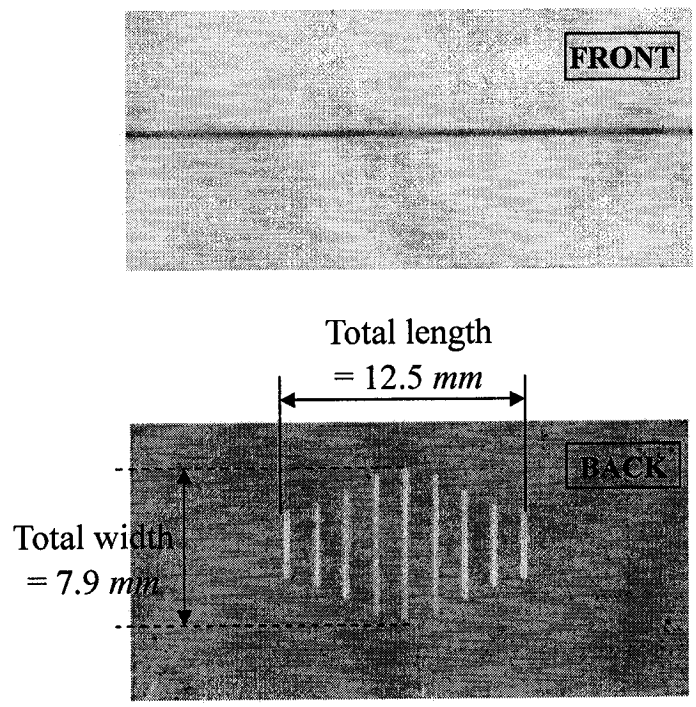

Fig. 3-30: A photo of 9-slot non-linearly TA patterned EBG structure fabricated for measurements.

Fig. 3-31 shows the simulated and measured results on the 9-slot non-linearly TA patterned EBG structure.

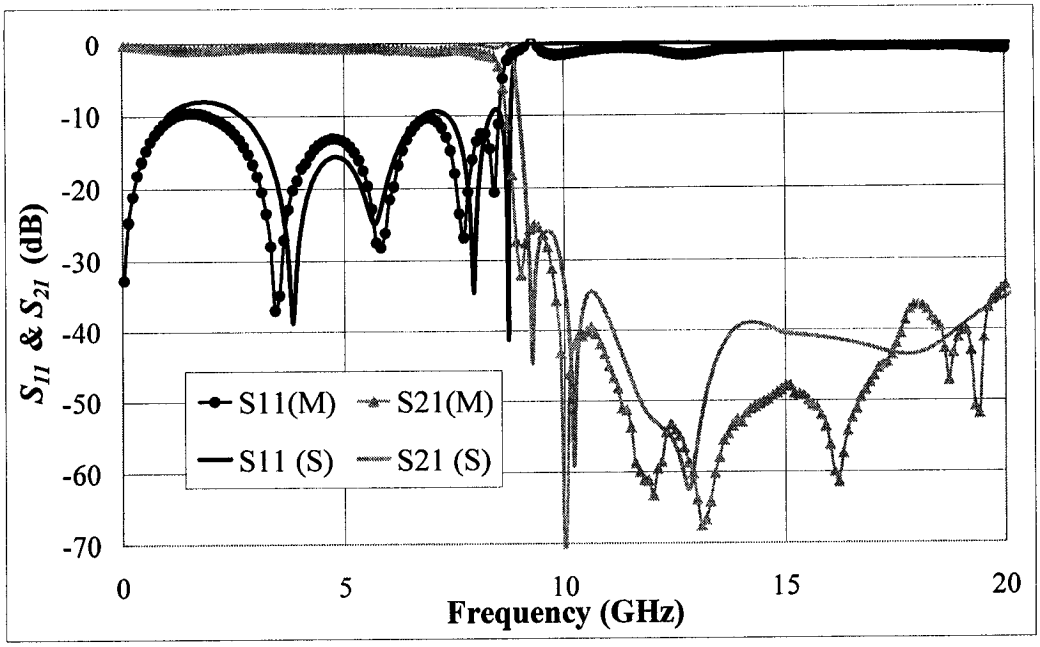

Fig. 3-31: S-parameter results of simulated (S) and measured (M) 9-slot TA patterned EBG structure.

It is observed from Fig. 3-31 that the simulated and measured results match very well. Therefore, the concept of constructing a non-linearly TA patterned EBG structure is verified.

3.2.3. SUMMARY

In this section, an EBG structure with a special type of pattern called Tapered Array (TA) was explored and investigated. The distinct characteristic of tapered array pattern is the gradual increase of the slot perforation length to a maximum then decrease back to the original dimension with a certain structure period. It is considered to be a planar pattern that can be implemented in the ground plane of a microstrip transmission line very easily.

It was found that the structure period (a) affects the quality of the passband

insertion loss and the stopband attenuation. The insertion loss decreases and the attenuation increases as a is increased. The number of slots (n) and the slot lengths are also very important for constructing a continuous and wide stopband region. Meanwhile, the most important dimension in the TA-patterned EBG structure is the center slot length (L), which is strongly correlated to the 3 dB cutoff frequency. The cutoff frequency increases as L is decreased. Therefore, this finding allows designers to control the passband and stopband regions very easily.

The non-linearly tapered array pattern further enhanced the performance of the EBG structure as a microwave lowpass filter significantly. In addition, the design and implementation are both simple and compatible with microwave planar technology. When compared to the conventional EBG structure with periodically spaced rectangular perforations, the proposed TA patterned EBG structure has a better performance and a smaller structural size. Therefore, the non-linear structure can easily be utilized and applied in microwave components that require a lowpass filter.

4. DESIGN OF INTER-COUPLED SPLIT-RING RESONATOR STRUCTURES

Bandpass filters are one of the most common and yet essential building blocks in today's communication system. Many microwave components and devices depend on filters to achieve the frequency-selective or harmonic-suppression applications [4-1, 4-2, 4-3]. Conventionally, the bandpass filters are constructed with parallel-coupled microstrip lines, which utilize half-wavelength line resonators [4-4, 4-5]. However, recent development in commercial communication systems makes broad bandwidth transmission at higher frequencies desirable. Therefore, the drawback of narrow bandwidth of parallel-coupled filters has to be addressed. The structures with improved fractional bandwidth have been proposed but these structures utilize short circuit stub as inductors and shunt metal pads as capacitors, which require via and increase the overall device area [4-6, 4-7].

In this chapter, inter-coupled split-ring resonator (SRR) structure (Fig. 4-1) is proposed and implemented directly on the microstrip line to realize a bandpass filter (BPF) at microwave frequencies. The characteristics of the proposed structure such as the passband frequency and the bandwidth are explored so the filter can be controlled and designed to have practical applications. The proposed structure not only exhibits a special property of having a wide passband width but also it is very simple to design

and implement. Therefore, the proposed structure can be a suitable candidate for microwave filters employed in microstrip planar technology.

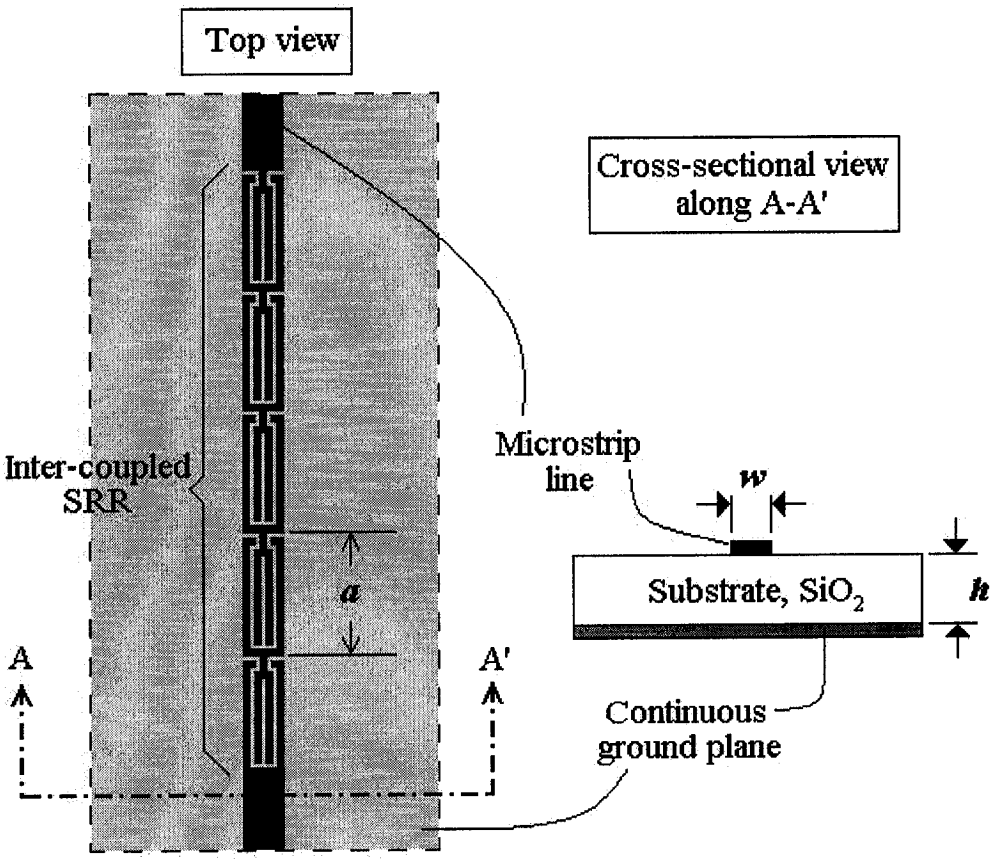

Fig. 4-1: An inter-coupled SRR structure implemented on microstrip line to realize a BPF with a large FBW.

4.1. DESIGN METHODOLOGY: UNIFORM SRR STRUCTURES

The standard procedure to design a microstrip-based filter is to first select a lowpass prototype network with normalized element values. Then, by performing frequency and element transformation, the lowpass prototype can be realized with lumped network, which has the desired frequency band performance. A lowpass prototype with a ladder network structure is shown in Fig. 4-2.

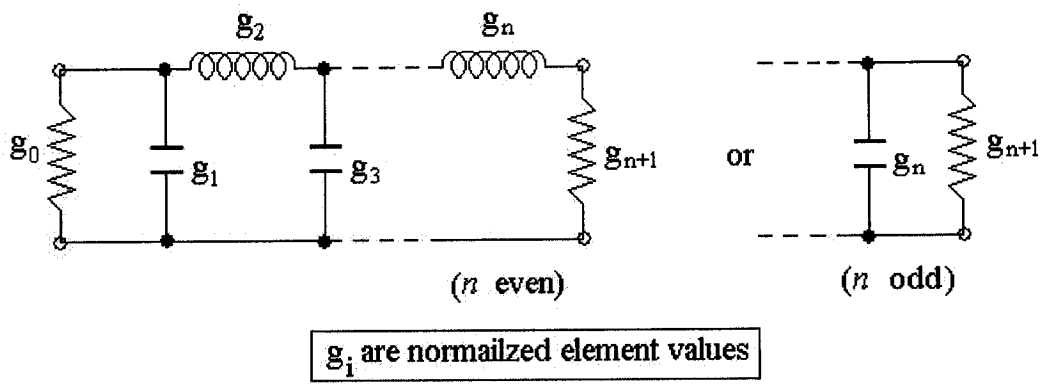

Fig. 4-2: A generalized lowpass prototype with a ladder network structure.

In order to implement the filter circuit and realize it with practical microwave structures, the impedance inverters (*K*-inverters) were utilized. Fig. 4-3 illustrates the equivalent circuit of a shunt capacitor and a bandpass filter expressed in terms of *K*-inverters.

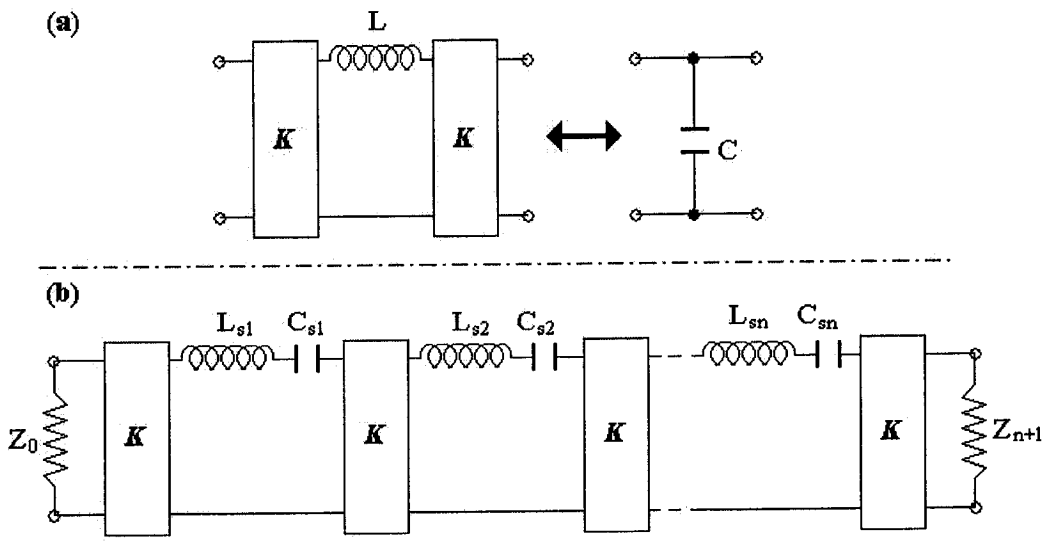

Fig. 4-3: Equivalent form of (a) a shunt capacitance and (b) the bandpss prototype with the utilization of *K*-inverters [4-8].

The *K*-inverter is a two-port network that has a phase shift of 90 degrees and it can be realized with a quarter-wavelength microstrip transmission line [4-8]. Thus, one way to comprehend this in practical microwave filter design is to utilize the

proposed inter-coupled split-ring resonator structure. The *K*-inverter could be represented by the split-ring structure, which its length is chosen to be a quarter of the guided wavelength at the frequency of transmission. Then, the series inductor and capacitor shown in Fig. 4-3 are represented by the cascaded metal rings and the space between each resonator respectively.

The proposed bandpass filter is consisted of half-wavelength resonators that are inter-coupled together to form cascaded split-ring structures. Therefore, the input and the output ports can be aligned, which is an advantage when compared to the conventional parallel-coupled microstrip filters where there is an offset between the ports. Fig. 4-4 shows a single half-wavelength resonator and its equivalent circuit. The half-wavelength resonator is represented by the black region shown in Fig. 4-4(a). The dashed line regions are part of the adjacent resonators also shown to illustrate how the split-rings are formed. Fig. 4-4(b) illustrates the corresponding series inductance (contributed by the half-wavelength resonator shown in black) and series capacitance (contributed by the spacing between the split-rings) that are induced by this configuration. The spacings between the split-rings are exaggerated in Fig. 4-4(b) to reveal how each component is contributed by the physical implementation.

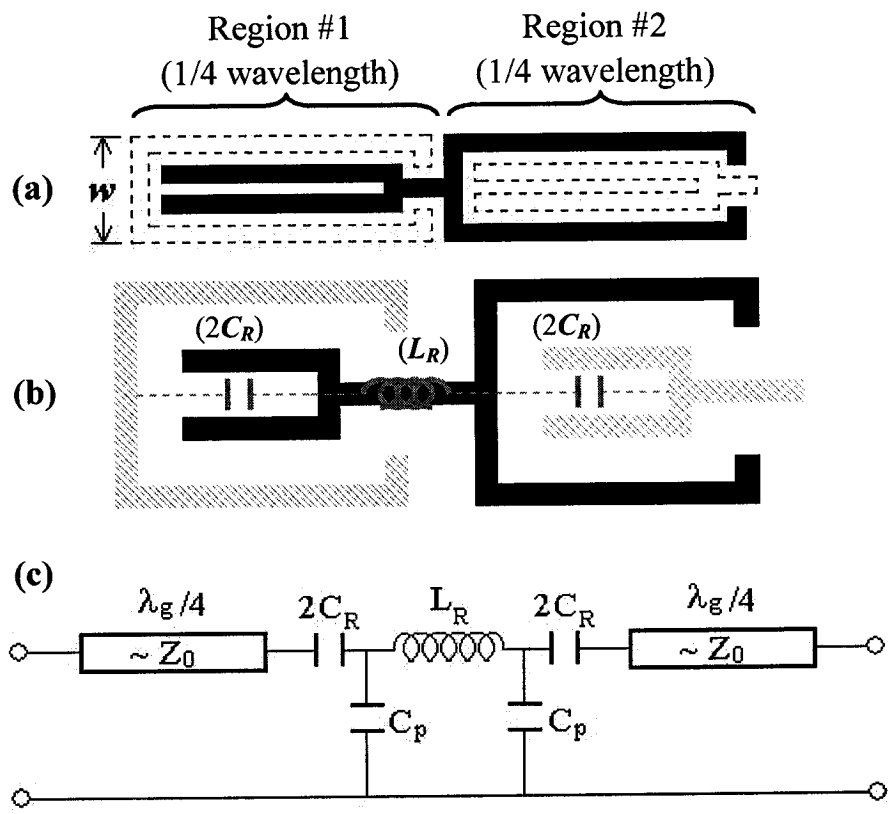

Fig. 4-4: (a) A half-wavelength resonator (black region) showing (b) induced capacitance and inductance and (c) its equivalent circuit.

L_R and C_R are the series inductance and capacitance of the half-wavelength resonator. C_ps are the parasitic capacitances to the ground. Two approximations were made for the following analysis. First, since the width of the split-ring structure is relatively small, the effect of the parasitic is small and hence C_ps are neglected. Second, even though region #1 and #2 shown in Fig. 4-4 are non-symmetrical, the induced capacitances (C_R) in both regions are assumed to be the same since the coupling regions of the split-ring resonators are approximately the same. If w of the resonator shown in Fig. 4-4 is selected to be the same as the microstrip line width, then the characteristic impedance of the line will remain near 50 Ω. Therefore, the

bandpass filter network shown in Fig. 4-3 can be approximated with the inter-coupled split-ring resonators and the values of L_s and C_s can be calculated with the basic element transformation equations given by

$$L_R \approx L_s = \frac{Z_0}{X \cdot \omega_0} g_i \; ; \quad C_R \approx C_s = \frac{1}{\omega_0^2 L_s} \tag{4-1}$$

The fractional bandwidth (X) of the bandpass filter is given by

$$X = \frac{\omega_2 - \omega_1}{\omega_0} ; \quad \omega_0 = \sqrt{\omega_1 \omega_2} \tag{4-2}$$

where ω_1 and ω_2 indicate the passband-edge angular frequencies and Z_0 is the characteristic impedance of 50 Ω.

First of all, the proposed structures that have uniform and periodic split-ring resonators are considered. Thus, the element values of g_i for every unit cell are forced to be the same (denoted by g) for every resonator since they are periodically identical. From Eq. 4-1, L_R and C_R can be expressed in terms of g and therefore, one set of solution can be found to satisfy the desired fractional bandwidth (X) and the center frequency (ω_0). To demonstrate the design methodology, bandpass filters were analyzed according to the parameters shown in TABLE 4-I, in the attempt to reveal the characteristics of the proposed inter-coupled split-ring resonator structure.

TABLE 4-I: PHYSICAL AND DESIGN PARAMETERS

Physical Parameters	Substrate	Corning 1059 (SiO_2)
	Dielectric constant (ε_r)	3.9
	Substrate thickness (h)	0.37 *mm*
	Microstrip line width (w)	0.80 *mm*
Design Parameters	Arithmetic Mean Center frequency (f_c)	14 *GHz*
	Geometric Mean Center frequency (f_0)	13 ~ 14 *GHz*
	Fractional Bandwidth (X)	30 ~ 80%
	Number of SRR cells	5

The physical parameters are chosen so the microstrip transmission line structure has a characteristic impedance of 50 Ω. The target center passband frequency is set at 14 *GHz* and five of the cascaded split-ring resonators are considered here. Meanwhile, it is also desirable to have the control of the fractional bandwidth of the filter so the target is set from 30% to 80%. Since ω_0 $(=\sqrt{\omega_1 \cdot \omega_2} = 2\pi f_0)$ is calculated as a geometric mean value, it varies as the fractional bandwidth is increased. Therefore, a fixed arithmetic mean center frequency ω_c $(=(\omega_1 + \omega_2)/2 = 2\pi f_c)$ is used as an indicator to design the bandpass filters. The inductance and the capacitance from Eq. 4-1 have to be calculated before the implementation of the inter-coupled split-ring resonators. Therefore, an element value, g, can be found for every pair of X and w_0 with the equivalent circuit modeling simulated by Agilent Advanced Design System. TABLE 4-II shows the corresponding inductance, capacitance, and the element values of the bandpass filters obtained from calculations and circuit simulations.

TABLE 4-II: DESIGN PARAMETERS FOUND BY CALCULATIONS AND CIRCUIT MODELING

Target f_c (*GHz*)	Target X (%)	L_s (*nH*)	C_s (*pF*)	g	Resulting f_0 (*GHz*)	Resulting X (%)
14.0	30	2.56	0.05	1.35	14.0	28.7
	40	1.63	0.08	1.13	13.8	40.5
	50	1.22	0.11	1.04	13.6	50.7
	60	0.92	0.15	0.93	13.4	61.8
	70	0.71	0.21	0.89	13.1	71.9
	80	0.64	0.23	0.84	13.0	79.5

Fig. 4-5 shows the simulated results of S_{21} from the circuit modeling. It can be seen that the fractional bandwidth is varied for a significant range while the arithmetic mean of the center frequency stays at 14 *GHz*. Also noted from the figure that as the fractional bandwidth decreases from 80% to 30%, the insertion loss (ripples in the passband) is increased from 0.5 *dB* to 1.5 *dB*. However, as the fractional bandwidth decreases, the quality of high frequency stopband is improved. The attenuation at around 22.5 GHz improves from 18.9 *dB* to 53.8 *dB*. Fig. 4-6 illustrates the corresponding S_{11} of the circuit simulations.

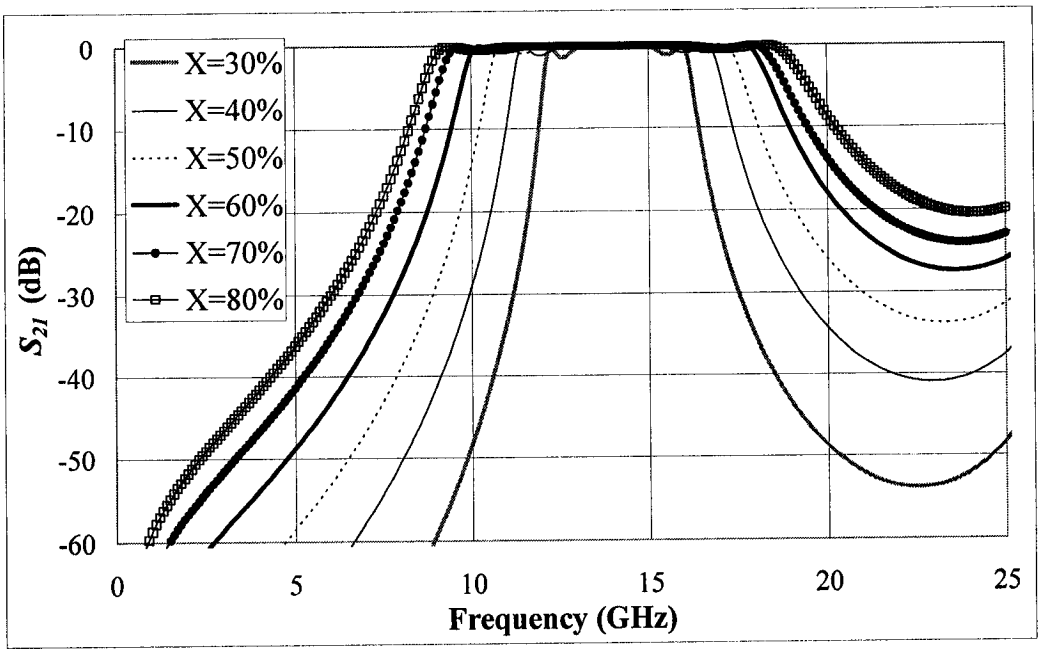

Fig. 4-5: S_{21} of the circuit simulations showing the variation of the fractional bandwidth.

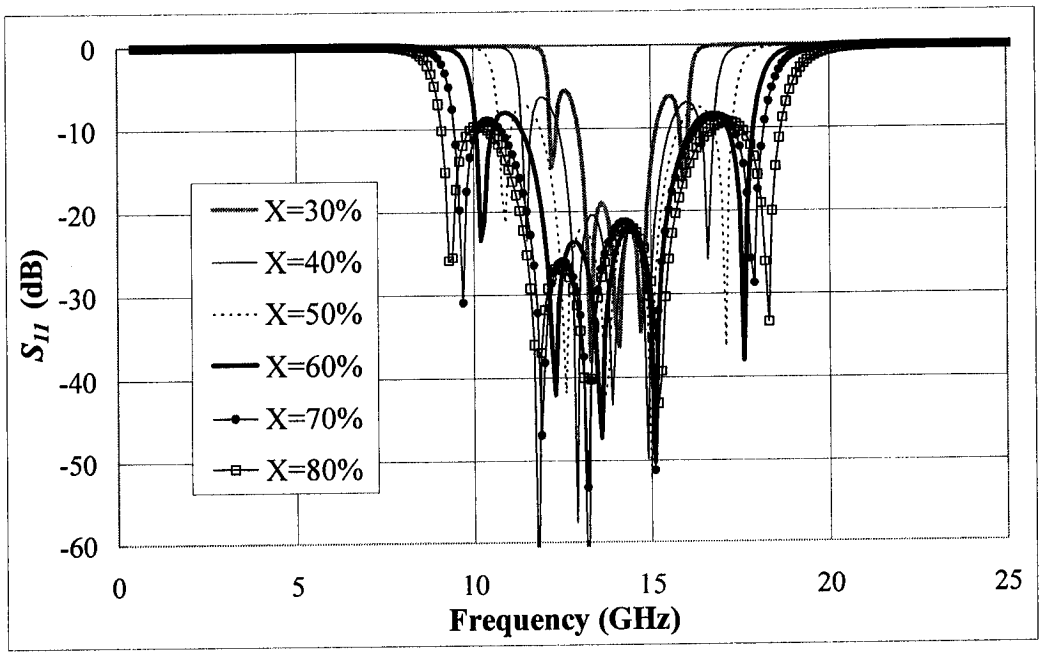

Fig. 4-6: S_{11} of the circuit simulations showing the variation of the fractional bandwidth.

The number of uniform and periodic inter-coupled split-ring resonators utilized is five for the previous simulations.

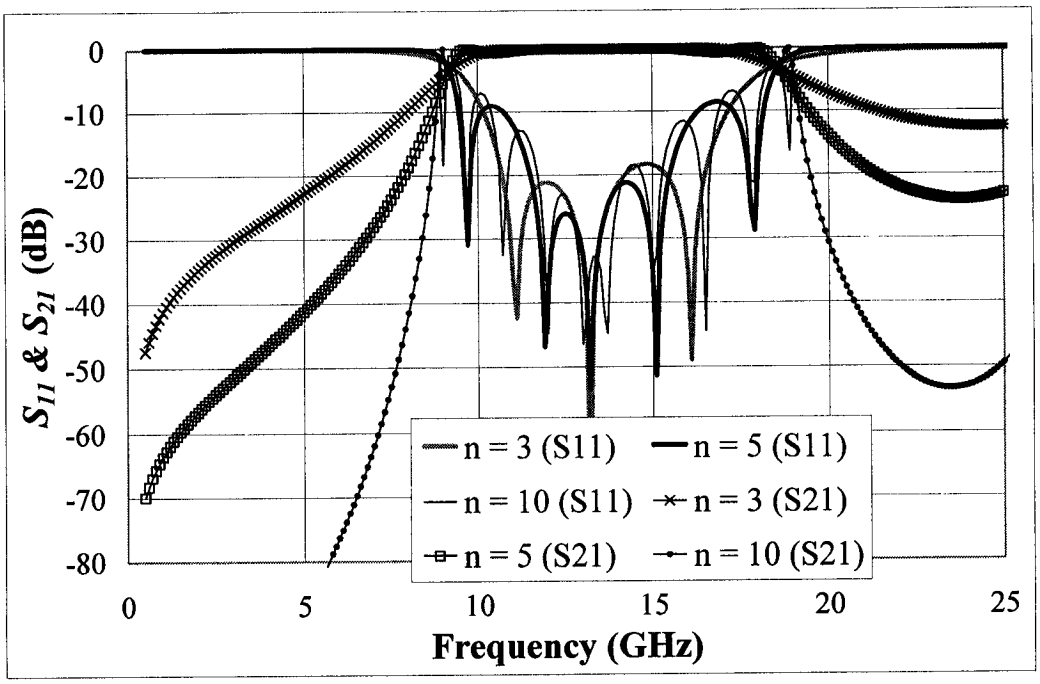

Fig. 4-7: Comparisons of simulated S_{11}/S_{21} for the structures with 3, 5, and 10 inter-coupled split-ring resonator cells.

Fig. 4-7 shows the simulated S_{11} and S_{21} for the structures that have a fractional bandwidth of 70% but with a different number of resonators. Just like the conventional parallel-coupled microstrip filter, as the number of resonator unit increases, the filter's selectivity is improved. Therefore, a higher number of resonator units are required to produce a more defined passband.

Up to this point, the values of capacitance and inductance were calculated and the desired filter responses were confirmed by the circuit simulation. Therefore, the next step is to implement the inter-coupled split-ring resonator physically in the layout designs.

4.2. PHYSICAL IMPLEMENTATION OF SRR STRUCTURES

Since strong couplings are desirable, every half-wavelength resonators are inter-coupled with adjacent resonators to form split-ring structures along half of their length. Therefore, the quarter-wavelength coupling length (or the structure period, a) that consisted of the split-ring resonator determines the arithmetic mean of the center frequency (f_c) of the passband region.

$$a = \frac{\lambda_g}{4}; \quad \lambda_g = \frac{c}{f_c \sqrt{\varepsilon_{eff}}} \tag{4-3}$$

where λ_g is the guided wavelength, c is the speed of light, and ε_{eff} is the effective permittivity of the medium. Thus, the first design requirement is to select a, which can be calculated from Eq. 4-3 and it is equal to 3.1 *mm* for f_c of 14 *GHz*. Fig. 4-8 illustrates the dimensions used to characterize an inter-coupled split-ring resonator structure. Evidently, the capacitance is controlled by the ring spacing (s) and the inductance is controlled by the ring width (w_r). The structure period (a) has a combined effect on both the capacitance and the inductance.

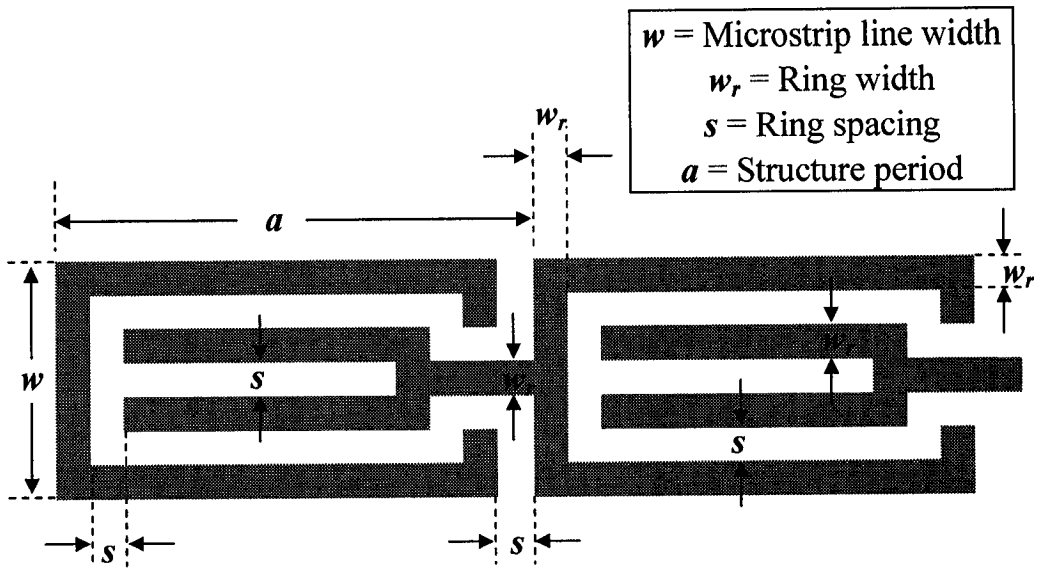

Fig. 4-8: Dimensions of the inter-coupled split-ring resonator structure.

The substrate used to construct the inter-coupled split-ring resonator structure is Corning 1059, which has a dielectric constant of 3.9. Its dimension and microstrip width were described in TABLE 4-I, which provide a characteristic impedance of 50 Ω. In order to maintain the compatibility, it is desirable to keep this characteristic impedance undisturbed. Therefore, the second requirement to design the inter-coupled split-ring resonator is to let w equals 0.8 *mm*. With these conditions, the ring spacing (s) and width (w_r) were varied to match to the values derived from the circuit simulations (TABLE 4-II) in order to construct bandpass filters with desired fractional bandwidths. TABLE 4-III shows the physical parameters used to build the inter-coupled split-ring resonators that can be utilized as microwave bandpass filters with controllable fractional bandwidth. The resulting passband center frequency and the fractional bandwidth are also shown.

TABLE 4-III: PHYSICAL PARAMETERS USED IN LAYOUT SIMULATIONS

Microstrip Width (w)	Structure Period (a)	Target X (%)	Ring Spacing s (μm)	Ring Width w_r (μm)	Resulting f_0 (GHz)	Resulting X (%)
0.8 mm	3.1 mm for f_c = 14 GHz	30	224.0	32.0	14.0	29.1
		40	160.0	80.0	13.8	40.1
		50	106.0	120.5	13.6	50.9
		60	64.0	152.0	13.4	60.6
		70	32.0	176.0	13.2	71.7
		80	10.0	192.5	13.0	80.0

From TABLE 4-III, it can be seen clearly that the physical limitations of the proposed filter are the ring spacing (s) and width (w_r). The inter-coupled split-ring resonator structure becomes harder to construct as these two values reach below micro-meters. Nevertheless, the proposed structure is demonstrated to have a flexible range of fractional bandwidth that can be controlled easily by adjusting the ring spacing and width. Meanwhile, the arithmetic mean center frequency of the bandpass filter can be designed by choosing the desired structure period (a), which can be calculated with Eq. 4-3. Fig. 4-9 shows the S_{21} of the simulated layout designs according to the physical values given by TABLE 4-III to demonstrate the variation of the fractional bandwidth from 30% to 80%. The corresponding S_{11} are shown in Fig. 4-10.

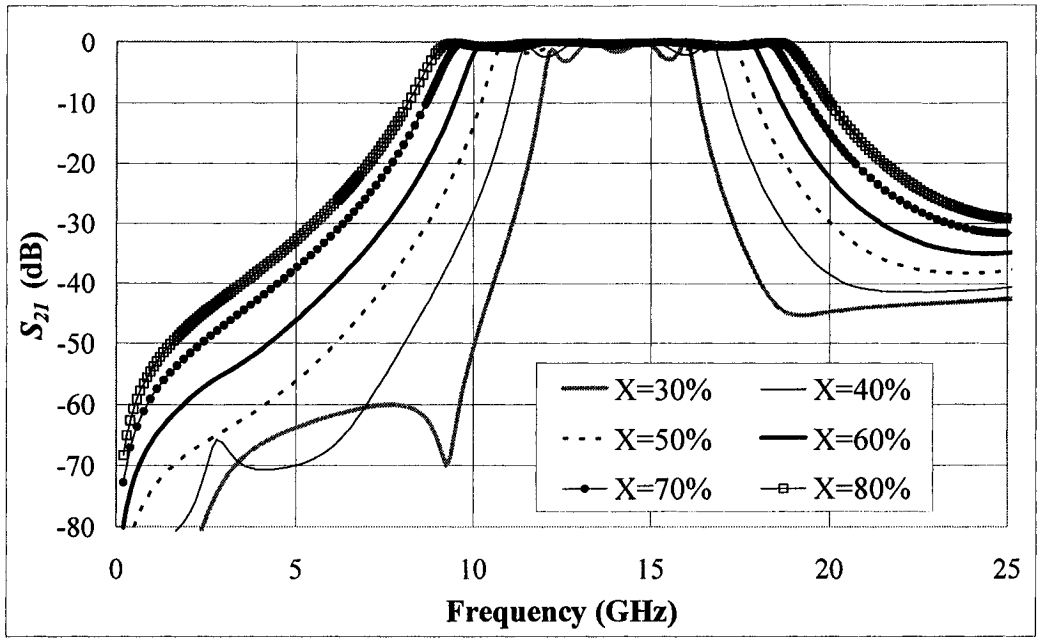

Fig. 4-9: S_{21} of the simulated layout designs for the inter-coupled split-ring resonator structures with variation of the fractional bandwidth from 30% to 80%.

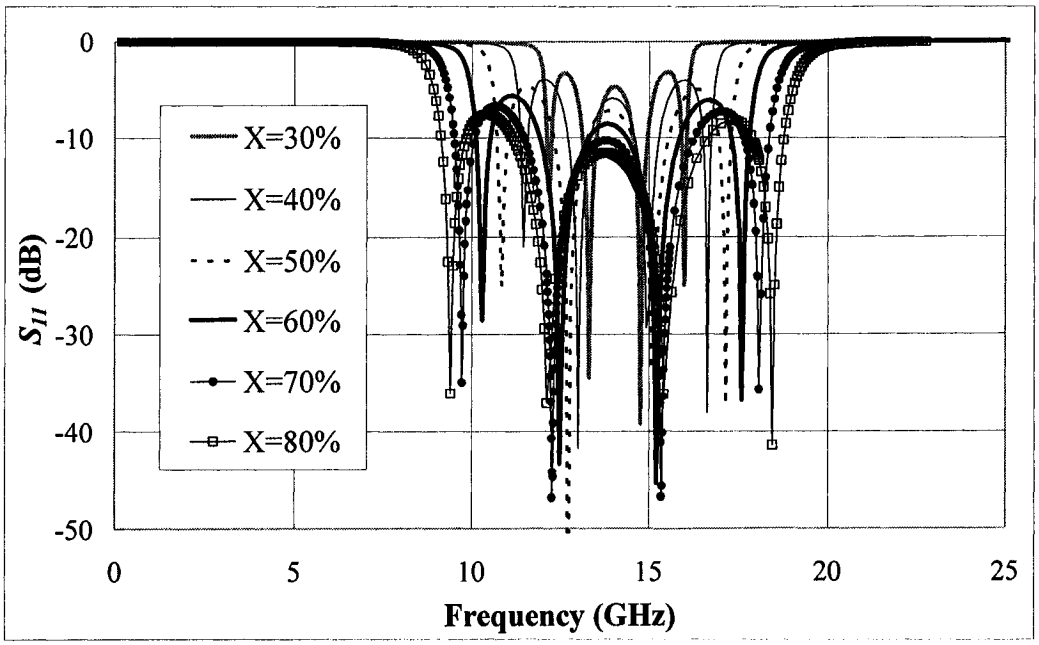

Fig. 4-10: S_{11} of the simulated layout designs.

It is observed that the insertion loss (S_{21}) in the passbands increases from 0.9 *dB* to 3.2 *dB* as the fractional bandwidth is decreased from 80% to 30%. This indicates that the

passband's quality degrades as the fractional bandwidth is decreased. This degradation can also be seen from the S_{11} response in Fig. 4-10. Nevertheless, the maximum attenuations of the upper and lower stopbands were all better than 25 *dB* shown in Fig. 4-9. Also, the arithmetic means of center passband frequencies remain at 14 *GHz*, which is consistent with the circuit simulations. For the purpose of comparison, Fig. 4-11 illustrates the S_{21} obtained from the circuit (dashed-grey) and layout (solid-black) simulations. It can be seen that the circuit and layout simulations matched fairly well.

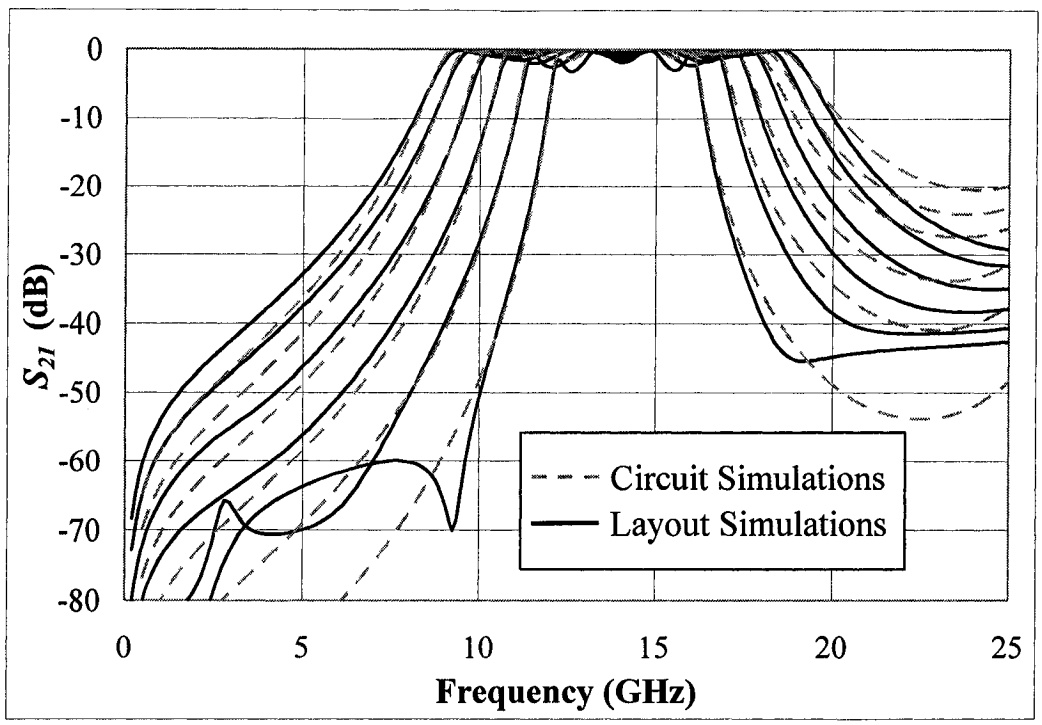

Fig. 4-11: Comparisons of S_{21} between the circuit and layout simulations.

To demonstrate the control of the center passband frequency (f_c), three structures with different structure period (a = 4.3 *mm*, 3.6 *mm*, and 3.1 *mm*) were simulated. All other dimensions including the microstrip width (w), ring spacing (s), and ring width (w_r) were kept constant. The resulting S_{21} responses are shown in Fig. 4-12.

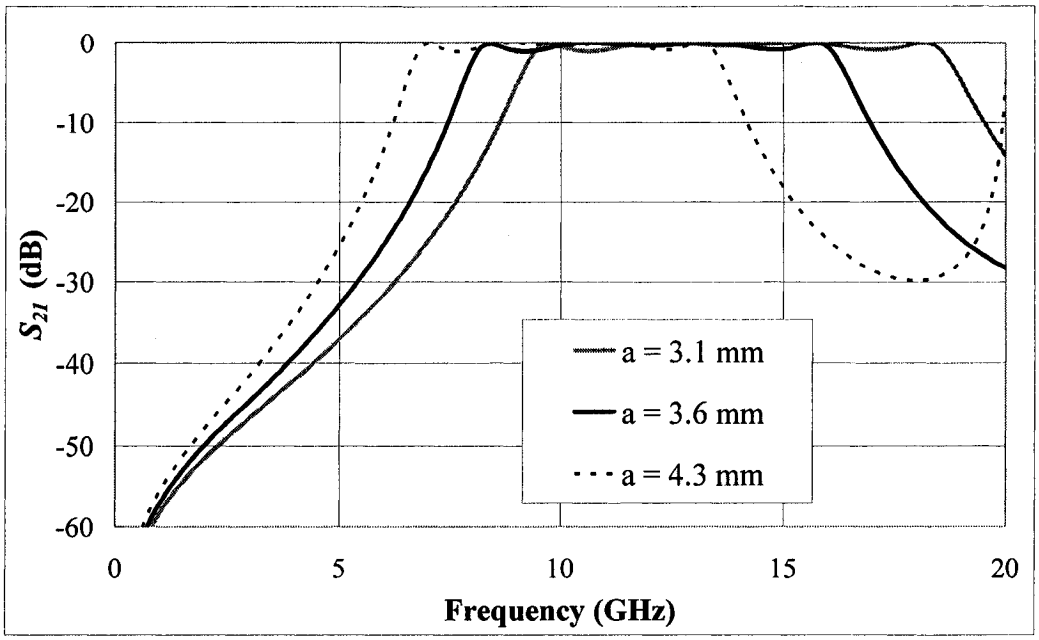

Fig. 4-12: S_{21} of the inter-coupled split-ring resonator structures with a = 4.3 *mm*, 3.6 *mm*, and 3.1 *mm*.

It can be observed that the corresponding center passband frequency (f_c) is located at 10.1 *GHz*, 12.1 *GHz*, and 14.0 *GHz* for structures with a = 4.3 *mm*, 3.6 *mm*, and 3.1 *m*m respectively. Also, the fractional bandwidth remains unchanged at 73% for all three cases. The maximum insertion losses in the passbands were around 1.1 *dB* while the attenuations of the stopbands were all better than 30 *dB*. Therefore, the proposed structures that have uniform inter-coupled split-ring resonators can be designed to have a particular center frequency and fractional bandwidth without difficulty. Moreover, the proposed structure exhibit a wider than normal fractional bandwidth characteristic with low insertion loss.

The inter-coupled split-ring resonator structure that has five unit cells with a equals to 3.1 *mm* (f_c = 14 *GHz*) and a ring spacing of 30 μm was experimentally

fabricated and the S-parameters were measured with Anritsu 37347A Vector Network Analyzer to compare against the simulated ones. Fig. 4-13 illustrates the fabricated sample with four half-wavelength resonators cascaded together to form five periodically inter-coupled split-rings implemented on the microstrip line. The overall device length is 15.5 *mm*. Fig. 4-14 shows the comparison between the simulated and measured S-parameters.

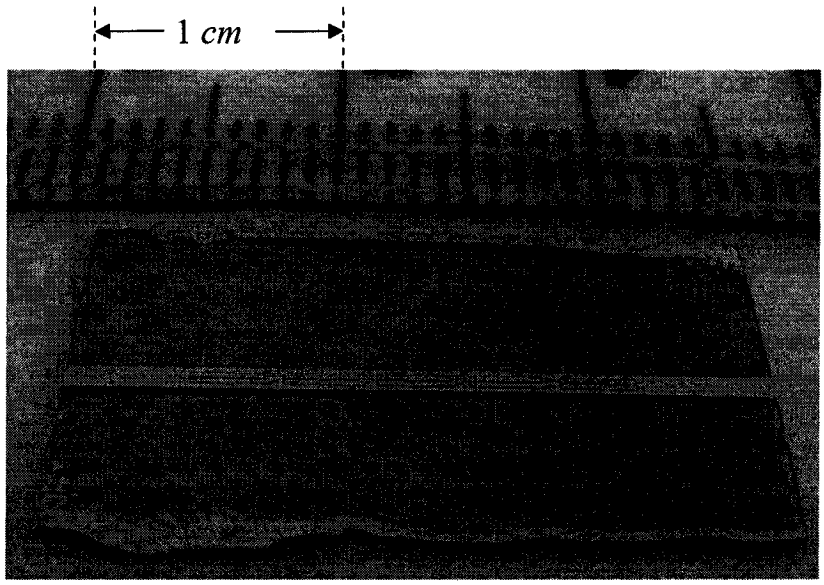

Fig. 4-13: A photo of fabricated sample with a = 3.1 *mm* and s = 30 μm for measurements.

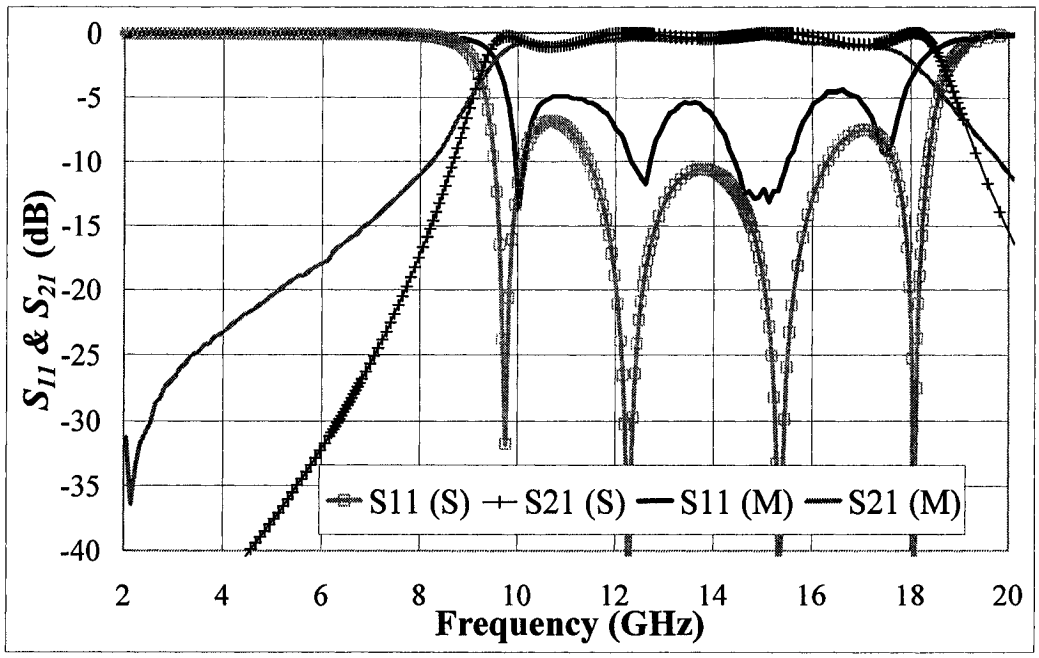

Fig. 4-14: Comparison between the simulated (S) and measured (M) S-parameters for the case with **a** = 3.1 *mm* and $s = 30\ \mu m$.

It is observed from Fig. 4-14 that the f_c of the measured sample is located at 13.8 *GHz*, which is very close to the simulation result. In addition, the measured sample exhibits a passband region from 9.33 *GHz* to 18.21 *GHz*, which corresponds to a fractional bandwidth of 68.2%. The maximum passband insertion loss is 0.81 *dB* for the measured sample. Therefore, this experiment confirms the feasibility of utilizing the inter-coupled split-ring resonator structure for microwave bandpass filter applications. One possible explanation for the discrepancy between the measured and simulated S_{21} at low frequency end is due to the calibration of the test fixture. Due to the limitation of the physical size of the fabricated sample, there was not much room at both ends of the microstrip line, which are needed for the calibration purpose. Nevertheless, the viability of the structure is demonstrated.

4.3. NON-UNIFORM SRR STRUCTURES

Depending on the application of the filter, whether a maximally-flat response or a steeper roll-off edge is desirable, various transfer functions such as Butterworth, Chebyshev or elliptic responses used for lowpass prototype filters can be considered. In this section, the inter-coupled split-ring resonator structures were simulated according to the element values of 3-pole and 5-pole Chebychev prototypes with a fractional bandwidth (X) of 30% centered at 14 *GHz* to demonstrate the enhanced filter performances. TABLE 4-IV summarizes the design parameters used to realize the modified resonator structure.

TABLE 4-IV: SIMULATION AND DESIGN PARAMETERS FOR NON-UNIFORM SRR STRUCTURES

Target f_c (*GHz*)			14			
Target X			30%			
a (*mm*)			3.10			
Functions	Elements	g_i	L_s (*nH*)	C_s (*pF*)	s (*mm*)	w_r (*mm*)
Chebychev 3-pole	$n = 1, 3$	1.032	1.95	0.066	0.100	0.125
	$n = 2$	1.147	2.17	0.059	0.200	0.125
Chebychev 5-pole	$n = 1, 5$	1.147	2.17	0.059	0.080	0.140
	$n = 2, 4$	1.371	2.60	0.050	0.160	0.140
	$n = 3$	1.975	3.74	0.035	0.240	0.140

Fig. 4-15 illustrates the topology of the microstrip line containing the inter-coupled split-ring resonators, which has non-periodic cells with the ring spacings (s) and ring widths (w_r) that correspond to the coefficients of the 3-pole Chebychev prototype. A 3-pole filter in the inter-coupled split-ring resonator design would have

three independent branches (n = 1 ~ 3) as shown in Fig. 4-15 and thus, there are four split-ring resonator cells. Therefore, a 5-pole filter would have five independent branches, which would form six split-ring resonator cells.

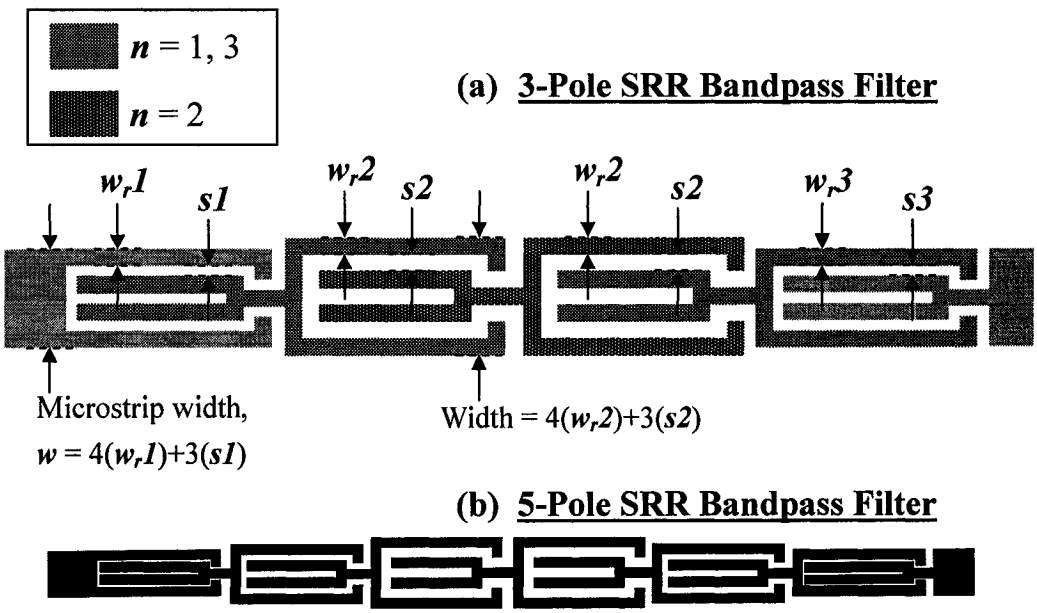

Fig. 4-15: (a) Layout of the modified inter-coupled split-ring resonators according to the element values of the 3-pole Chebychev prototype. (b) Schematic for the 5-pole filter.

Fig. 4-16 shows the S-parameters obtained from the layout simulations of the inter-coupled split-ring resonator structures that utilize Chebychev 3-pole and 5-pole filter responses.

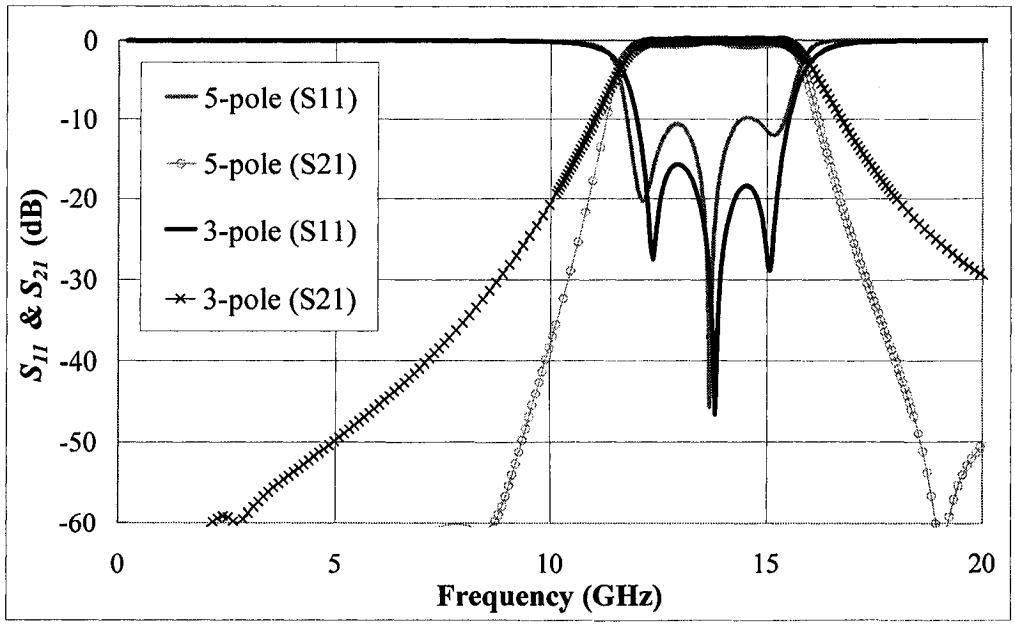

Fig. 4-16: S_{11} and S_{21} of the layout simulations of the inter-coupled split-ring resonator structures based on 3-pole and 5-pole Chebychev coefficients.

Both structures have a fractional bandwidth of 30.8% centered at around 14 *GHz*. It is observed that the 5-pole configuration has a sharper roll-off at the passband edges. However, the maximum insertion loss in the passbands is only 0.15 *dB* for the 3-pole configuration (0.5 *dB* for the 5-pole). By utilizing a transfer function, the filter's performance is greatly enhanced. Fig. 4-17 shows a comparison between the uniformly-sized (four SRR unit cells) and the Chebychev 3-pole inter-coupled split-ring resonator structures. Both structures have a fractional bandwidth of 30% centered at 14 *GHz*.

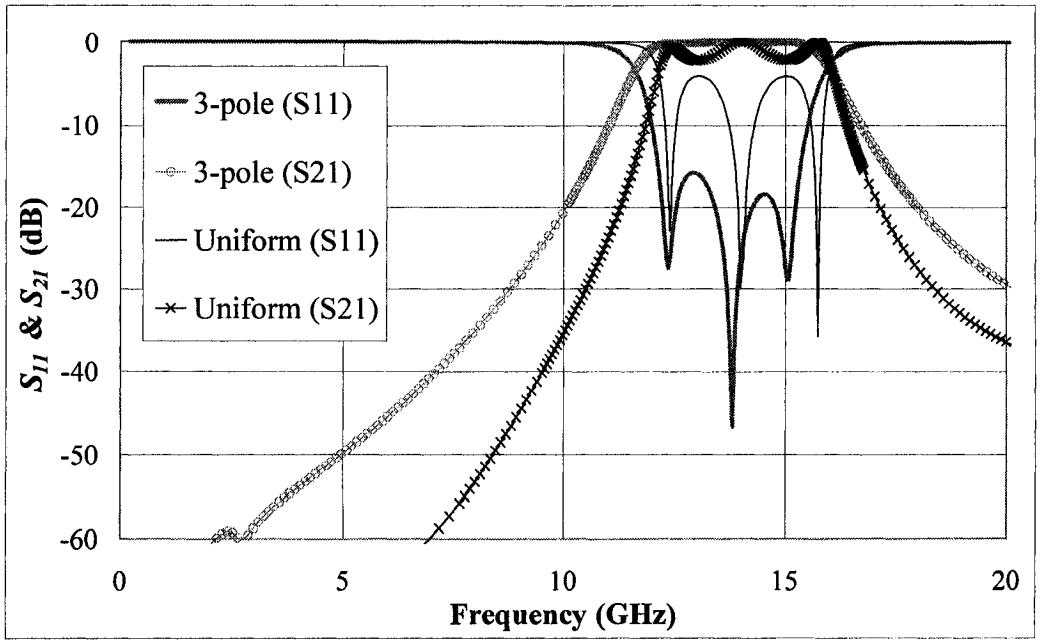

Fig. 4-17: Comparison between the uniform SRR and Chebychev 3-pole SRR configurations.

It can be observed that the filter with Chebychev 3-pole configuration has superior performances on both the insertion loss (S_{21}) and the return loss (S_{11}) in the passband. The maximum insertion loss is 0.17 *dB* for the filter with Chebychev 3-pole configuration and 2.3 *dB* for uniformly-sized configuration. Therefore, the inter-coupled split-ring resonator structures can also be configured with typical transfer functions to enhance the filter performance.

4.4. SUMMARY

A novel inter-coupled split-ring resonator structure has been designed and analyzed in this chapter. Together with the microstrip transmission line, the proposed structure has unique characteristics such as a wide passband region with low insertion loss and a high attenuation in stopband regions. Thus, it can be utilized in applications

such as microwave bandpass filter. Unlike the traditional parallel-coupled structures, the inter-coupled split-ring resonators occupy less space in the lateral direction and they are compatible with microwave planar technology. It has been demonstrated in both simulations and experiments that the proposed structure can exhibit a fractional bandwidth of over 68% with a simple uniformly-sized configuration. The location of the passband frequency and the fractional bandwidth are also relatively straightforward to design. In addition, common filter prototype response can be applied easily to enhance the performances of the structure. Therefore, the inter-coupled split-ring resonator structure incorporated with microstrip line has been successfully demonstrated with promising results for them to be applied as microwave filters.

5. ULTRA-LOW SHEET RESISTANCE CdS DEPOSITION

Cadmium Sulfide (CdS) is a II-VI semiconductor compound used mostly as window layers in solar cell applications [5-1, 5-2, 5-3]. Also, CdS is a very sensitive photoconductor when the appropriate deposition conditions are applied. Many deposition methods are available for CdS thin films such as chemical bath deposition (CBD), vacuum deposition, and sputtering [5-4, 5-5, 5-6]. CdS thin films with different properties were reported depending on the deposition method and conditions such as solution concentration, temperature, deposition time, and annealing techniques [5-7, 5-8, 5-9, 5-10, 5-11, 5-12, 5-13]. It has been reported that CdS thin film deposition by the CBD method yields the best results in terms of photoconductivity and photosensitivity [1-24, 1-25]. The CBD method is also a low-cost and simple way to deposit CdS over a large area. The purpose of this chapter is to explore and propose a set of optimal conditions for depositing CdS thin films with extremely low sheet resistance (~ 300 *Ω/square*). It is possible to utilize such thin films for microwave switching applications [1-26, 1-27].

First, the preparation of the CBD and the formation of CdS are discussed. Then, the measurement setup used to obtain the sheet resistances and the calculations of photoconductivity are described. Three essential conditions, including temperature,

stir rate, and number of depositions were examined and the results are presented.

5.1. PREPARATION OF CBD SOLUTION

In order to form CdS thin films, Cd^{2+} and S^{2-} ions are required in the CBD solution. 0.5 *M* of both cadmium acetate ($CdC_4H_6O_4$) and thiourea (SCN_2H_4) solutions were first prepared with de-ionized (DI) water. The Cd^{2+} ions are released when the cadmium acetate reacts with a complexing agent, triethanolamine (TEA) with a concentration of 7.4 *M*. Ammonia (30 %) was added in the CBD solution to ensure the release of the S^{2-} ions so CdS could be formed. The pH value of the solution is maintained to be around 11. The chemical reaction of the CBD is

$$[Cd(TEA)]^{2+} + SC(NH_2)_2 + 2OH^- \rightarrow CdS + TEA + CO(NH_2)_2 + H_2O \qquad (5\text{-}1)$$

The CBD solution was prepared in a 80 *ml* beaker and the deposition steps are described in TABLE 5-I. The glass substrates were cleaned with hydrochloric acid and rinsed with DI water in ultrasonic bath prior to CdS deposition. Four gold-electrodes were vacuum deposited onto the glass substrates before the CBD deposition so the sheet resistance of the CdS thin film could be measured.

TABLE 5-I: PREPARATION OF CBD SOLUTION AND PROCEDURE OF DEPOSITION

Steps	Actions
1	Add 11.2 *g* of 0.5 *M* cadmium acetate solution into the beaker.
2	Add 2.8 *g* of 99% TEA and stir thoroughly.
3	Add 5 *g* of 30% Ammonia solution and stir thoroughly.
4	Add 2.8 *g* of 0.5 *M* thiourea solution and stir thoroughly.
5	Add 20 *g* of DI water and stir thoroughly for 1 minute.
6	Place the beaker in water bath (55 ~ 95 °C) and set the stir rate (100 ~ 800 rpm), wait for 15 seconds.
7	Immerse the glass substrate into the solution for 30 minutes.
8	Remove the substrate and rinse with DI water for 1 minute.
9	Place the substrate with DI water in ultrasonic bath for 2 minutes
10	Remove the substrate and rinse with DI water for 5 minutes.
11	Repeat from step 1 if multiple numbers of depositions is required.

5.2. MEASUREMENT SETUP AND METHOD

The sheet resistances of CdS thin films were measured with the four-point probe technique. The measurement setup is shown in Fig. 5-1 and the sheet resistance (R_s) can be calculated by obtaining the values for V_1 and V_2.

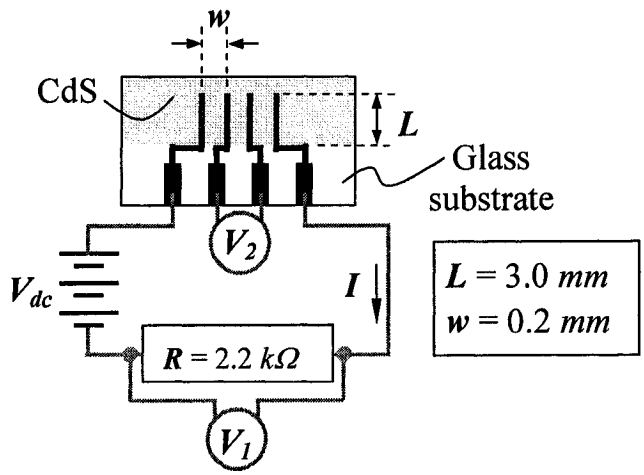

Fig. 5-1: Measurement setup utilized to evaluate the sheet resistances of the CdS thin films.

With the dimensions of the electrodes (L and w) and the value of the resistor known,

the following equation was used to calculate the sheet resistance (R = 2.2 $k\Omega$, L = 3 mm, and w = 0.2 mm).

$$R_s = \frac{V_2}{I} \times \frac{L}{w} = \left(\frac{RL}{w}\right)\frac{V_2}{V_1}; \quad \therefore R_s = 33\left(\frac{V_2}{V_1}\right) \ (k\Omega/square) \tag{5-2}$$

All the CdS thin films were placed in a dark condition for at least 12 hours before measurements. For every sample, the dark R_s is first recorded for one minute and then the samples were exposed to a 532 nm green laser pointer (50 mW/cm^2) for three minutes. Afterwards, the samples were remained in the dark for seven minutes. Fig. 5-2 shows a photo of actual deposited CdS thin film on the glass substrate with four gold electrodes for the sheet resistance measurements. The color of the CdS thin film appears to be semi-transparent orange. The degree of the orange color darkens as the number of the deposition increases.

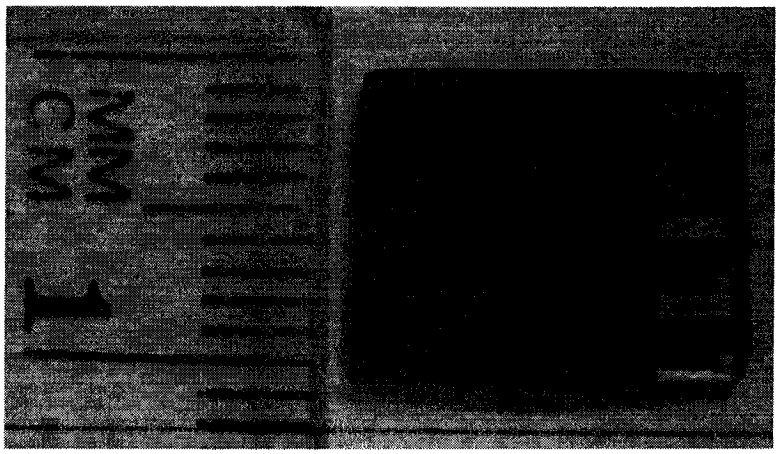

Fig. 5-2: A photo of actual deposited CdS thin film on the glass substrate with four gold electrodes.

5.3. RESULTS AND DISCUSSIONS

Three aspects of deposition conditions were examined: the temperature, the stir

rate, and the number of depositions. The findings for each are shown in the following sections.

5.3.1. VARIATION OF DEPOSITION TEMPERATURE

Three CdS samples were deposited at 55°C, 75°C, and 95°C respectively in this experiment to show the effect of deposition temperature. Fig. 5-3 shows the measurement results of the sheet resistance (R_s) versus time at three different deposition temperatures.

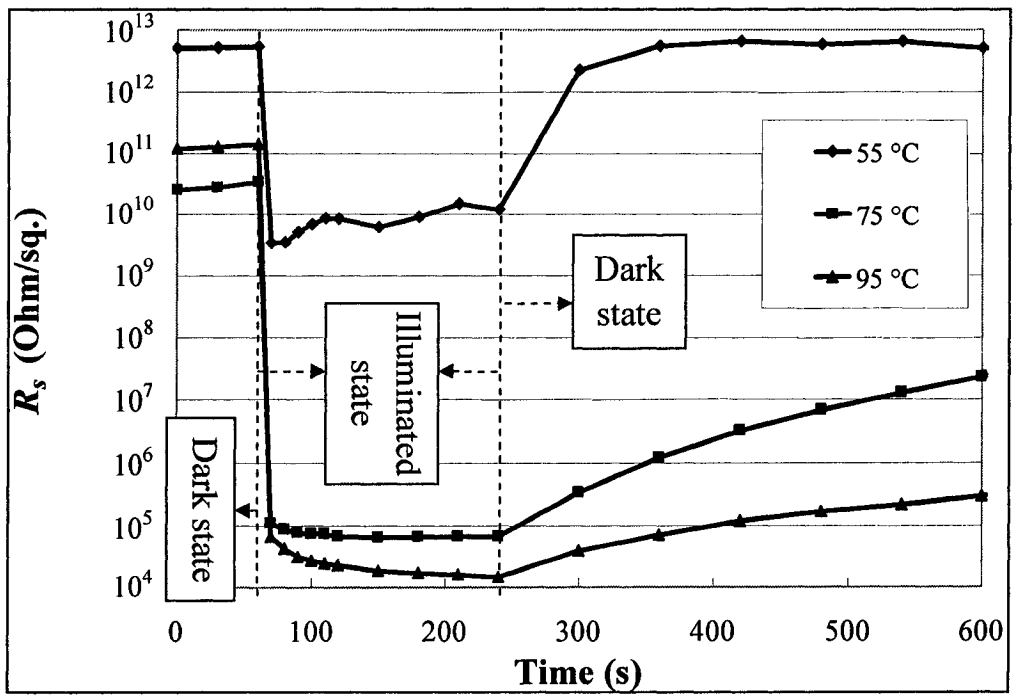

Fig. 5-3: Measured results of R_s for CdS thin films that were deposited with different temperatures.

It is observed that as the temperature increases, the R_s under illumination is decreased significantly. Therefore, this indicates that R_s is strongly correlated with the deposition temperature. The sample deposited at 95°C yields the best result of the

sheet resistance. However, the decay time of the photoconductive state becomes longer as the deposition temperature is increased. Since the main purpose of this work is to establish a CdS thin film with lowest possible R_s, the deposition temperature of 95°C is selected as the first essential condition.

5.3.2. VARIATION OF STIR RATE

The stirring action in the CBD solution provides a uniform layer of CdS thin film in a transparent-orange color to be deposited. In this section, the goal is to determine the optimal stir rate for depositing a CdS layer with lowest sheet resistance. Five CdS samples with different stir rates (100 ~ 800 rpm) were deposited at 95°C for 30 minutes each. Fig. 5-4 shows the measurement results of R_s under illumination for three minutes versus the stir rate.

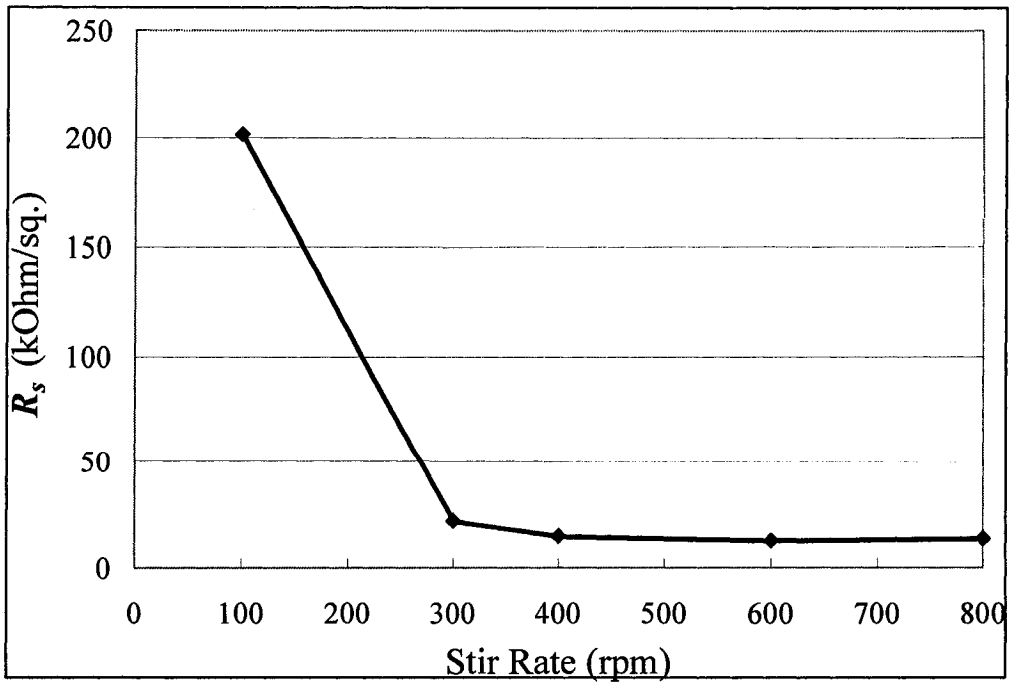

Fig. 5-4: Measured results of R_s under illumination for three minutes versus stir rate.

It is seen that the R_s reaches a minimum at the stir rate of 600 rpm. Further increase in stir rate did not show significant improvement on the R_s. The stirring action evenly mixes the CBD and produces a layer of uniform CdS thin film with a thickness around 0.5 ~ 0.8 μm for a 30-minute deposition. Therefore, the optimal stir rate is chosen to be at 600 rpm.

5.3.3. MULTIPLE NUMBERS OF DEPOSITIONS

The effect of the number of depositions was also investigated and studied. Theoretically, the relationship between the sheet resistance and the thickness of a thin film is

$$R_s = \rho\frac{L_x}{A} = \rho\frac{L_x}{w_x \cdot t} \Rightarrow \text{if } (L_x = w_x), \text{ then} \Rightarrow R_s = \frac{\rho}{t} \tag{5-3}$$

The dimensions in Eq. 5-3 are illustrated in Fig. 5-5. Therefore, the R_s can be reduced if the thickness of the thin film is increased.

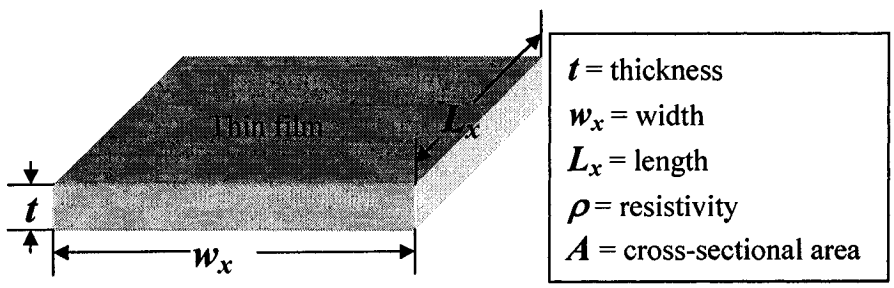

Fig. 5-5: The dimensions used for sheet resistance calculations in Eq. 5-3.

In order to increase the thickness of the CdS thin film, the deposition by CBD were repeated for three and six times for two separate samples to determine the effect of multiple depositions. The measured results of these two samples are plotted in Fig.

5-6 and the sample with only one deposition is also included for comparison.

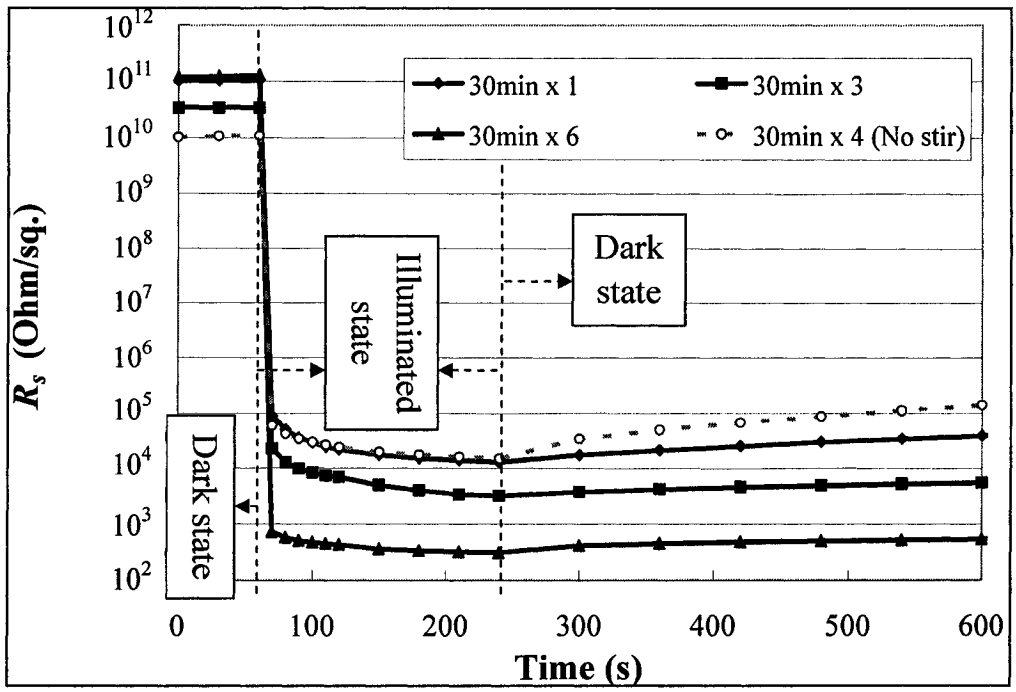

Fig. 5-6: Measured result of R_s versus time for CdS samples with different numbers of depositions.

It is observed that after three minutes of illumination the R_s decreases significantly as the number of depositions is increased. R_s values of 300 *Ω/square* under illumination for three minutes was obtained with six depositions. Also shown in Fig. 5-6 is a dashed line, which represents the CdS sample deposited for four times but without the stirring. The R_s of this sample after three minutes of illumination did not show any improvements when compared to the samples with stirring. Therefore, the stirring action is very critical in achieving an ultra-low sheet resistance CdS thin film since it provides uniform mixture to be deposited evenly.

The thickness of the CdS sample with six depositions was measured with Scanning Electron Microscopy (SEM) and found to be 5 *μm* and it is shown in Fig.

5-7. The conductivity of this CdS thin film is calculated to be 6.7 Ω^{-1} cm^{-1}. The sheet resistance of the CdS thin film can possibly be reduced even further with more depositions.

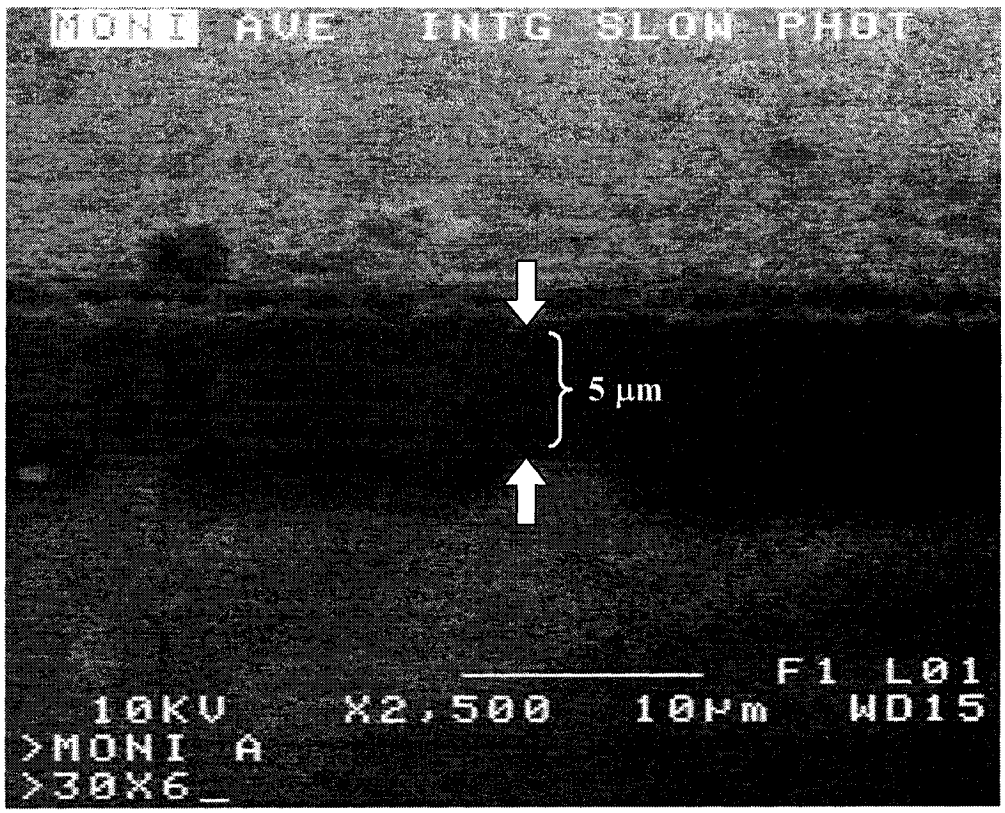

Fig. 5-7: SEM photo showing the thickness of the CdS thin film for the sample with six depositions.

5.4. POSSIBLE IMPROVEMENTS ON SWITCHING SPEED

The proposed CdS thin film has achieved the low sheet resistance (R_s) requirement. The switching speed from off state (high R_s) to on state (low R_s) is very fast (~ 10^7 Ω/s). However, the switching from on to off state is very slow (~ 10^{-3} Ω/s). Further investigations are necessary in order to improve this characteristic for an effective switching to be accomplished. Here, one possible enhancement is proposed

to increase the on to off switching speed. It is suspected that the prolonged duration of the on state is due to the excess amount of free carriers that are not able to recombine. Therefore, one method to provide the recombination paths is to deposit small metallic dot patterns in between the CdS thin film layers. The metallization layer used for metallic dots should be made to be very thin so it will not block the illumination too severely. Two configurations of different dot sizes and spacings, shown in Fig. 5-8 were experimentally fabricated and measured. Two layers of CdS were first deposited according to the procedure in TABLE 5-I. Then, the layer of metallic dots were deposited and it followed by another two layers of CdS.

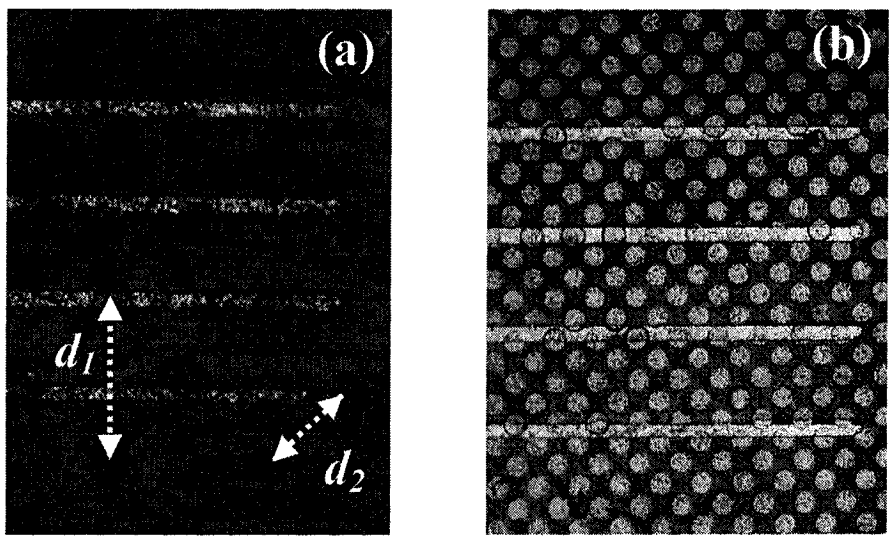

Fig. 5-8: Photos of the metallic dots deposited in between the layers of CdS thin films with (a) r = 50 μm and (b) r = 25 μm.

Fig. 5-9 illustrates the graph of sheet resistance (R_s) versus time when the

switching was taking place from on state (low R_s) to off state (high R_s).

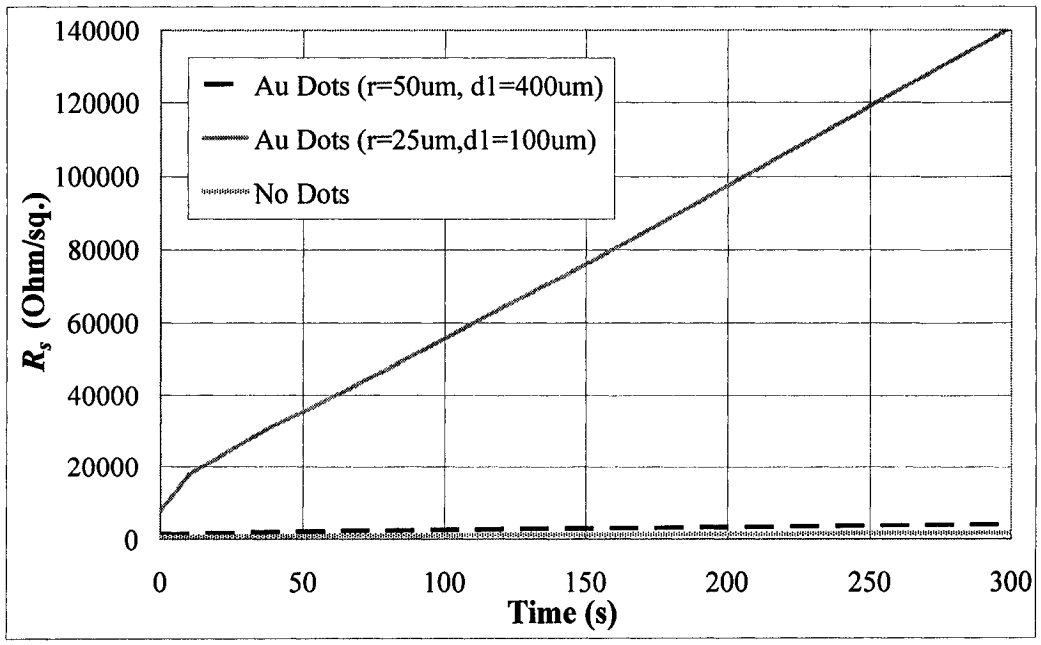

Fig. 5-9: Switching responses from on state to off state.

At zero seconds, the illumination was turned off and the samples were measured in dark so the switching responses from on to off can be obtained. The comparisons show the effect of the metallic dots on the switching speed. As observed from Fig. 5-9, the sample without the dots showed a decay of around 3 Ω/s. When the dots were deposited, the sheet resistance started to decay faster at 8 Ω/s and 420 Ω/s for dot radius of 50 μm and 25 μm respectively. Thus, the initial investigation suggests that the dot metallization could improve the switching speed. However, more vigorous exploration and analysis are necessary to truly enhance the speed down to millisecond range. Parameters such as the dot radius, metal thickness, number of metal layers, and heat treatment time should be examined carefully in order to achieve a fast switching

response.

5.5. SUMMARY

The sheet resistance of CBD deposited CdS thin film is studied. Three aspects of the deposition conditions were explored in order to accomplish the goal of preparing an ultra-low sheet resistance CdS thin film. It is found that the sheet resistance depends strongly on the deposition temperature, the stir rate, and the number of depositions. A set of optimal deposition conditions were established and a CdS thin film with sheet resistance of 300 *Ω/square* was successfully prepared. It is possible to utilize such thin films in microwave switching applications that require low sheet resistance. Initial investigation on the attempt to improve the switching speed from on state (low R_s) to off state (high R_s) showed moderate increase on the decay rate of the sheet resistance. Further works are required to fully enhance the switching speed.

6. APPLICATIONS: SWITCHABLE MICROWAVE FILTERS

In this chapter, the works on constructing a novel switchable microwave filter are studied. The illumination-sensitive CdS thin films were deposited on microwave electromagnetic bandgap (EBG) and inter-coupled split-ring resonator (SRR) structures to facilitate the optical switching of the propagating signals. Both simulated and experimentally measured results are presented.

6.1. ELECTROMAGNETIC BANDGAP STRUCTURES

When CdS is deposited entirely on the ground plane of an EBG structure, the periodic perforations are covered up. Thus, the CdS thin film's conductivity becomes a critical factor in the operation of the microwave structure. When the thin film is in the resistive state (Dark condition), the traveling wave experiences a discontinued ground plane and a filter response is produced accordingly. When the thin film is in the conductive state (Illuminated condition), the traveling wave experiences a continuous ground plane and therefore the structure behave like an ordinary microstrip line. Effectively, the responses of the constructed microwave filter can be turned on and off by the illumination. Fig. 6-1 shows an EBG structure with the CdS thin film deposited on the ground plane to cover up the perforations.

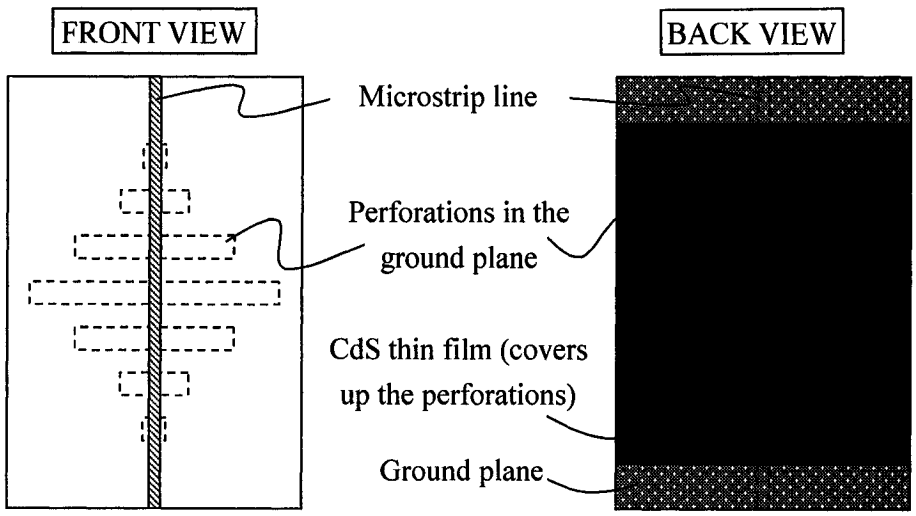

Fig. 6-1: EBG with linearly tapered slot-array pattern and the CdS thin film deposited on the ground plane to facilitate optical switching.

To enhance the switching performance, a conductive island is inserted in the center of each EBG perforations. Thus, the EBG pattern is now defined by boundaries of gaps instead of perforations (Fig. 6-2). The conductive islands are the same as the rest of ground plane, which are gold conductors.

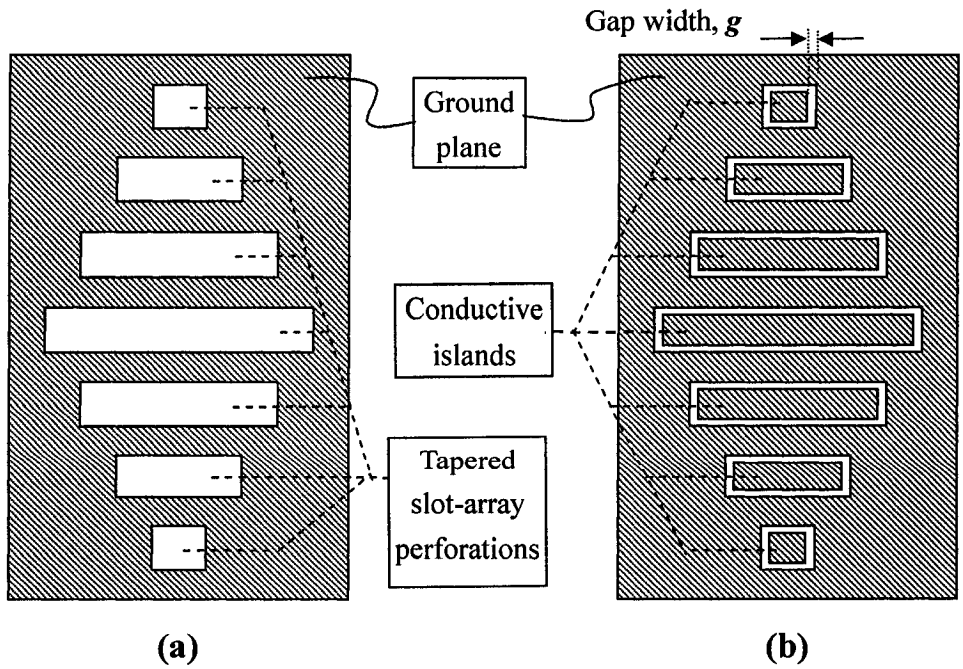

Fig. 6-2: A ground plane with (a) regular tapered slot-array perforations and (b) conductive islands

located in the center of each slot.

The proposed structure reduces the area that is covered by CdS while maintains the same periodically-induced stopband effect. By adding the conductive islands, the overall conductivity in the perforation regions is increased under the illuminated state because the gold has a much higher conductivity than the CdS thin film. The proposed structures with different gap widths (g) were simulated and the results are presented in the next section.

6.1.1. SIMULATIONS: THE EFFECT OF CONDUCTIVE ISLANDS

Agilent Advanced Design System's full-wave Momentum is used to simulate the proposed structures, which have the additional conductive islands. The gap width was varied from 5 μm to 100 μm to demonstrate the significance of the conductive islands. The linearly tapered slot-array structure discussed in Chapter 3 was utilized in this study. The simulation parameters are reiterated in TABLE 6-I.

TABLE 6-I: SIMULATION PARAMETERS FOR THE STRUCTURES WITH CONDUCTIVE ISLANDS

Structural Dimensions	Substrate type	Alumina (Al_2O_3)
	Dielectric constant (ε_r)	9.8
	Substrate thickness (h)	250 μm
	Microstrip line width (w)	250 μm
EBG Pattern Dimensions	Number of slots (n)	7
	Center slot length (L)	7.7 mm
	Structure period (a)	2.0 mm
	Slot length step (x)	1.2 mm
	Slot width (t)	0.5 mm
	Minimum slot length (v)	0.5 mm
	Gap width (g)	5 ~ 100 μm

First of all, the simulation results of S_{11} and S_{21} for structures without the effects of CdS thin film are presented in Fig. 6-3.

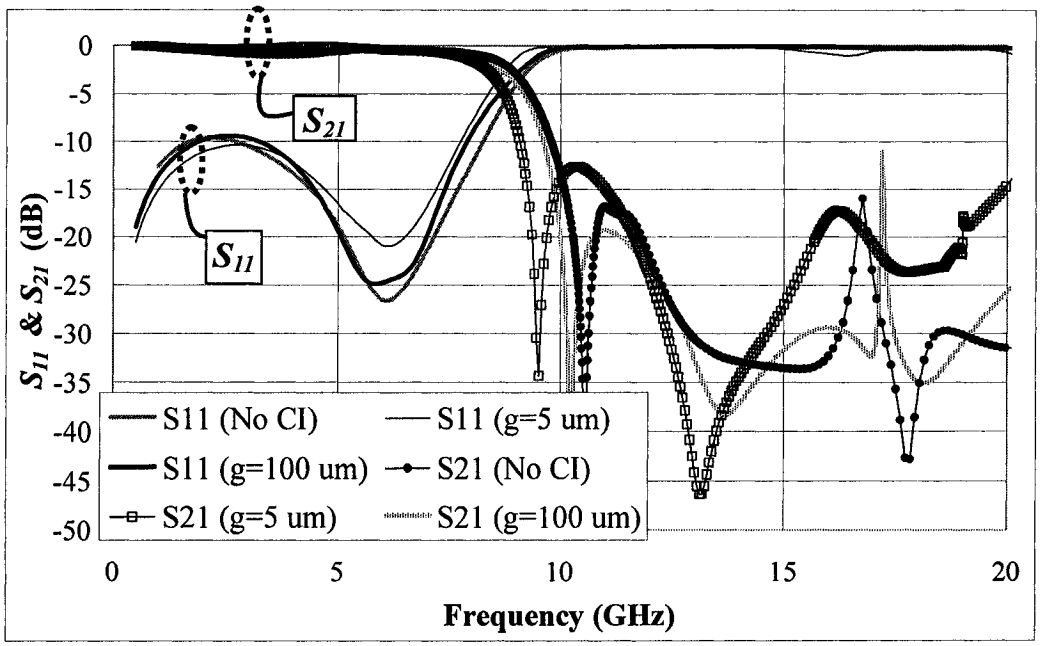

Fig. 6-3: Simulation results of S_{11} and S_{21} for the structures without the CdS thin film. (No CI = No conductive islands present)

It can be observed from Fig. 6-3 that the S-parameters behave similarly for structures with and without the conductive islands. There is a slight decrease in the 3 *dB* cutoff frequency as the gap width (g) is decreased. However, this variation is very small, which is only 0.5 *GHz* between the case of narrowest gap (g = 5 μm) and the case of no conductive islands. The results show that the additions of the conductive islands to the ground plane do not disturb the stopband effect of the EBG structure significantly. Therefore, it is feasible and realistic to utilize the proposed structure to enhance the optical switching of the microwave signals with the illumination-sensitive CdS thin films.

The next step is to simulate the proposed structure with a layer of CdS thin film, which is assumed to exhibit both high and low sheet resistances to predict the optical switching performance. In the following simulations, the sheet resistances for the illuminated and dark states are assumed to be 300 *Ω/square* and 10^9 *Ω/square* respectively so that this contrast would provide a sufficient switching ratio. Fig. 6-4 shows the S-parameters for three cases under dark state: g = 5 μm, g = 100 μm, and the structure without the conductive islands.

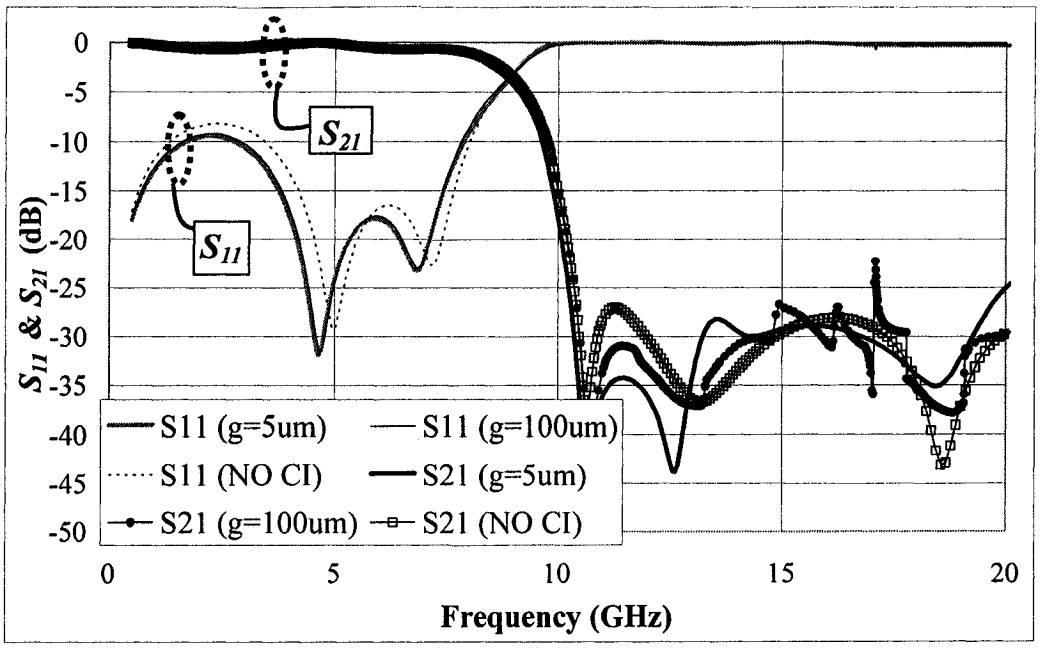

Fig. 6-4: S-parameters under dark state for g = 5 μm, g = 100 μm, and the structure without the conductive islands (NO CI).

It can be seen from Fig. 6-4 that the S-parameters for the three cases are almost identical. The 3 *dB* cutoff frequencies of the S_{21} are all located at around 9 *GHz*. When the CdS thin film operates under dark state, the sheet resistance is high and therefore the ground plane that contains the slot-array patterns is not continuous. Thus, the

structures maintained their stopband properties and the results shown in Fig. 6-4 are expected. When the CdS thin film is exposed to illumination, the sheet resistance reduces significantly and renders the film to be conductive. Thus, the ground plane becomes continuous and the stopband effect of the EBG structure is eliminated. Fig. 6-5 shows the simulated S_{21} of the structures with the gap widths (g) vary from 5 to 100 μm under illuminated state.

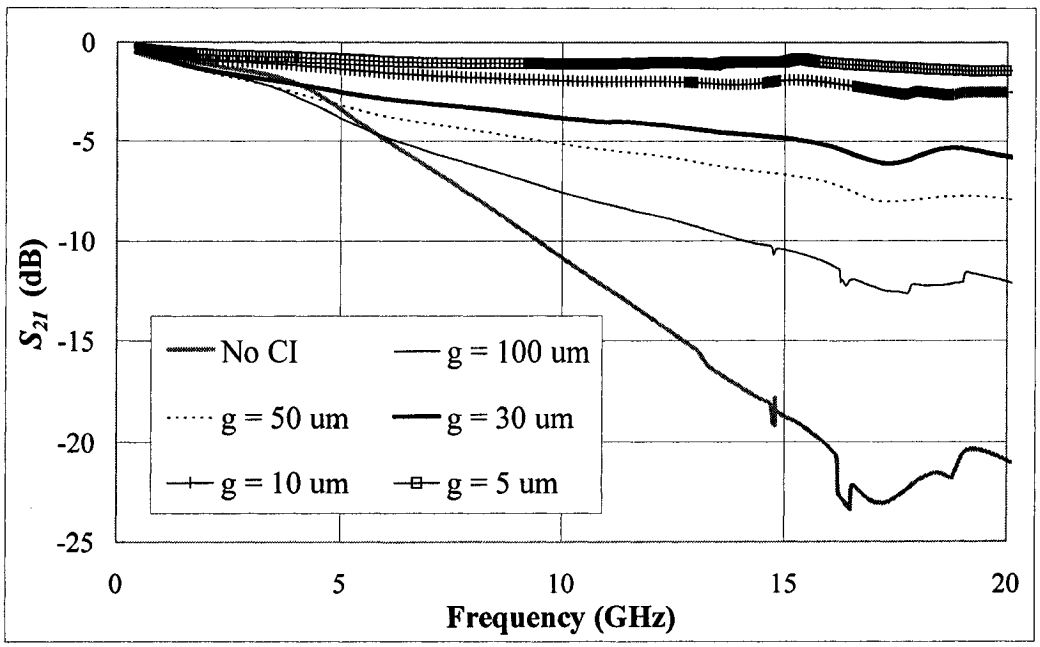

Fig. 6-5: Simulated S_{21} with g varies from 5 to 100 μm under illuminated condition. (No CI = No conductive islands present)

The importance of the conductive islands and the gap width (g) can be observed in Fig. 6-5. As g is decreased, the insertion loss (S_{21}) reduces significantly. At 13 *GHz*, the insertion loss reduced from 16 *dB* to 1 *dB* when compared between the case of g = 5 μm and the case of no conductive islands. Therefore, by adding the conductive islands into the EBG perforations, it facilitates the possibility of making an optically

switchable device. Fig. 6-6 shows a comparison of S_{21} between illuminated and dark states for the case of $g = 5\ \mu m$. The dark to illumination insertion loss ratio at 13 *GHz* is about 40 (40 *dB* to 1 *dB*).

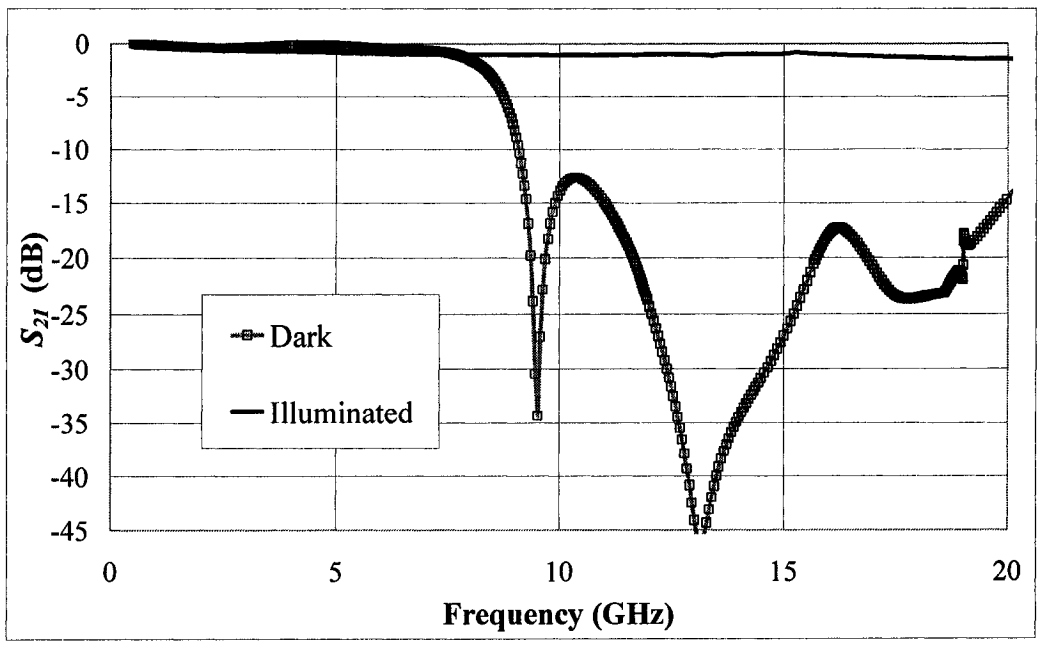

Fig. 6-6: Comparison of S_{21} between illuminated and dark states (the case of $g = 5\ \mu m$).

6.1.2. EXPERIMENTAL MEASUREMENTS AND COMPARISONS

Actual samples of tapered slot-array EBG structures with and without the conductive islands were fabricated according to the dimensions shown in TABLE 6-I. The gap widths (g) in the ground plane of the EBG structure were constructed with standard photolithography steps. The case of $g = 30\ \mu m$ was used to demonstrate the effect of the conductive islands. After the EBG structures were constructed, the CdS thin film was then deposited on the ground plane to cover up the perforation patterns. The deposition method for the CdS layer was presented in Chapter 5. The vector

network analyzer was used to measure the S-parameters of the samples in both illuminated and dark conditions. Fig. 6-7 shows photos of the fabricated samples for measurements. The results are compared to simulated ones and they are presented in this section.

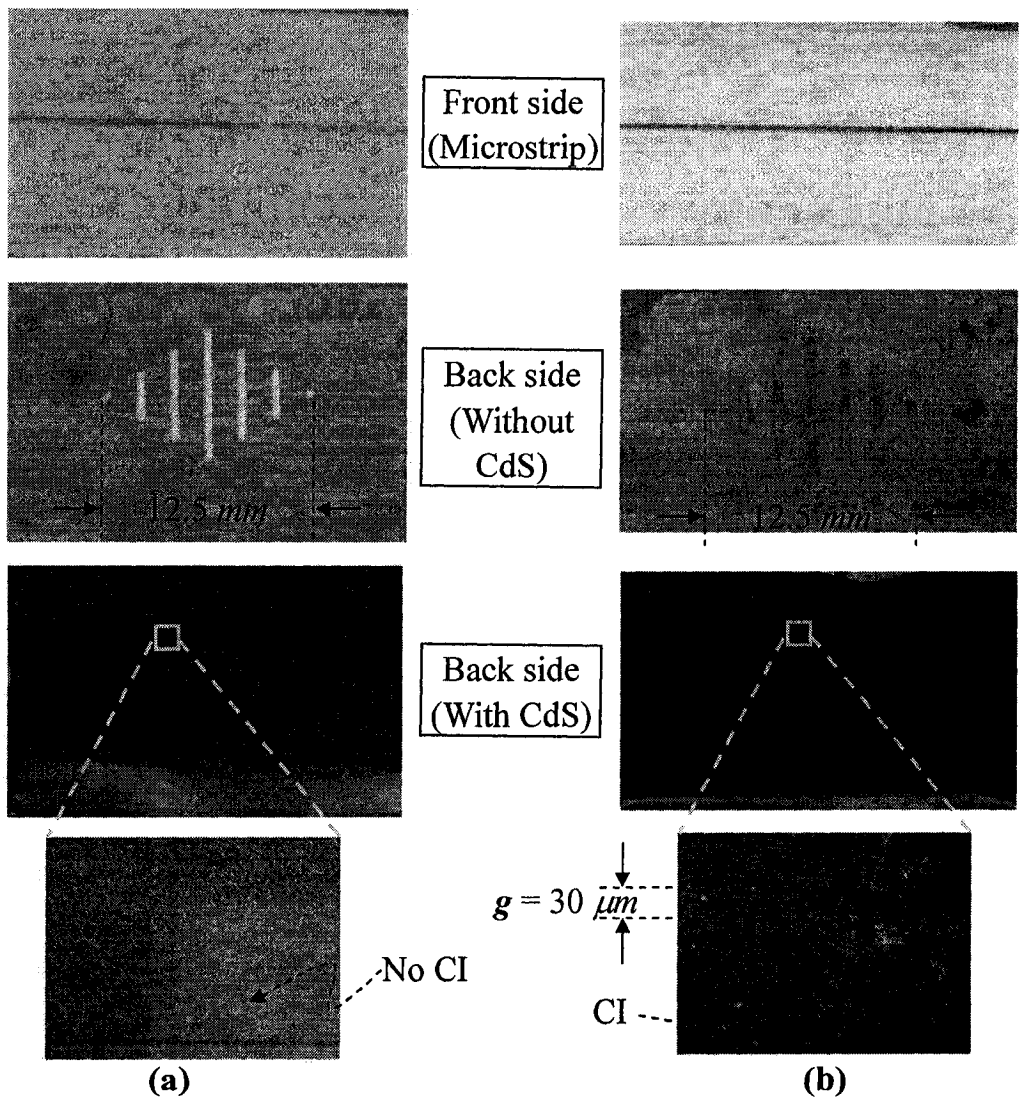

Fig. 6-7: Photos of fabricated samples (a) without and (b) with the conductive islands (CI). CdS thin films were deposited on the ground plane of the samples to cover up the perforations.

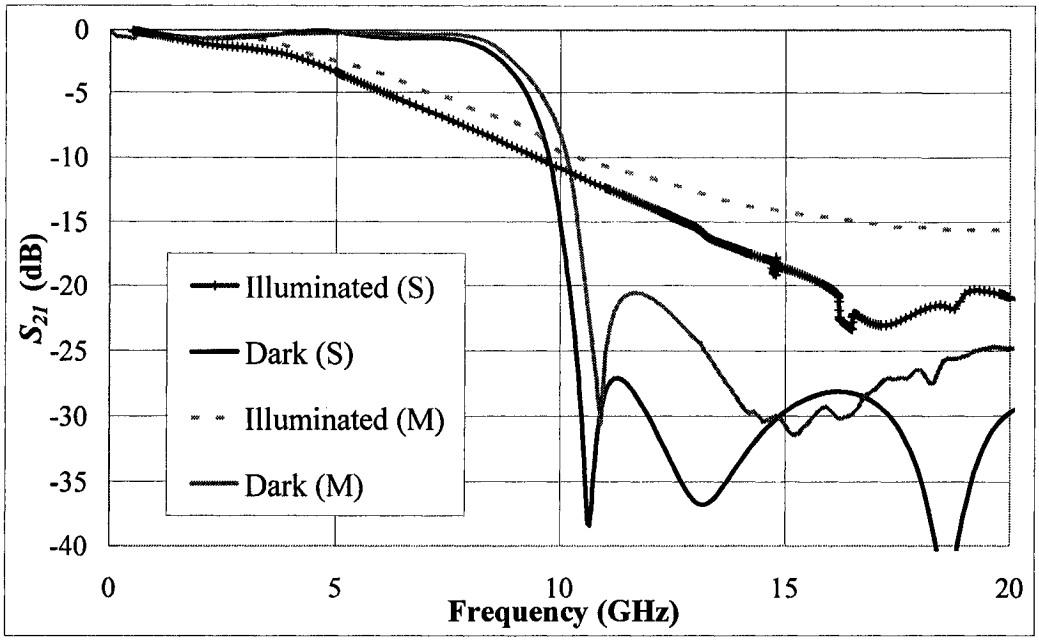

Fig. 6-8: Comparison of simulated (S) and measured (M) S_{21} for the case where no conductive islands are presented in the structures.

Fig. 6-8 shows the comparisons of simulated and measured S_{21} results for the structures that do not contains the conductive islands. It is seen that the results for the dark state match very well. For the illuminated state, the measured S_{21} has a slightly lower insertion loss. The reason for this occurrence might be because the sheet resistance of the actual deposited CdS thin film under illuminated condition was lower than 300 *Ω/square*, which is the sheet resistance value used in the simulations. However, the insertion loss for the illuminated state is still large when the conductive islands are not presented. The dark to illumination insertion loss ratio for the measured results at 13 *GHz* is 1.9 (24.1 *dB* to 12.7 *dB*). The ratio is equal to 2.4 for the simulated results.

Fig. 6-9 illustrates the comparisons of simulated and measured S_{21} for the

structures that contain the conductive islands. The gap width (g) is equal to 30 μm in this case. The insertion loss for the illuminated case improved significantly when it is compared to the structure without the conductive islands. The dark to illumination insertion loss ratio for the measured results at 13 *GHz* is 5.6 (31.3 *dB* to 5.6 *dB*). The ratio is equal to 8.6 for the simulated results. Therefore, by inserting the conductive islands, the effective ratio increased almost three times. Moreover, from the simulation analysis, this performance can be improved even further by reducing g.

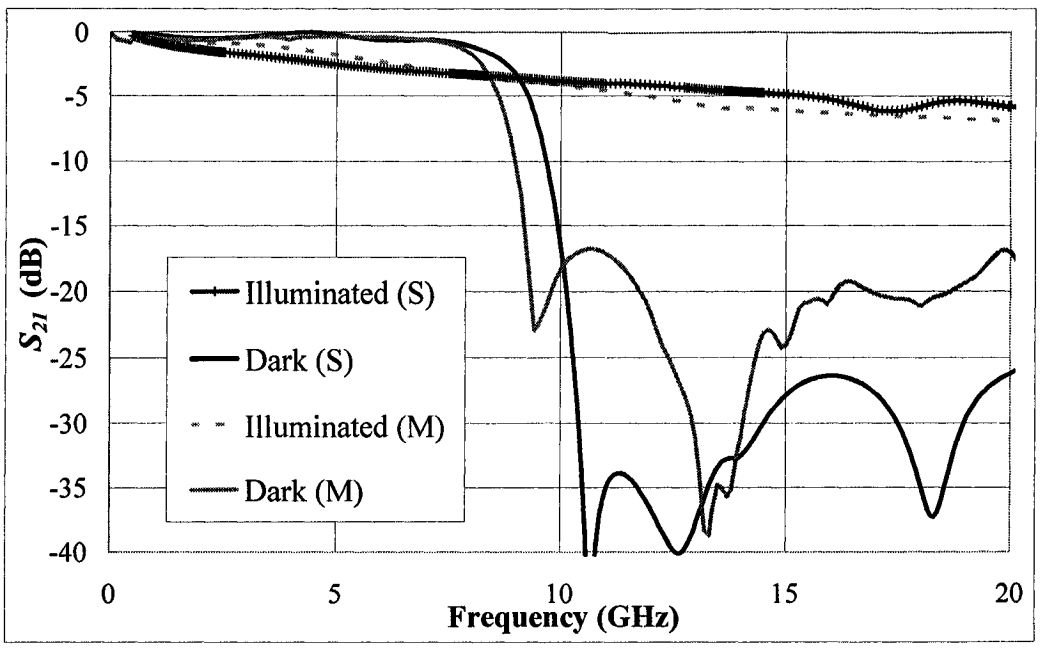

Fig. 6-9: Comparison of simulated (S) and measured (M) S_{21} for g = 30 μm.

The switching of EBG structures by means of illumination has been demonstrated successfully. Also, the switching performance can be enhanced significantly with the addition of conductive islands. Therefore, a novel EBG structure that is suitable for optical switching has been constructed and achieved.

6.2. SPLIT-RING RESONATOR STRUCTURES

The inter-coupled split-ring resonator structures presented in Chapter 4 are also potentially suitable for optical switching applications. In this section, this option is explored and studied. Both simulation and measurement results were performed to provide a thorough analysis.

In order to achieve switching, the passband effect induced by the inter-coupled split-ring resonators has to be controlled. One method to accomplish this is to deposit a layer of CdS thin film on the microstrip line where the inter-coupled split-ring resonators were constructed. Thus, the passband effect can be switched on and off with the applied illumination because of the CdS thin film's light-sensitive property. When the structure is under dark condition, it retains the characteristic of a bandpass filter. On the other hand, the structure becomes an ordinary microstrip transmission line when it is exposed to illumination. Fig. 6-10 shows an inter-coupled split-ring resonator structure with a layer of CdS thin film deposited on the top to facilitate the optical switching.

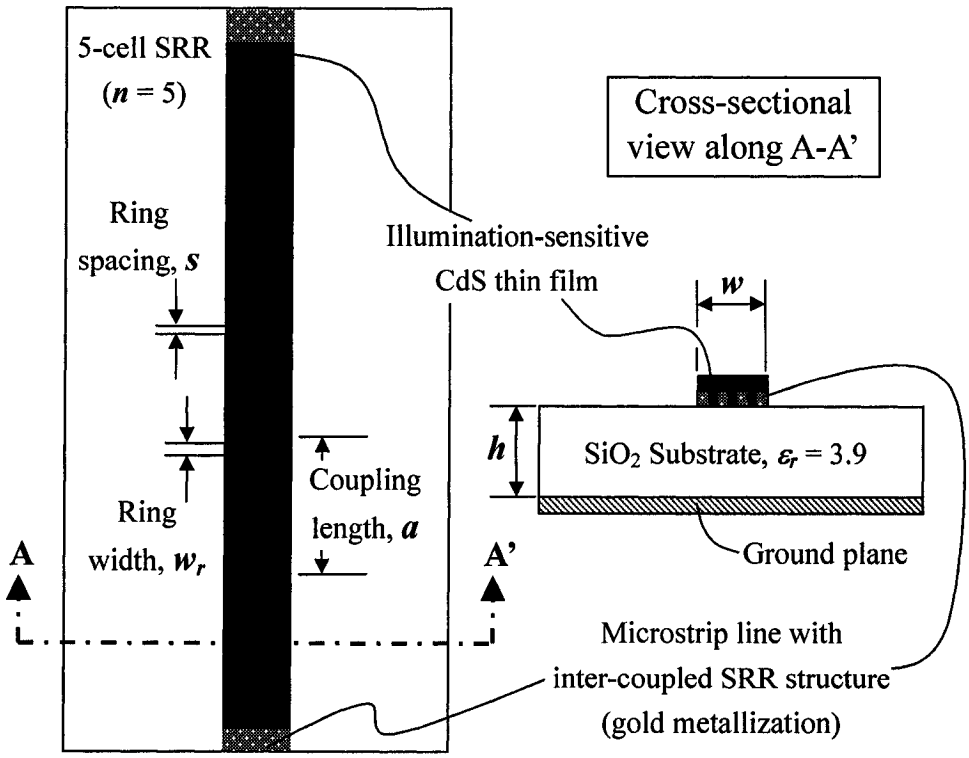

Fig. 6-10: Inter-coupled SRR structure with a layer of CdS thin film deposited on the top to facilitate optical switching.

From Chapter 4, it is already known that the coupling length (a) is directly related to the arithmetic mean of the center passband frequency. Also, the corresponding ring spacing (s) and width (w_r) can be determined from the calculated equivalent capacitance and inductance of the resonator. Therefore, this analysis will not be repeated in this section. Instead, the effect of the CdS thin film layer deposited on top of the inter-coupled split-ring resonator structure is explored.

6.2.1. SIMULATIONS: THE SWITCHING EFFECT OF CDS THIN FILMS

In the following simulations, the sheet resistances for the illuminated and dark states are assumed to be 300 *Ω/square* and 10^9 *Ω/square* respectively. Two groups of

structures were simulated with the addition of the CdS layer. The structure period (a) was varied in the first group and the number of split-ring resonator cells (n) was varied in the second group. The structural dimensions used in the simulations are summarized in TABLE 6-II.

TABLE 6-II: THE STRUCTURAL DIMENSIONS USED IN THE SIMULATIONS

Substrate type			Corning 1059 (SiO_2)	
Dielectric constant (ε_r)			3.9	
Substrate thickness (h)			0.37 *mm*	
Microstrip line width (w)			0.80 *mm*	
	Structure period (a)	Ring spacing (s)	Center passband frequency (f_0)	Number of SRR cells (n)
Group #1	2.40 ~ 3.60 *mm*	0.030 *mm*	12 ~ 18 *GHz*	5
Group #2	2.70 *mm*	0.030 *mm*	16 *GHz*	3 ~ 6

Fig. 6-11 shows the S_{21} responses for the structures in group #1 under dark condition. Four inter-coupled split-ring resonator structures with different structure period (a) were simulated with the CdS layer having a sheet resistance of 10^9 *Ω/square*. The passband is clearly observed since the microstrip lines were still remained discontinuous with the split-ring patterns on the top. At 5 *GHz*, the insertion losses are all higher than 40 *dB*.

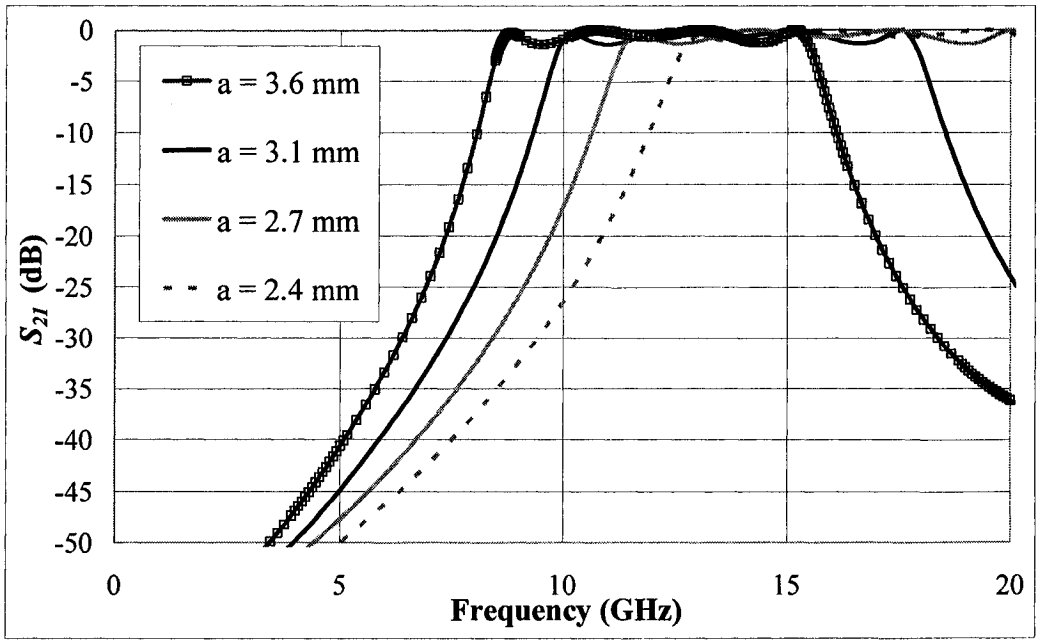

Fig. 6-11: S_{21} of the structures in group #1 (variation of a) under dark condition.

Fig. 6-12 shows the S_{21} and S_{11} responses for the structures in group #1 under illuminated condition. In this case, the passband regions were eliminated since the microstrip lines became continuous due to the conductive CdS thin film (Sheet resistance = 300 *Ω/square*) on the top. The insertion losses (S_{21}) did not vary significantly when the structure period is changed. At 5 *GHz*, the insertion losses are around 1.3 *dB* while the return losses (S_{11}) are below 20 *dB*. Therefore, the dark to illumination insertion loss ratio for a = 3.1 *mm* at 5 *GHz* is 34 (44.7 *dB* to 1.3 *dB*).

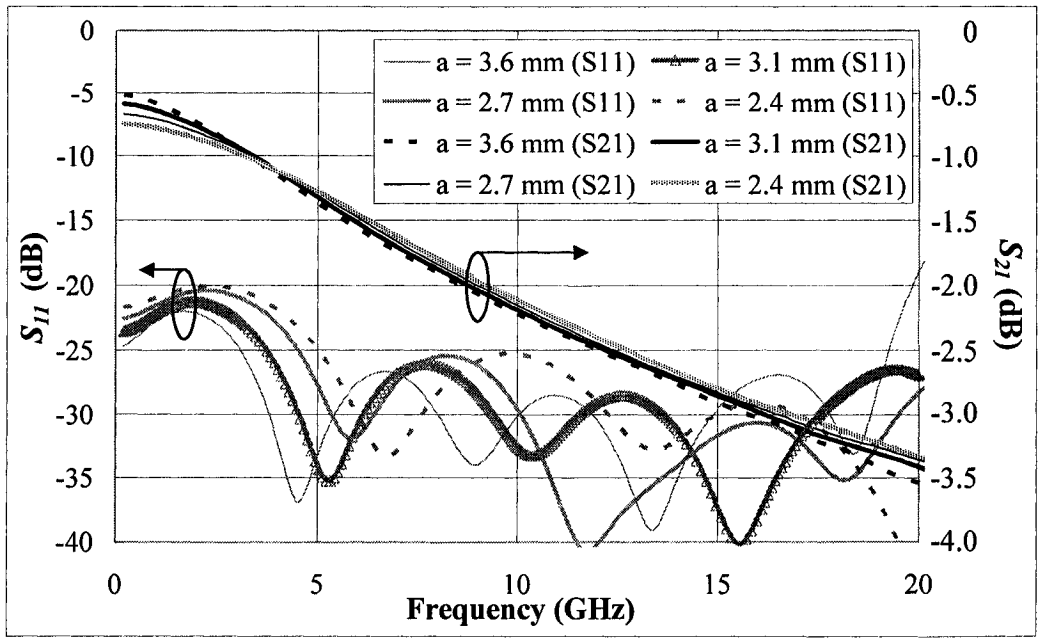

Fig. 6-12: S_{21}/S_{11} of the structures in group #1 (variation of a) under illuminated condition.

Simulation group #2 examines the relationship between the numbers of split-ring resonator cells with respect to the switching performance. Fig. 6-13 shows the simulation results of four split-ring resonator structures with different n under dark condition (Sheet resistance of the CdS layer is 10^9 *Ω/square*).

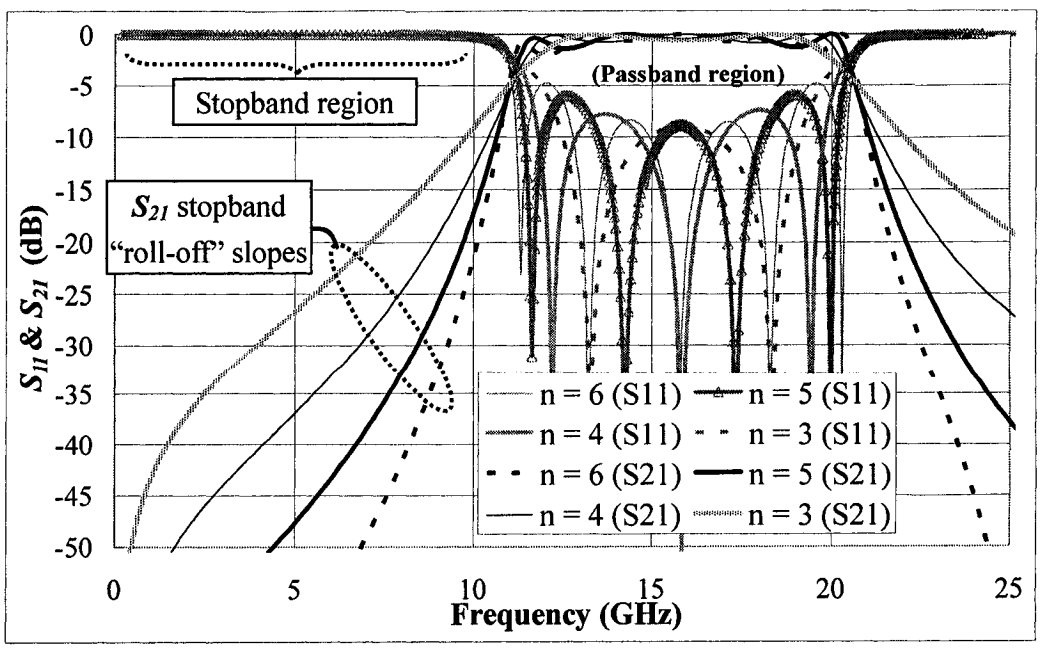

Fig. 6-13: S_{21}/S_{11} of the structures in group #2 (variation of n) under dark condition.

It is observed that the passband region centered at 16 *GHz* is the same for all cases because the structure periods (a) were kept constant at 2.7 *mm*. However, the "roll-off" slopes in the stopband region decrease significantly as n is decreased. This means that the band edges are less defined and the stopband ability is decreased. Fig. 6-14 shows the S-parameters of the same structures under illuminated condition (Sheet resistance of the CdS layer is 300 *Ω/square*).

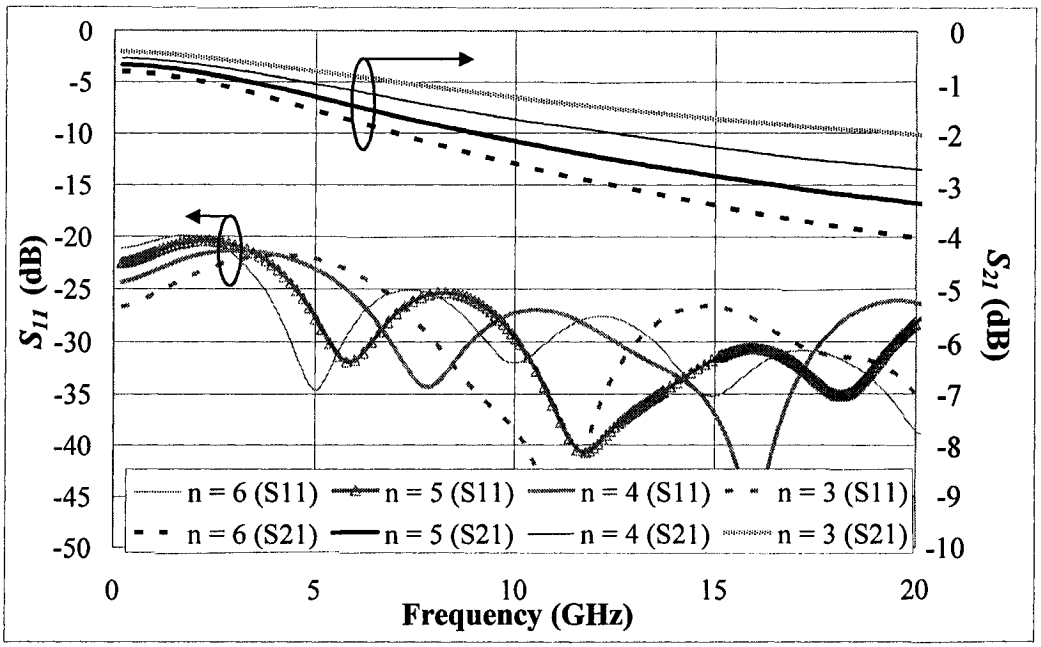

Fig. 6-14: S_{21}/S_{11} of the structures in group #2 (variation of n) under illuminated condition.

Again, the passband regions were eliminated when the CdS thin films become conductive. It is observed that the insertion loss (S_{21}) at 5 *GHz* increases from 0.8 *dB* to 1.6 *dB* as n is increased from 3 to 6. As the frequency increases, this effect is amplified (1.7 *dB* to 3.4 *dB* at 15 *GHz*). Meanwhile, the return losses (S_{11}) are below 20 *dB* for all cases. The insertion loss ratio for $n = 6$ at 5 *GHz* is 38 (61 *dB* to 1.6 *dB*).

Therefore, the optical switching with the illumination-sensitive CdS thin film deposited on the split-ring resonator structures is successfully demonstrated with the simulations. To verify these results, two actual split-ring resonator structures with the deposition of CdS thin films were fabricated and measured. The comparisons of simulation and measurement results are presented in the next section.

6.2.2. EXPERIMENTAL MEASUREMENTS AND COMPARISONS

Two inter-coupled split-ring resonator structure with different structure period (a) and cell number (n) were fabricated to demonstrate the optical switching. The substrate type, thickness, and microstrip line width used to construct the split-ring resonator structures are the same as the values used in the simulations shown in TABLE 6-II. The rest of the structural dimensions are shown in TABLE 6-III. Fig. 6-15 shows the photos of fabricated inter-coupled split-ring resonator structures with and without the CdS thin films.

TABLE 6-III: DIMENSIONS OF SPLIT-RING RESONATORS USED TO FABRICATE THE ACTUAL SAMPLES

Sample No.	Structure period (a)	Ring spacing (s)	Center passband frequency (f_0)	Number of SRR cells (n)
A	3.10 *mm*	0.030 *mm*	14 *GHz*	5
B	2.70 *mm*	0.030 *mm*	16 *GHz*	6

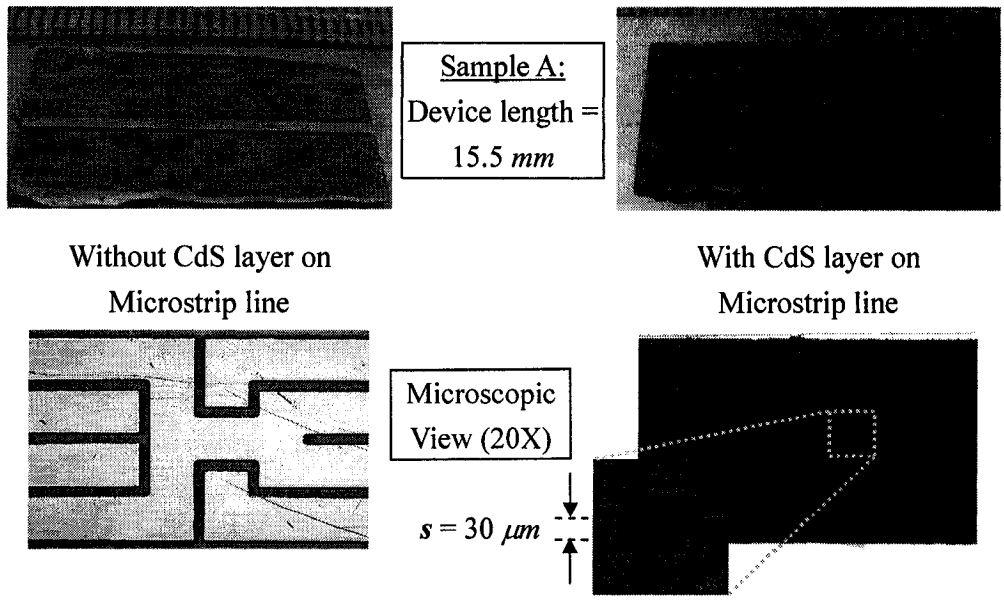

Fig. 6-15: Photos of fabricated inter-coupled split-ring resonator structures with and without the CdS thin films.

Both samples were measured with the vector network analyzer and the results are compared to the simulated ones. Fig. 6-16 shows both measured and simulated S_{21} results. They matched very well for the illuminated case. However, the measured result under the dark condition shows a reduced roll-off slope in the low frequency stopband region. Thus, the dark to illumination insertion loss ratio at 5 *GHz* for the measured result is equal to 13 (19 *dB* to 1.5 *dB*), which is not as large as the simulated one (the ratio = 34).

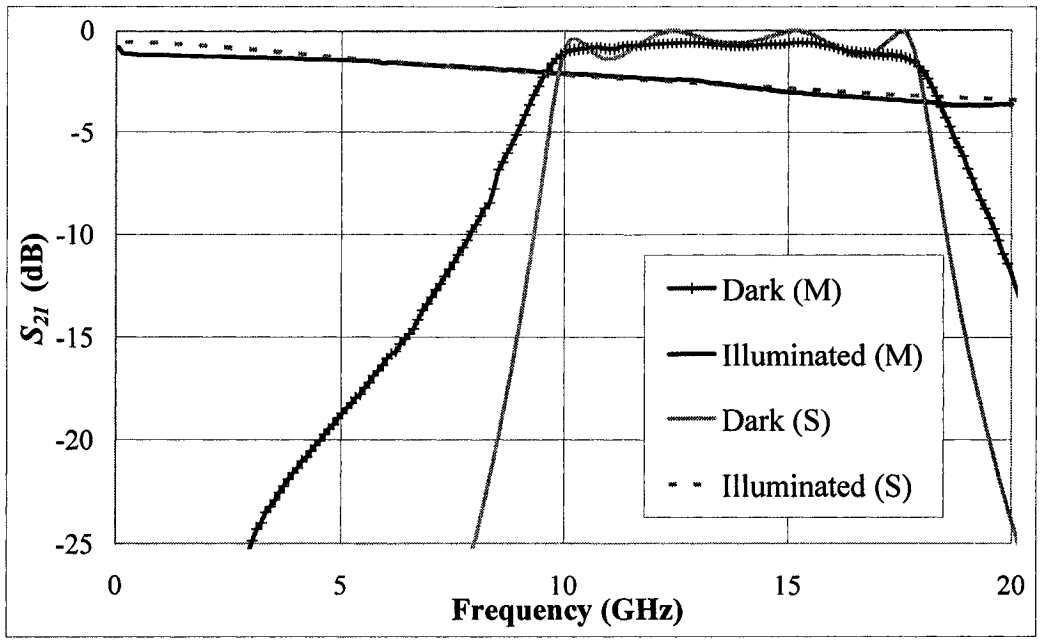

Fig. 6-16: The comparisons of measured (M) and simulated (S) S_{21} for sample A under dark/illuminated conditions.

Fig. 6-17 illustrates the switching responses of sample B obtained from both the simulations and the measurements. In this case, the structure period (a) is reduced and the number of the split-ring resonator cells (n) is increased. It is observed that the passband region shifted to higher frequencies due to the reduced a. Both the passband regions and the illuminated S_{21} responses matched very well between the simulations and the measurements. At 5 *GHz*, the dark to illuminated insertion loss ratio is 12 (23 *dB* to 1.9 *dB*) from the measured S_{21}. Meanwhile, the ratio equals to 38 (61 *dB* to 1.6 *dB*) for the simulated S_{21}.

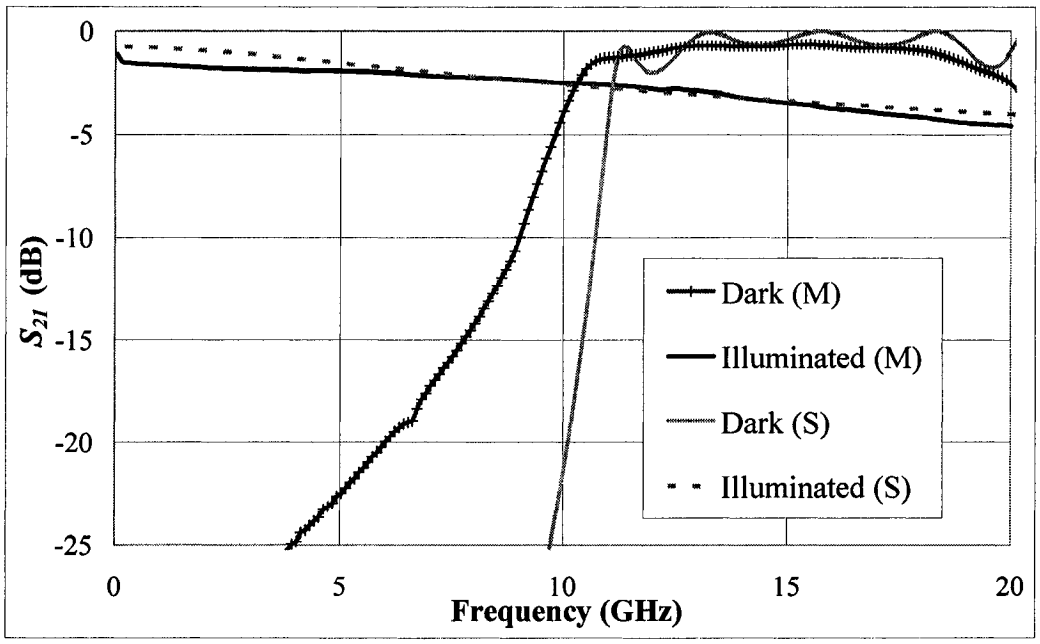

Fig. 6-17: The comparisons of measured (M) and simulated (S) S_{21} for sample B under dark/illuminated conditions.

6.3. SUMMARY

In this chapter, the possibility of building a switchable structure is explored and studied. The illumination-sensitive CdS thin film investigated in Chapter 5 is utilized as the switching medium. Therefore, it is crucial to find the appropriate microwave structure to complete this task. It has been shown that the electromagnetic bandgap (EBG) structures can be enhanced and modified by adding the conductive islands in the perforations. The greatest advantage of this feature is to make the EBG structures suitable for switching and thus the insertion loss is improved significantly. At the same time, the conductive islands do not affect EBG structures' ability to create stopband regions. The switching ratio of the enhanced EBG structure is almost three times

higher than the ordinary EBG structure. Therefore, the conductive islands are an integral part of the optically switchable microwave structure.

Inter-coupled split-ring resonator (SRR) structures are also a good candidate for optical switching due to their unique arrangement of ring patterns. It has been shown that a bandpass filter constructed with defining the SRR patterns on a microstrip line can be switched to an ordinary microstrip line with a switching ratio of higher than 10 at 5 *GHz*.

TABLE 6-IV: SUMMARIZED RESULTS OF THE SWITCHABLE STRUCTURES OBTAINED BY MEASUREMENTS

Insertion Losses & Switching Ratios	EBG (without CI[#])	EBG (with CI)	SRR (sample A)	SRR (sample B)
IL[*] at 13 *GHz* (Dark)	24.1 *dB*	31.3 *dB*	--	--
IL at 13 *GHz* (Illuminated)	12.7 *dB*	5.6 *dB*	--	--
IL at 5 *GHz* (Dark)	--	--	19.0 *dB*	23.0 *dB*
IL at 5 *GHz* (Illuminated)	--	--	1.5 *dB*	1.9 *dB*
Switching Ratios	**1.9**	**5.6**	**13**	**12**

[#]CI = Conductive Islands; [*]IL = Insertion Loss

Even though the S_{21} dark to illuminated ratios of the measured results are not as high as the simulated ones, but the optical switching with a ratio of higher than 10 is successfully demonstrated with experimentally fabricated samples. For the EBG structures, the switching ratio can be improved by reducing the gap width (***g***) that surrounds the conductive islands. From the simulation results, the switching ratio can be improved up to 40 when ***g*** is reduced to 5 *μm*. For the SRR structures, the switching ratio can be improved by either reducing the number of cells (***n***) or the ring

spacing (*s*). Therefore, the optical switching of microwave signals is proven to be achievable by utilizing the proposed structures and the CdS thin films.

7. CONCLUSIONS AND FUTURE WORKS

7.1. THESIS SUMMARY

In this thesis work, novel perforation patterns used to construct electromagnetic bandgap (EBG) structures and innovative utilization of the split-ring resonator (SRR) were proposed and verified by experiments. Also, the illumination-sensitive Cadmium Sulfide (CdS) thin films were applied to the proposed structure to enable the switching of the transmission properties. Thus, switchable microwave structures were successfully achieved and demonstrated. Main contributions to the field of microwave periodic structures and their applications are stated as follow:

1. The double-stopband EBG structure has been proposed and experimentally verified. The critical structural ratios were found so the construction of a flat passband region is achieved in between two stopband regions. Flexibility of the passband frequency has also been confirmed.
2. Linearly and non-linearly tapered slot array EBG structures have been proposed and experimentally verified. The novel tapered array pattern not only exhibits a wider stopband region but also takes 40% less space to construct when compared to ordinary rectangular patterns. The design technique for tapered array EBG structures has also been developed.
3. Inter-coupled SRR structure has been proposed and experimentally constructed on

the microstrip line to build microwave bandpass filters. The novel construction demonstrated an exceptionally wide fractional bandwidth of over 68%. Meanwhile, the analysis showed that the proposed structure is compatible with common filter responses. The control of passband frequency and fractional bandwidth has been achieved.

4. Ultra-low sheet resistance CdS thin film has been experimentally prepared. Multiple depositions allow the film to achieve a sheet resistance of 300 *Ω/square* when incident with a green laser pointer having an illumination intensity of 50 mW/cm^2. Highest dark state sheet resistance recorded was 10^{12} *Ω/square*.
5. Optically controlled microwave filters have been proposed and experimentally verified. The CdS thin films were deposited on both proposed tapered array EBG structure and inter-coupled SRR structure. Addition of conductive islands to the EBG structure enhanced the switching significantly.

Detailed summary on the findings and the analysis are presented in the following:

In Chapter 3, three types of EBG structures were investigated: the double-stopband structure, the linearly and non-linearly tapered array (TA) structures. The double-stopband EBG structure can be constructed simply by implementing one-dimensional rectangular periodic perforations in the ground plane of a microstrip transmission line. With the proper adjustment of the perforation's length and width to

the structure period ratios, the frequencies of the stopband regions can be controlled. Thus, the configuration creates a passband region in between the two stopbands. The double-stopband EBG structure was demonstrated by experiment and a passband region from 14 to 18 *GHz* was achieved with a device that is 30.8 *mm* in length.

EBG structure's physical length must be reduced in order for it to be practical. Thus, the TA patterned EBG structure was proposed to accomplish this goal. Three aspects of the linearly TA patterned EBG structures were examined: the structure period (a), the number of slot (n), and the length of slot (L). It has been found that the structure period did not notably affect the stopband frequency like in the conventional periodic EBG structures. Instead, it was the lengths of the tapered slots that were controlling the cutoff frequency. As the center length of the tapered slot increases, the cutoff frequency is decreased significantly. Therefore, the overall length of the device can be maintained while the stopband frequency varies. To fully appreciate and maximize the effect of the tapered array EBG structure, non-linearly tapered slots were utilized. It has been demonstrated that a 9-slot non-linearly TA patterned EBG structure with a length of 12.5 *mm* can generate a stopband from 9 to 20 *GHz*. Meanwhile, the minimum attenuation in the stopband was 25 *dB* and the average insertion loss in the passband was 1 *dB*. It would require the conventional EBG structure to have a length of 21.6 *mm* to achieve a stopband from 9 to 18 *GHz*. The

non-linearly TA patterned EBG structure is only 57% in length of the conventional structure and it does not have the spurious S_{11} ripple in the passband.

In Chapter 4, split-ring resonators (SRR) were implemented in a form of inter-coupled configuration on the microstrip line and the overall structure was investigated. This configuration was found to have an exceptionally wide fractional bandwidth while the implementation did not require extra space. The passband frequency was discovered to have a strong dependence on the SRR's structure period. A fractional bandwidth of 68.2% with a maximum insertion loss of 0.81 *dB* was achieved with a fabricated sample having a length of 15.5 *mm*. Also, the fractional bandwidth can be controlled and designed easily while the overall filter performance can be enhanced further when a transfer function's coefficients are applied. Therefore, the inter-coupled SRR structure can be utilized as an efficient bandpass filter.

In Chapter 5, a set of optimal deposition condition was established for the deposited CdS thin film to have a low sheet resistance. Chemical bath deposition was utilized while the deposition temperature, the stir rate, and the number of deposition were examined. It was demonstrated that a CdS thin film having an illuminated sheet resistance of 300 *Ω/square* can be achieved with a deposition temperature of 95 °C, a stir rate of 600 *rpm*, and six times of repeated depositions. Initial investigation on improving the switching speed was carried out and moderately enhanced results have

been observed.

In Chapter 6, the CdS thin films were applied to EBG and inter-coupled SRR structures to construct optically switchable microwave filters. To enhance the switching performance of the EBG structure, the conductive islands were inserted to the middle of the perforations. Thus, a switching of the transmission coefficient (S_{21}) from 31.3 *dB* (dark state) to 5.6 *dB* (illuminated state) at 13 *GHz* was demonstrated for the 7-slot linearly tapered array EBG structure. Meanwhile, a switching of S_{21} from 19 *dB* (dark state) to 1.5 *dB* (illuminated state) was achieved for the 5-cell inter-coupled SRR structure. Therefore, both the lowpass and bandpass microwave filters were successfully realized as switchable structures with the application of the illumination-sensitive CdS thin films.

Furthermore, the main advantages of the double-stopband EBG structure are its simple implementation and defined passband region. The drawback of bulky physical size can be addressed with the tapered array EBG structures, which not only offer significantly reduced sizes but also possess the ability to create wide stopband. In addition, non-linearly tapered structures offer customized results that are simple to design. The inter-coupled split-ring resonator structures have main advantages such as wide fractional bandwith and compatibility with microstrip line. Thus, no extra space is required to implement this component as a bandpass filter. When these microwave

periodic structures are integrated with the developed low sheet-resistance CdS thin film, novel optically controlled microwave structure is produced. The switchable filter provides an opportunity to be integrated in optoelectronic applications. Also, it does not have any mechanical parts and it is simple to implement.

In conclusion, the microwave structures based on EBG and inter-coupled SRR patterns were explored and analyzed in this thesis work. The possibility of switching their stopband effects by optical means were also investigated and demonstrated. These will allow the advancement of both EBG and inter-coupled SRR structures in practical microwave filter applications and improve the understanding of these periodic structures.

7.2. POTENTIAL FUTURE WORKS

Much works remain to be done to improve the performance of these periodic structures. Also, the quality of the CdS thin film needs to be improved for a shorter switching time. Parameters such as the metallization patterns, metal thickness, layers of metallization and heat treatment length should be examined further to achieve a faster switching speed. New switching structures could be developed in order to maximize the contrast between on and off states. For example, a switching structure that changes the transmission response from having EBG characteristics to complementary-SRR (CSRR) characteristics can possibly be achieved by modifying

the construction of the ground patterns. Also, the inter-coupled split-ring resonator structure can be modified to allow more control on the series inductance and capacitance on the microstrip line. Therefore, as the understanding of these periodic structures advances, they will become an integral part of the microwave and millimeter-wave components because of their simple designs and promising performances.

8. APPENDICES

8.1. APPENDIX A – EFFECTIVE PERMITTIVITY[‡]

Since the microstrip transmission line is based on a mixed-dielectric system, the effective microstrip permittivity (ε_{eff}) has to be determined. The ε_{eff} is a vital parameter in determining the velocity of the propagating waves with the microstrip transmission line as the medium. Therefore, the relationship between λ_g and ε_{eff} is as follow:

$$\begin{aligned} v_p &= f\lambda_g \\ c &= f\lambda_0 \end{aligned} \tag{8-1}$$

$$\lambda_g = \frac{\lambda_0}{\sqrt{\varepsilon_{eff}}} \tag{8-2}$$

v_p = Velocity of propagating wave in **microstrip**

c = Velocity of propagating wave in **free-space**

λ_g = Propagating wavelength in **microstrip**

λ_0 = Propagating wavelength in **free-space**

f = Propagating frequency

It has been found that the ε_{eff} is highly correlated to width-to-height ratio of the microstrip transmission line structure. For very wide microstrip lines, the ε_{eff} is approaching ε_r (the permittivity of the substrate) since most of the electric fields are confined within the substrate. For very narrow microstrip lines, the ε_{eff} is approaching

‡ The discussion in this appendix is based on Chapter 3 and 4 of the reference [8-1].

half of the combination of the substrate and the free-space. Fig. A-1 illustrates the two extreme cases of ε_{eff}.

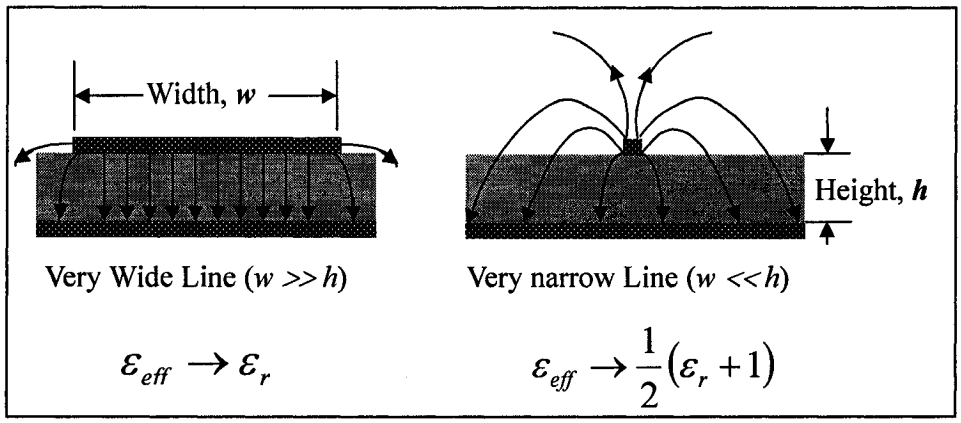

Fig. A-1: Microstrip transmission line structure with very wide and very narrow line widths.

Many closed-form formulas have been investigated and established to calculate ε_{eff} [8-2, 8-3]. Owens developed the closed-form formulas shown below, which is applicable to alumina-type substrates where the permittivity is between 8 and 12 ($8 \leq \varepsilon_r \leq 12$).

Case #1: $Z_0 > (44 - 2\varepsilon_r)\ \Omega$

$$\varepsilon_{eff} = \frac{\varepsilon_r + 1}{2}\left\{1 + \frac{29.98}{Z_0}\left(\frac{2}{\varepsilon_r + 1}\right)^{1/2}\left(\frac{\varepsilon_r - 1}{\varepsilon_r + 1}\right)\left(\ln\frac{\pi}{2} + \frac{1}{\varepsilon_r}\ln\frac{4}{\pi}\right)\right\}^2 \qquad (8\text{-}3)$$

Case #2: $Z_0 < (44 - 2\varepsilon_r)\ \Omega$

$$\varepsilon_{eff} = \frac{\varepsilon_r}{0.96 + \varepsilon_r(0.109 - 0.004\varepsilon_r)\{\log(10 + Z_0) - 1\}} \qquad (8\text{-}4)$$

However, the ε_{eff} calculated thus far is not frequency-dependent and is applicable for frequencies up to a few Giga-Hertz. As the operating frequency increases, the dispersion effect cannot be neglected anymore. The microstrip transmission line

structure exhibits the dispersion effect, which is a problem that the phase constant is not exactly doubled as the frequency of the transmitting signal doubles. Therefore, the phase velocity (v_p) becomes frequency-dependent and so as ε_{eff}.

$$\lambda_g = \frac{c}{f\sqrt{\varepsilon_{eff}(f)}} \tag{8-5}$$

$$\varepsilon_{eff}(f) \to \begin{cases} \varepsilon_{eff} & \text{as } f \to 0 \\ \varepsilon_r & \text{as } f \to \infty \end{cases} \tag{8-6}$$

Kirschning and Jansen [8-4] developed a set of formula, which can solve for ε_{eff} for all frequencies up to 60 *GHz* with accuracy better than 0.6 percent. The restrictions are as follow:

$$1 \le \varepsilon_r \le 20$$
$$0.1 \le w/h \le 100$$
$$0 \le h/\lambda_0 \le 0.13$$

The expression for calculating $\varepsilon_{eff}(f)$ is as follow where frequency f is in *GHz* and thickness h is in *cm*:

$$\varepsilon_{eff}(f) = \varepsilon_r - \frac{\varepsilon_r - \varepsilon_{eff}}{1 + P(f)} \tag{8-7}$$

$$P(f) = P_1 P_2 \{(0.1844 + P_3 P_4) \cdot 10fh\}^{1.5763} \tag{8-8}$$

$$P_1 = 0.27488 + \{0.6315 + 0.525/(1 + 0.157fh)^{20}\}(w/h) - 0.065683\exp(-8.7513w/h)$$
$$P_2 = 0.33622\{1 - \exp(-0.03442\varepsilon_r)\}$$
$$P_3 = 0.0363\exp(-4.6w/h)\left[1 - \exp\left\{-(fh/3.87)^{4.97}\right\}\right]$$
$$P_4 = 1 + 2.751\left[1 - \exp\left\{-(\varepsilon_r/15.916)^8\right\}\right]$$

Once the $\varepsilon_{eff}(f)$ is found, the guided wavelength traveling with the microstrip structure can be calculated. Therefore, the relationship between the period of the

electromagnetic bandgap structure (a) and the center stopband frequency can be established through the following equation.

$$a = \frac{\lambda_g}{2} = \frac{c}{2f\sqrt{\varepsilon_{eff}(f)}} \tag{8-9}$$

Thus, the dimension of the electromagnetic bandgap structure with desirable stopband frequency can be found.

8.2. APPENDIX B – SCATTERING PARAMETERS OF TWO-PORT NETWORK[§]

In a two-port transmission line network, the "scattering parameters" (S-parameters) are used to characterize the behavior of the incident and reflected waves. Fig. B-1 shows the two-port network with A_1 and B_1 as the incident and reflected waves at Port-1 and A_2 and B_2 as the incident and reflected waves at Port-2 respectively.

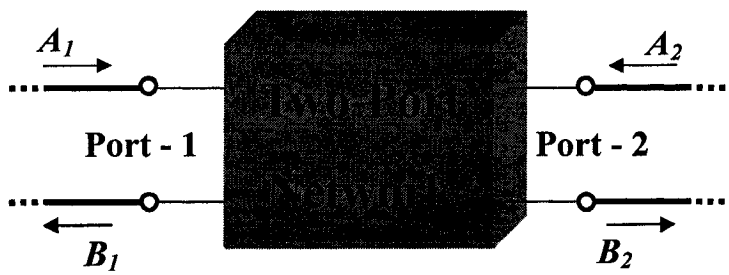

Fig. B-1: Two-port network showing incident and reflected waves at Port-1 and Port-2.

Thus, the relationships between the traveling waves at both ports can be expressed in

[§] The discussion in this appendix is based on Chapter 1 of the reference [8-5].

the following equations.

$$B_1 = S_{11}A_1 + S_{12}A_2$$
$$B_2 = S_{21}A_1 + S_{22}A_2 \tag{8-10}$$

or in matrix form,

$$\begin{bmatrix} B_1 \\ B_2 \end{bmatrix} = \begin{bmatrix} S_{11} & S_{12} \\ S_{21} & S_{22} \end{bmatrix} \begin{bmatrix} A_1 \\ A_2 \end{bmatrix} \tag{8-11}$$

S-parameters are defined as follows:

$S_{11} = \left.\frac{B_1}{A_1}\right|_{A_2=0}$ ***Input reflection coefficient*** (output properly terminated)

$S_{21} = \left.\frac{B_2}{A_1}\right|_{A_2=0}$ ***Forward transmission coefficient*** (output properly terminated)

$S_{22} = \left.\frac{B_2}{A_2}\right|_{A_1=0}$ ***Output reflection coefficient*** (input properly terminated)

$S_{12} = \left.\frac{B_1}{A_2}\right|_{A_1=0}$ ***Reverse transmission coefficient*** (input properly terminated)

Input/Output is properly terminated means that the characteristic impedance of the microstrip transmission line matches the termination so a traveling wave incident on the load will be absorbed totally and no energy will be returned to the output port. For example, when measuring the transmission coefficient (S_{21}), the output termination has to be matched with the characteristic impedance so A_2 is zero. Thus, the contribution to the transmitted wave at Port-2 (B_2) is only due to the incident wave at Port-1 (A_1) and the transmission coefficient of the network can be found. Therefore, the S-parameters are very useful in measuring the performance of the electromagnetic

bandgap and inter-coupled split-ring resonator structures that are based on microstrip transmission lines.

8.3. APPENDIX C – FABRICATION AND MEASUREMENT PROCEDURES

8.3.1. FABRICATION PROCEDURE

The following steps are the procedure used to fabricate the electromagnetic bandgap and inter-coupled split-ring resonator structures. The substrates are either Alumina (Al_2O_3) or Corning 1059 (SiO_2) with gold metallization on both sides.

1. Apply photo-resist (Shipley 1827) on one side of the sample with a spin rate of 3000 *rpm* for 30 seconds.
2. Pre-bake the sample for 10 minutes at 90°C.
3. Repeat step 1 and 2 for the second side of the sample.
4. Expose UV-light to the area where the gold metallization is to be etched away. Each side is exposed for 300 seconds.
5. Develop the photo-resist on the sample, rinse and spin dry.
6. Post-bake the sample for 10 minutes at 120°C.
7. Etch the gold metallization, rinse and spin dry.
8. Wash away the remaining photo-resist with acetone, rinse and spin dry.

For the optical switching applications, the CdS layer is deposited onto the sample

according to the method described in Chapter 5. To etch away the unwanted CdS in certain regions, the following steps were performed.

Electromagnetic bandgap structures:

1. Apply photo-resist (Shipley 1827) on the ground plane where the perforations are defined to protect the CdS layer.
2. Pre-bake the sample for 10 minutes at 90°C.
3. Immerse the sample into diluted hydrochloric acid (10% HCl) solution to etch away the CdS layer on the front side (where the microstrip line is).
4. Rinse and spin dry the sample.
5. Wash away the photo-resist with acetone, rinse and spin dry.

Split-ring resonator structures:

1. Apply photo-resist, 3000 *rpm* for 30 seconds, (Shipley 1827) on the front side of the sample where the split-ring patterns are defined to protect the CdS layer.
2. Pre-bake the sample for 10 minutes at 90°C.
3. Expose UV-light to the front side of the sample with the split-ring patterns covered for 300 seconds.
4. Develop the photo-resist on the sample, rinse and spin dry.
5. Immerse the sample into diluted hydrochloric acid (10% HCl) solution to etch away unwanted CdS.

6. Rinse and spin dry the sample.

7. Wash away the photo-resist with acetone, rinse and spin dry.

8.3.2. MEASUREMENT PROCEDURE

The Anritsu 37347A Vector Network Analyzer (VNA) is used to carry out the S-parameters measurements of the experimentally fabricated electromagnetic bandgap and inter-coupled split-ring resonator samples. A Universal Test Fixture (UTF, Inter-Continental Microwave) fixes the sample in place and the setup is connected to the VNA via microwave cables. Thus, the structure is being measured as a two-port network where S_{21} and S_{11} are used to characterize its performance. Fig. C-1 shows the schematic diagram of the measurement setup.

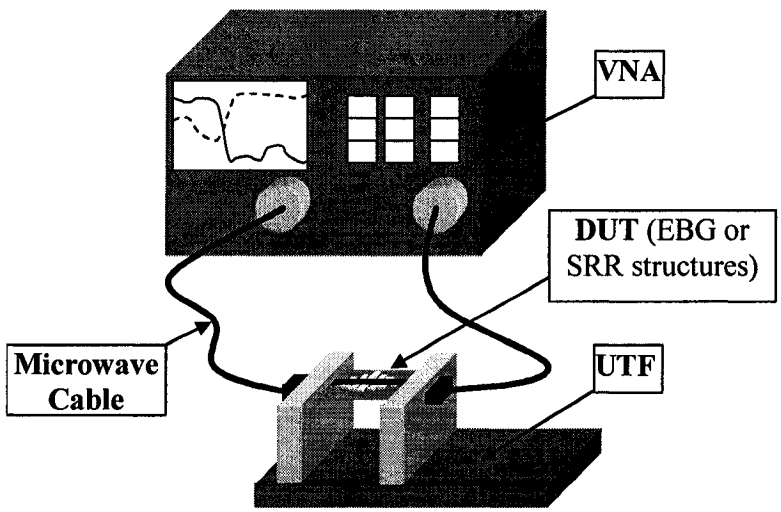

Fig. C-1: Schematics of the measurement setup with the vector network analyzer and the universal test fixture.

Prior to the measurements, the VNA is calibrated using TRL (Thru-Reflect-Line) method such that the reference planes for characterizing the samples are located 5 *mm*

from both edges. The samples were made to have extra spaces at both ends so the device under test (DUT) is only the EBG or the SRR structure. Therefore, losses due to the connectors, the cables, and the UTF are not included in the measurement results. Fig. C-2 shows a schematic diagram of an EBG sample with the locations of reference planes as an example.

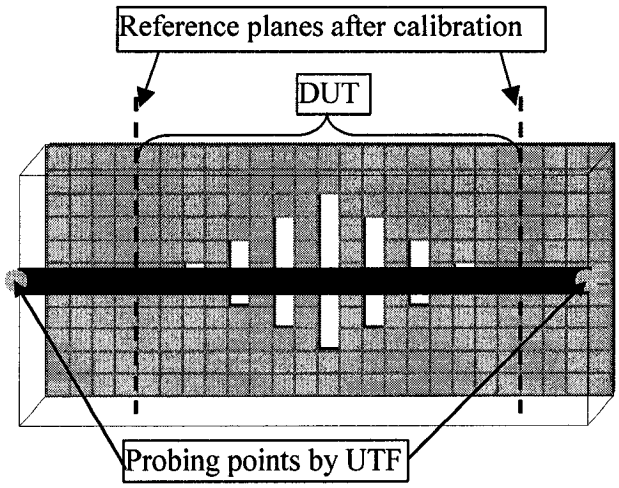

Fig. C-2: Schematic diagram of an electromagnetic bandgap structure with the position of reference planes.

8.3.3. TRL CALIBRATION

To measure structures like microstrip transmission line, Universal Test Fixture (UTF) is required to provide the connection between the Device Under Test (DUT) and the Vector Network Analyzer (VNA). However, calibration steps are required prior to the measurements to ensure the accuracy of the results. A set of in-fixture calibration standard is needed to remove the effects of VNA, cables, and UTF. Therefore TRL (Thru-Reflect-Line) calibration method provides a simple and

effective way to remove the measurement errors. To perform the TRL calibration, three standards are required: Thru, Reflect, and Line.

Thru

- Non-zero length line.
- Attenuation of the Thru is not required to be known.
- Reference plane is established at the center of the line.
- Z_0 must be the same as the Line.

Reflect

- Short or open that has phase within +/- 90°.
- Does not need to be perfect short or open (ideally the reflection coefficient, Γ, equals to 1) but need to specify either greater or less than Z_0.
- Γ must be identical at both Port -1 and Port-2.

Line

- Optimal length is $\lambda/4$ or 90° of insertion phase relative to the Thru.
- Attenuation of the Line is not required to be known.
- The difference between the Line and the Thru has to be between (20° and 160°) $\pm$ n $\times$ 180°.

All calibration standards should have the same characteristic impedance and

same width-to-height ratio as the DUT. Also, the accuracy of the calibration depends on the quality of the calibration standards. The bandwidth to which the TRL calibration is accurate is around 8:1 (frequency span:start frequency). This means the accuracy range is depending on the length of the Line and the Thru standards; thus more than one Line/Thru pairs are required if accurate result is needed for a wide frequency range. Therefore, the TRL calibration is ideal for measuring and characterizing the microstrip structures. More information on calibrations can be found in reference [8-6, 8-7, 8-8].

9. REFERENCES

[1-1] "Telecom Industry Revenue to Reach $1.2 Trillion in 2006," VoIP Magazine, 2005. (http://www.voip-magazine.com/content/view/1197/)

[1-2] E. Yablonovitch, "Inhibited spontaneous emission in solid-state physics and electronics," *Physical Review Letters*, Vol. 58, No. 20, May 1987, pp. 2059-2062.

[1-3] K. M. Ho, C. T. Chan, and C. M. Soukoulis, "Existence of a photonic gap in periodic dielectric structures," *Physical Review Letters*, Vol. 65, No. 25, Dec. 1990, pp. 3152-3155.

[1-4] E. Yablonovitch and T. J. Gmitter, "Photonic band structures: the face-centered-cubic case," *Physical Review Letters*, Vol. 63, No. 18, Oct. 1989, pp. 1950-1953.

[1-5] S. John, "Strong localization of photons in certain disordered dielectric superlattices," *Physical Review Letters*, Vol. 58, No. 23, June 1987, pp. 2486-2489.

[1-6] V. Radisic, Y. Qian, R. Coccioli, and T. Itoh, "Novel 2-D photonic bandgap structure for microstrip lines," *IEEE Microwave and Guided Wave Letters*, Vol. 8, No. 2, Feb. 1998, pp. 69-71.

[1-7] T. Lopetegi, M. A. G. Laso, M. J. Erro, M. Sorolla, and M. Thumm, "Analysis and design of periodic structures for microstrip lines by using the coupled mode theory," *IEEE Microwave and Wireless Comp. Letters*, Vol. 12, No. 11, Nov. 2002, pp. 441-443.

[1-8] M. A. G. Laso, T. Lopetegi, M. J. Erro, D. Benito, M. J. Garde, and M. Sorolla, "Multiple-frequency-tuned photonic bandgap microstrip structures," *IEEE Microwave and Guided Wave Letters*, Vol. 10, No. 6, June 2000, pp. 220-222.

[1-9] J. Wu, I. Shih, S. N. Qiu, C. X. Qiu, P. Maltais, and D. Gratton, "Photonic bandgap microstrips with controlled bandstops," *2nd CanSmart Workshop: Smart Materials and Structures*, Oct. 2002, pp. 171-179.

[1-10] J. Wu, I. Shih, S. N. Qiu, and C. X. Qiu, "Characterization of microwave photonic band-gap structures with bandpass filter applications," *Journal of Vacuum Sci. and Tech. A*, Vol. 24, No. 3, May/Jun 2006, pp. 827-830.

[1-11] M. Bozzetti, A. D'Orazio, M. De Sario, V. Petruzzelli, F. Prudenzano, and F. Renna, "Tapered photonic bandgap microstrip lowpass filters: design and realization," *IEE Proc.-Microwave Antennas Propagation*, Vol. 150, No. 6, Dec. 2003, pp. 459-462.

[1-12] T. Y. Yun and K. Chang, "Uniplanar one-dimensional photonic-bandgap structures and resonators," *IEEE Trans. on Microwave Theory and Tech.*, Vol. 49, No. 3, March 2001, pp. 549-553.

[1-13] J. Wu, S. N. Qiu, C. X. Qiu, and I. Shih, "Wide stopband EBG structure design based on 2D nonlinearly tapered slot array," *Microwave and Optical Tech. Letters*, Vol. 49, No. 1, Jan. 2007, pp. 31-34.

[1-14] K. O. Hill, Y. Fujii, D. C. Johnson, and B. S. Kawasaki, "Photosensitivity in optical fiber waveguides: Application to reflection filter fabrication," *Applied Physics Letters*, Vol. 32, Iss. 10, May 1978, pp. 647-649.

[1-15] T. Erdogan, "Fiber grating spectra," *Journal of Lightwave Technology*, Vol. 15, No. 8, Aug. 1997, pp. 1277-1294.

[1-16] J. B. Pendry, A. J. Holden, D. J. Robbins, and W. J. Stewart, "Magnetism from conductors and enhanced nonlinear phenomena," *IEEE Trans. on Microwave Theory and Tech.*, Vol. 47, No. 11, Nov. 1999, pp. 2075-2084.

[1-17] D. R. Smith, W. J. Padilla, D. C. Vier, S. C. Nemat-Nasser, and S. Schultz, "Composite medium with simultaneously negative permeability and permittivity," *Physical Review Letters*, Vol. 84, No. 18, May 2000, pp. 4184-4187.

[1-18] R. A. Shelby, D. R. Smith, and S. Schultz, "Experimental verification of a negative index of refraction," *Science*, Vol. 292, April 2001, pp. 77-79.

[1-19] V. G. Veselago, "The electrodynamics of substances with simultaneously negative values of ε and μ," *Soviet Physics Uspekhi*, Vol. 10, No. 4, Jan-Feb

1968, pp. 509-514.

[1-20] J. Bonache, F. Martin, J. Garcia-Garcia, I. Gil, R. Marques, and M. Sorolla, "Ultra wide band pass filters (UWBPF) based on complementary split rings resonators," *Microwave and Optical Tech. Letters*, Vol. 46, No. 3, Aug. 2005, pp. 283-286.

[1-21] J. Garcia-Garcia, F. Martin, F. Falcone, J. Bonache, I. Gil, T. Lopetegi, M. A. G. Laso, M. Sorolla, and R. Marques, "Spurious passband suppression in microstrip coupled line band pass filters by means of split ring resonators," *IEEE Microwave and Wireless Comp. Letters*, Vol. 14, No. 9, Sept. 2004, pp. 416-418.

[1-22] S. N. Burokur, M. Latrach, and S. Toutain, "Study of the effect of dielectric split-ring resonators on microstrip-line transmission," *Microwave and Optical Tech. Letters*, Vol. 44, No. 5, March 2005, pp. 445-448.

[1-23] J. Garcia-Garcia, J. Bonache, I. Gil, F. Martin, R. Marques, F. Falcone, T. Lopetegi, M. A. G. Laso, and M. Sorolla, "Comparison of electromagnetic band gap and split-ring resonator microstrip lines as stop band structures," *Microwave and Optical Tech. Letters*, Vol. 44, No. 4, Feb. 2005, pp. 376-379.

[1-24] H. W. Wu, Y. K. Su, M. H. Weng, and C. Y. Hung, "A compact narrow-band microstrip bandpass filter with a complementary split-ring resonator," *Microwave and Optical Tech. Letters*, Vol. 48, No. 10, Oct. 2006, pp. 2103-2106.

[1-25] J. Bonache, I. Gil, J. Garcia-Garcia, and F. Martin, "Novel microstrip bandpass filters based on complementary split-ring resonators," *IEEE Trans. on Microwave Theory and Tech.*, Vol. 54, No. 1, Jan. 2006, pp. 265-271.

[1-26] S. H. Jang and J. C. Lee, "Design of novel cross-coupling elliptic function filters with the miniaturized edge-coupled split ring resonators," *Microwave and Optical Tech. Letters*, Vol. 45, No. 6, June 2005, pp. 495-499.

[1-27] P. K. Nair, M. T. S. Nair, J. Campos, and L. E. Sansores, "A critical discussion of the very high photoconductivity in chemically deposited Cadmium Sulfide thin films: implications for solar cell technology," *Solar Cells*, Vol. 22, Issue 3,

Nov. 1987, pp. 211-227.

[1-28] P. K. Nair, J. Campos, and M. T. S. Nair, "Opto-electronic characteristics of chemically deposited cadmium sulphide thin films," *Semiconductor Sci. and Tech.*, Vol. 3, No. 2, Feb. 1988, pp. 134-145.

[1-29] M. Y. Frankel, R. H. Voelker, and J. N. Hilfiker, "Coplanar transmission lines on thin substrates for high-speed low-loss propagation," *IEEE Trans. on Microwave Theory and Techniques*, Vol. 42, No. 3, March 1994, pp. 396-402.

[1-30] W. Platte and W. Barrasch, "High-reflection 30 GHz grating structure optically induced in a CdS film coplanar waveguide on a ceramic substrate," *Electronics Letters*, Vol. 31, No. 5, March 1995, pp. 400-401.

[2-1] A. S. Andrenko, "Study and microwave applications of artificial periodic substrate PBG planar circuits," *Mathematical Methods in Electromagnetic Theory (MMET 2002)*, Vol. 1, pp. 21-26, Sept. 2002.

[2-2] Y. Qian; V. Radisic, and T. Itoh, "Simulation and experiment of photonic band-gap structures for microstrip circuits," *Asia-Pacific Microwave Conf. Proc. (APMC 1997)*, Dec. 1997, Vol. 2, pp. 585-588.

[2-3] V. Radisic, Y. Qian, and T. Itoh, "Broad-band power amplifier using dielectric photonic bandgap structure," *IEEE Microwave and Guided Wave Letters*, Vol. 8, No. 1, Jan. 1998, pp. 13-14.

[2-4] I. Rumsey, M. Piket-May, P. K. Kelly, "Photonic bandgap structures used as filters in microstrip circuits," *IEEE Microwave and Guided Wave Letters*, Vol. 8, No. 10, Oct. 1998, pp.336-338.

[2-5] F. R. Yang, R. Coccioli, Y. Qian, and T. Itoh, "Planar PBG structures: Basic properties and applications," *IEICE Trans. on Electronics*, Vol. E83-C, No. 5, May 2000, pp. 687-696.

[2-6] T. Kim and C. Seo, "A novel photonic bandgap structure for low-pass filter of wide stopband," *IEEE Microwave and Guided Wave Letters*, Vol. 10, No. 1, Jan. 2000, pp. 13-15.

[2-7] J. Yoon and C. Seo, "Improvement of broadband feedforward amplifier using photonic bandgap," *IEEE Microwave and Wireless Comp. Letters*, Vol. 11, No. 11, Nov. 2001, pp. 450-452.

[2-8] F. R. Yang, Y. Qian, R. Coccioli, and T. Itoh, "A novel low-loss slow-wave microstrip structure," *IEEE Microwave and Guided Wave Letters*, Vol. 8, No. 11, Nov. 1998, pp. 372-374.

[2-9] F. R. Yang, K. P. Ma, Y. Qian, and T. Itoh, "A uniplanar compact photonic-bandgap (UC-PBG) structure and its applications for microwave circuit," *IEEE Trans. on Microwave Theory and Techniques*, Vol. 47, No. 8, Aug. 1999, pp. 1509-1514.

[2-10] C. Y. Hang, V. Radisic, Y. Qian, and T. Itoh, "High efficiency power amplifier with novel PBG ground plane for harmonic tuning," *1999 IEEE MTT-S Microwave Symposium Digest*, Vol. 2, Jun. 1999, pp. 807-810.

[2-11] F. R. Yang, Y. Qian, and T. Itoh, "A novel uniplanar compact PBG structure for filter and mixer applications," *1999 IEEE MTT-S Microwave Symposium Digest*, Vol. 3, Jun. 1999, pp. 919-922.

[2-12] M. A. G. Laso, T. Lopetegi, M. J. Erro, D. Benito, M. J. Garde, and M. Sorolla, "Multiple-frequency-tuned photonic bandgap microstrip structures," *IEEE Microwave and Guided Wave Letters*, Vol. 10, No. 6, Jun. 2000, pp. 220-222.

[2-13] N. C. Karmakar and M. N. Mollah, "Investigations into nonuniform photonic-bandgap microstripline low-pass filters," *IEEE Trans. on Microwave Theory and Techniques*, Vol. 51, No. 2, Feb. 2003, pp. 564-572.

[2-14] J. B. Pendry, A. J. Holden, and W. J. Stewart, "Extremely low frequency plasmons in metallic mesostructures," *Physical Review Letters*, Vol. 76, No. 25, Jun. 1996, pp. 4773-4776.

[2-15] J. D. Baena, J. Bonache, F. Martin *et al*, "Equivalent-circuit models for split-ring resonators and complementary split-ring resonators coupled to planar transmission line," *IEEE Trans. on Microwave Theory and Techniques*, Vol. 53, No. 4, Apr. 2005, pp. 1451-1461.

[2-16] J. Garcia-Garcia, F. Martin, F. Falcone *et al*, "Microwave filters with improved stopband based on sub-wavelength resonators," *IEEE Trans. on Microwave Theory and Techniques*, Vol. 53, No. 6, Jun. 2005, pp. 1997-2006.

[2-17] F. Falcone, T. Lopetegi, J. D. Baena, R. Marques, F. Martin, and M. Sorolla, "Effective negative-ε stopband microstrip lines based on complementary split ring resonators," *IEEE Microwave and Wireless Comp. Letters*, Vol. 14, No. 6, Jun. 2004, pp. 280-282.

[2-18] S. N. Burokur, M. Latrach, and S. Toutain, "Phenomenon study of a microstrip line on a slot split ring resonators defected ground plane," *IEEE Antennas and Propagation Society International Symposium*, Vol. 1A, 3-8 July 2005, pp. 766-769.

[2-19] J. Wu, S. N. Qiu, C. X. Qiu, and I. Shih, "A novel method for switching and tuning of PBG structures," *Microwave and Optical Tech. Letters*, Vol. 43, No. 4, Nov. 2004, pp. 334-337.

[2-20] D. Cadman, D. Hayes, R. Miles, and R. Kelsall, "Simulation results for a novel optically controlled photonic bandgap structure for microstrip lines," *High Frequency Postgraduate Student Colloquium*, Sept. 2000, pp. 110-115.

[4-1] M. Le Roy and A. Perennec, "Novel circuit models of arbitrary-shape line: application to parallel coupled microstrip filters with suppression of multi-harmonic responses," *2005 European Microwave Conference*, Vol. 2, 4-6 Oct. 2005.

[4-2] A. G. Lamperez and M. S. Palma, "High selectivity X-band planar diplexer with symmetrical box-section filters," *2005 European Microwave Conference*, Vol. 1, 4-6 Oct. 2005.

[4-3] R. Phromloungsri, S. Patisang, K. Srisathit, and M. Chongcheawchamnan, "A harmonic-suppression microwave bandpass filter based on an inductively compensated micro strip coupler," *2005 Asia-Pacific Microwave Conf. Proc.*, 4-7 Dec. 2005.

[4-4] J. T. Kuo and M. Jiang, "Enhanced microstrip filter design with a uniform dielectric overlay for suppressing the second harmonic response," *IEEE*

Microwave and Wireless Comp. Letters, Vol. 14, No. 9, Sept. 2004, pp. 419-421.

[4-5] R. J. Wenzel, "Exact design of TEM microwave networks using quarter-wave lines," *IEEE Trans. on Microwave Theory and Techniques*, Vol. 12, No. 1, Jan. 1964, pp. 94-111.

[4-6] C. L. Hsu, F. C. Hsu, and J. K. Kuo, "Microstrip bandpass filters for ultra-wideband (UWB) wireless communications," *2005 IEEE MTT-S International*, 12-17 June 2005.

[4-7] J. S. Hong and H. Shaman, "An optimum ultra-wideband microstrip filter," *Microwave and Optical Tech. Letters*, Vol. 47, No. 3, Nov. 2005, pp. 230-233.

[4-8] J. S. Hong and M. J. Lancaster, "*Filters for RF/Microwave applications*," USA, John Wiley & Sons, 2001, Ch. 3.

[5-1] T. L. Chu, S. S. Chu, C. Ferekides, C. Q. Wu, J. Britt, and C. Wang, "High efficiency CdS/CdTe solar cells from solution-grown CdS films," *22nd IEEE Photovoltaic Specialists Conf.*, Vol. 2, 7-11 Oct. 1991, pp. 952-956.

[5-2] X. Wu, R. G. Dhere, Y. Yan, I. J. Romero, Y. Zhang, J. Zhou, C. DeHart, A. Duda, C. Perkins, and B. To, "High-efficiency polycrystalline CdTe thin-film solar cells with an oxygenated amorphous CdS (a-CdS:O) window layer," *29th IEEE Photovoltaic Specialists Conf.*, 19-24 May 2002, pp. 531-534.

[5-3] A. Amith, "Thickness dependence of structural and electrical properties of CdS films for Solar cells," *Journal of Vacuum Sci. and Tech.*, Vol. 15, No. 2, Mar/Apr 1978, pp. 353-358.

[5-4] A. Morales-Acevedo, O. Vigil-Galan, G. Contreras-Purnte *et al*, "Physical properties of CdS thin films grown by different techniques: a comparative study," *29th IEEE Photovoltaic Specialists Conf.*, 19-24 May 2002, pp. 624-627.

[5-5] H. Ashour, F. El Akkad, R. Bohari, and K. H. Herrmann, "Properties of R. F. sputtered CdS thin films," *11th International Conf. on Microelectronics*, Nov. 22-24, 1999, pp. 263-265.

[5-6] S. S. Hegedus, "The photoresponse of CdS/CuInSe2 thin-film heterojunction solar cells," *IEEE Trans. on Electron Devices*, Vol. 31, No. 5, May 1984, pp. 629-633.

[5-7] N. K. Annamalai, C. C. Chao, and D. Raymond, "Technique to determine the growth rate and resistivity of evaporated CdS thin films," *Journal of Vacuum Sci. and Tech.*, Vol. 16, No. 2, Mar/Apr 1979, pp. 222-225.

[5-8] E. A. Gluszak and S. Hinckley, "Optical and electrical properties of chemically deposited CdS thin films modified by air annealing," *Conf. on Optoelectronic and Microelectronic Materials Devices*, 14-16 Dec. 1998, pp. 426-429.

[5-9] M. D. Archbold, D. P. Halliday, K. Durose, T. P. A. Hase, D. Smyth-Boyle, and K. Govender, "Characterization of thin film Cadmium Sulfide grown using a modified chemical bath deposition process," *IEEE 31st Photovoltaic Specialists Conf.*, 3-7 Jan. 2005, pp. 476-479.

[5-10] S. Abd-Lefdil, C. Messaoudi, M. Abd-Lefdil, and D. Sayah, "Temperature growth and annealing effects on CdS thin films prepared by chemical bath deposition process," *Physica Status Solidi A*, Vol. 168, 1998, pp. 417-423.

[5-11] R. Mendoza-Perez, G. Santana-Rodriguez, J. Sastre-Hernandez, A. Morales-Acevedo, A. Arias-Carbajal, O. Vigil-Galan, J. C. Alonso, and G. Contreras-Puente, "Effects of thiourea concentration on CdS thin films grown by chemical bath deposition for CdTe solar cells," *Thin Solid Films*, Vol. 480-481, 2005, pp. 173-176.

[5-12] N. R. Pavaskar, C. A. Menezes, and A. P. B. Sinha, "Photoconductive CdS films by a chemical bath deposition process," *Journal of The Electrochemical Society*, Vol. 124, No. 5, May 1977, pp. 743-748.

[5-13] P. J. Sebastian, A. Sanchez, and P. K. Nair, "Modification of the dark and photoconductivity and the optical transmittance of solution-grown CdS thin films," *Advanced Materials for Optics and Electronics*, Vol. 2, No. 3, May/Jun 1993, pp. 133-141.

[8-1] Terry Edwards, "*Foundations for microstrip circuit design*," England, John

Wiley & Sons, 2nd Edition, 1992, Ch. 3-4.

[8-2] H. A. Wheeler, "Transmission-line properties of parallel strips separated by a dielectric sheet," *IEEE Trans. on Microwave Theory and Tech.*, Vol. 13, No. 2, March 1965, pp. 172-185.

[8-3] R. P. Owens, "Accurate analytical determination of quasi-static microstrip line parameters," *The Radio and Electronic Engineer*, Vol. 46, No. 7, July 1976, pp. 360-364.

[8-4] M. Kirschning and R. H. Jansen, "Accurate model for effective dielectric constant of microstrip with validity up to millimeter-wave frequencies," *Electronics Letters*, Vol. 18, No. 6, March 1982, pp. 272-273.

[8-5] Guillermo Gonzalez, "*Microwave transistor amplifiers: analysis and design*," Prentice-Hall, 2nd Edition, 1997, Ch. 1.

[8-6] "In-fixture microstrip device measurements using TRL calibration," Product Note, PN 8720-2, 5091-1943E, Agilent Technologies, 2000.

[8-7] "Specifying calibration standards for the Agilent 8510 network analyzer," Product Note 8510-5B, 5956-4352, Agilent Technologies, Sept. 2001.

[8-8] "In-fixture measurements using vector network analyzers," Application Note, AN 1287-9, 5968-5329E, Agilent Technologies, 2000.